INERTIAL PARTICLES AND ENTRAINMENT IN TURBULENT FLOWS

A Dissertation

Presented to the Faculty of the Graduate School

of Cornell University

in Partial Fulfillment of the Requirements for the Degree of

Doctor of Philosophy

by

Garrett Hayes Good

August 2013

INERTIAL PARTICLES AND ENTRAINMENT IN TURBULENT FLOWS

Garrett Hayes Good, Ph.D.

Cornell University 2013

This work consists of three independent experimental studies. The first studies inhomogeneous turbulence with (even symmetric) non-Gaussian velocity probability density functions, created by partitioning an active grid in a wind tunnel. The turbulence is like that encountered in the environment (e.g., by wind turbines) or produced by fractal grids. The statistics of the turbulence are shown in particular to depend simply upon the spatial derivatives of the velocity r.m.s. field. The second study characterizes the intermittent nature of an inertial particle mixing layer, where a particle-laden flow entrains a particle-free flow. This is the case at the boundary of a cloud and affects its growth and hence climate modelling. The flow is accomplished with water droplets in a wind tunnel downstream of a splitter plate; the experiments are done for both homogeneous turbulence and where the active grid is partitioned to create an inhomogeneous interface like in the first study. We show the droplets to be entrained in intermittent, large-scale bursts, preserving the properties of the air and turbulence ambient to them, which in a cloud are critical to droplet growth. Gravitational settling effects are isolated by rotation of the apparatus. The third and final study takes a more fundamental look at inertial particles in isotropic conditions using both numerical simulations and water droplets in air turbulence from 32 loudspeaker jets aimed at a central point. Turbulent settling speeds, velocity variance and variance anisotropy are measured over an unprecedented parameter range, identifying all relevant parameterizations of particle inertia

and buoyancy affecting their response to turbulence, with applications to all particle-carrying flows. The three mechanisms by which turbulence modifies settling speeds (as compared to in quiescent flow) are isolated for the first time, with vertical turbulent motions shown to be responsible for settling reductions and horizontal ones to be for enhancements. The three experiments rely on hot-wire anemometry, phase Doppler particle analysis (PDPA) and high-speed camera Lagrangian particle tracking techniques. The body of the text consists of three stand-alone papers. The dissertation work provides fundamental understanding for wide-ranging environmental and industrial engineering problems.

BIOGRAPHICAL SKETCH

Garrett Good was born in Portland, Oregon in March 1987. His parents hail from the San Francisco Bay Area and divorced when he was young. Garrett's mother, Kim Erickson, supported him and his younger sister waiting tables until remarrying, after which she would be a stay-at-home mom, a paraeducator and school secretary. Garrett's heritage is mostly Northern European, but also German. His Portland experience was typical of national stereotypes.

Garrett graduated from Woodrow Wilson High School in 2005, where he developed a great love for Germany during a class exchange in the summer of his junior year. He thought his scientific interests best advanced at university, while personally maintaining those in the humanities. He graduated from Tufts University *summa cum laude* in 2009 in mechanical engineering, also majoring in mathematics and minoring in German. He began graduate work at Cornell University that year, completing his Masters in 2011. He then went abroad with a Fulbright award to conduct research at the Max Planck Institute for Dynamics and Self-Organization in Göttingen, Germany, where he finished his Cornell PhD in 2013.

Garrett enjoys music, games and sports. He loves the snow, and plays floorball or ice hockey whenever he can. He continues to live in Germany.

In memory of Tanya Mitra,

who dreamt to become a doctor.

ACKNOWLEDGEMENTS

I owe this work to Zellman Warhaft, my advisor and mentor at Cornell. For all of Zellman's invaluable contributions to my growth as a scientist, there were equally generous contributions to me personally. Zellman is a comforting example of the diverse interests and uncompromising purpose that can be maintained in life.

I am also grateful to Eberhard Bodenschatz for his invitation to Göttingen and his enthusiastic support for my work and career. Eberhard champions discovery and has afforded me not only the means, but along with Zellman, great patience and the freedom to pursue my goals. I thank the rest of my committee: Todd Cowen, for the use of the DeFrees Laboratory, his expertise and his unwavering positivity and concern for his students, and Lance Collins, for his vital collaboration and perspective as a computational scientist, his kind character, and humoring of an experimentalist's rival jests.

Many have helped me along the way at Cornell. I would not have completed my PhD without Marcia Sawyer's thoughtful guidance. I would have reached no heights without the ropes Sergiy Garashchenko taught me in the lab. I have benefited from the attention of the Collins' group during too many early morning meetings and from their collaboration, particular with Peter Ireland, without whose endless willingness to help and simulation results my final paper would not have been possible.

The MPI-DS family is massive. I have benefited from the knowledge and experience of Haitao Xu, Holger Nobach, Gregory Bewley, Heng-Dong Xi, and Ewe-Wei Saw. I have been assisted by the entire MPI-DS staff, and especially Angela Meister, Andreas Kopp, and Denny Fliegner, with every paperclip, nut and bolt, and network cable.

I have enjoyed the support of the National Science Foundation while at Cornell and of the Fulbright Program and Max Planck Society while in Göttingen. The staff of the German-American Fulbright Commission provide an amazing service.

I am grateful for the loyalty and love of friends and family, often a world away, who have held me upright throughout the tribulations of my graduate studies and stand with me to celebrate their conclusion.

TABLE OF CONTENTS

[1] Additional details of the experiments and data analysis are provided for the thesis in Appendix A

[2] Additional details of the experiments and data analysis are provided for the thesis in Appendix A

[3] Additional details of the experiments and data analysis are provided for the thesis in Appendix A

CHAPTER 1

INTRODUCTION

Turbulence is a topic not only of great fundamental interest but also of relevance to real, physical problems in the environment and engineering. It plays principle roles in surface water flows, the ocean, the weather and atmosphere and the stresses experienced by structures exposed to them, volcanic eruptions, nebulae and planet formation, spray injectors, gas turbine combustors, fluidized beds, and pollutant dispersion, to name more than a few. These diverse problems are all connected by the single and ubiquitous phenomenon of turbulence, complex even in its most simplified and model form. We are however interested in the complexity added by the features shared by these real flows, in their often inhomogeneous structure and in the behaviour of the fields of heavy particles they may carry.

While homogeneous turbulence has a given spectrum ranging from a common scale at which energy is supplied down to one where it is dissipated, these scales vary in space in an inhomogeneous, *multi-scale* flow. The non-linear interaction between such scales is not analytically understood and the interaction is important, for example, in understanding the structure of wall-bounded flows (Marusic et al., 2010), particularly those which interact with free-stream turbulence (Hancock and Bradshaw, 1989; Hunt and Graham, 1978; Sharp et al., 2009), like in the atmosphere. The velocity field probability density function (pdf) and its moments differ for these flows from the Gaussian nature of model turbulence. This has definite consequences for turbulent convection or diffusive processes which typically occur in such flows (Cebeci and Bradshaw, 1977; Hunt, 1985), or for the intermittently high stresses experienced by wind tur-

bines, which lead to their early failure (Windpower Monthly, 2005).

In Chapter 2, we use a combination of active and passive grids in a wind tunnel to generate a turbulent flow whose velocity statistics strongly contrast those of model turbulence. We investigate under what conditions the velocity pdf is skewed or may have symmetric but non-Gaussian tails, being either comparatively narrow or broad (even exponential). Exponential tails exist for fluid and particle accelerations (Ayyalasomayajula et al., 2006b) and for scalar fields (Gollub et al., 1991; Jayesh and Warhaft, 1991) in turbulence. Similar pdfs have also been observed in experimental work with fractal grids (Mazellier and Vassilicos, 2010; Krogstad and Davidson, 2011).

Inhomogeneous flows exist at the interfaces between flows of different properties, where one flow entrains another. This is precisely the case in a turbulent jet, which grows by entraining the quiescent fluid beside it, (or perhaps fluid with some free-stream turbulence). In the case of the jet there is also turbulence-generating shear at the interface, precisely as in the similarly-organized, Chapter 2 flows. Entrainment is in fact the mechanism by which all turbulent flows grow and has thus been the focus of much research regarding classic shear flows (for both the velocity and scalar fields) (Townsend, 1976), reactions (Broadwell and Breidenthal, 1982), turbulent plumes (Turner, 1986), the atmospheric boundary layer (Deardorff, 1974), stable density interfaces (Kantha et al., 1977) and clouds (Shaw, 2003; Andrejczuk et al., 2004).

In the relatively simple case of an interface between a turbulent and relatively quiescent flow (without shear), there is a turbulence mixing layer, where energetic eddies from one side both expel fluid and pull across and entrain fluid of differing properties from the other side. In Chapter 3, we study such a case,

where the turbulent fluid is laden with particles and the particle-laden flow grows by the entrainment of dry, (in this case) relatively quiescent air. This is precisely the case at the boundary of a turbulent cloud, albeit without shear. We create this flow in a wind tunnel using a combination of an active grid and screens and compare with the case where the turbulence properties are homogeneous (active grid only), but still only one half of the flow is initially particle-laden, such that the particle flow is again strongly inhomogeneous downstream of a splitter plate. Little is known about the entrainment of inertial particles, which are heavier than their carrier fluid, like water droplets in clouds or fuel droplets in combustors.

We paint the picture of an interface where the entrainment is characterized by large-scale intermittency due to the exchange of fluid by the large scales. We look at the intermittent nature of the particle entrainment process, as opposed to a smooth, diffusive one, and how the large-scale intermittency of inhomogeneous turbulence adds to this. In the example of the cloud, while a smooth diffusive process may capture the evolution of mean droplet number densities and the growth of the cloud boundary itself, the evolution of the droplet size and field are rather dependent upon properties local to droplets, which may be preserved if they are entrained in bulk. Particle inertia and settling no doubt play important roles in how inertial particles resist or preserve large-scale clustering due to entrainment. We present both single- and two-point statistics of the particle fields and assess the intermittent nature of the two mixing layers, also rotating the apparatus to isolate gravitational effects.

It is of course pertinent that even homogeneous particle fields move and distribute themselves in nontrivial ways in isotropic, model turbulence. Due to

their higher density, inertial particles are typically centrifuged away from highly vortical regions and concentrate in regions of strain in turbulence, resulting in a significant clustering of sub-Kolmogorov-sized particles at the Kolmogorov scale (Squires and Eaton, 1991; Wang and Maxey, 1993). The small-scale properties of the turbulence are of key importance. Particles cluster most when their inertial response times are similar to the timescales (lifetimes) of the Kolmogorov eddies, such that their motion couples best to these eddies. Particles with less inertia respond more like tracers in the flow, and those with more may couple to larger eddies, but have this coupling disrupted by the existence of smaller eddies in the flow.

The case is similar for how turbulence modifies particle settling velocities from those in quiescent fluid. Speeds are increased as particles have a preference for the downward-sweeping sides of eddies as they fall past them (Wang and Maxey, 1993; Dávila and Hunt, 2001; Aliseda et al., 2002; Hill, 2005; Nielsen, 1993). This increase scales with the turbulence r.m.s. velocity, and is highest for particles which again couple best to the smallest eddies in the flow. Less inertial particles have less preference and heavier particles (more negatively buoyant), either by their inertia or simply by falling too quickly to respond to the turbulence, can fail to couple to even the largest structures in the flow (Nielsen, 1993; Yang and Lei, 1998; Dávila and Hunt, 2001; Yang and Shy, 2005; Ghosh et al., 2005; Kawanisi and Shiozaki, 2008).

There are also two mechanisms by which turbulence may slow settling speeds. In what Nielsen (1993) described as loitering, the turbulent velocity field may appear frozen to particles which fall too quickly to be preferentially swept and side-step eddies. Such particles equally bisect upward- and downward-

moving regions of the flow, spending more time crossing the former, slowing them on average. The second is the nonlinear drag mechanism. With linear drag, the flow around the surface of a particle is locally Stokesian on the scale of the particle. If this flow reaches a sufficient Reynolds numbers to be non-Stokesian, particle drag coefficients increase, particularly as particles fall across upward-moving flow (Mei, 1994; Yang and Shy, 2003). Turbulent settling speeds are determined by the balance of all three mechanisms, (all of which vanish in the limit of infinite particle inertia), and in the axisymmetric system with gravity, particles may respond differently to the vertical and horizontal turbulent motions which determine this balance.

In Chapter 4, direct numerical simulations of a vast array of particle fields are used in conjunction with new experiments with water droplets in isotropic, soccer ball air turbulence, (generated by 32 loudspeaker jets), to study the motion of settling particles in model turbulence. The three mechanisms are isolated for the first time and the two-parameter space of particle weight and inertia are resolved over an unprecedented range of particles, revealing a large number of physically significant non-dimensional parameters to affect their mean settling speeds, velocity variance and variance anisotropy. The results are of fundamental interest to the many real examples of particle-carrying, turbulent flows.

We proceed with the first study in Chapter 2, followed by the second and third in Chapters 3 and 4. These are each written as independent papers, with standalone abstracts, introductions and conclusions. The comprehensive conclusions of this dissertation work and suggestions of future work are given in Chapter 5. Details of the experiments not summarized in the papers may be found in Appendix A of the thesis.

CHAPTER 2

ON THE PROBABILITY DISTRIBUTION FUNCTION OF THE VELOCITY FIELD AND ITS DERIVATIVE IN MULTI-SCALE TURBULENCE [1]

Using a combination of active and passive grids, we produce an inhomogeneous turbulent flow with strongly non-Gaussian velocity probability distribution (density) functions (pdfs). This new, multi-scale flow shares features with the turbulent jet in freestream turbulence, the near field of turbulence-generating grids, and atmospheric flows. In particular, we study unskewed velocity distributions with both super- and sub-Gaussian tails, and demonstrate the linear dependence of the normalized odd and even moments of the distributions on the first and second spatial derivatives of the turbulence r.m.s. fields, respectively. We also note bimodal behavior of the pdfs. The experiments demonstrate a clear effect of the flow organization and the large-scale intermittency on the velocity derivative pdfs and the small scales of the turbulence. The work is motivated by the complex wind fields, and associated, intermittent high stresses, encountered by wind turbines. We also draw comparisons to recent studies of multi-scale turbulence produced by fractal grids.

2.1 Introduction

Multi-scale turbulent flows, despite both their ubiquity in nature and industry, are still far from being well understood. The non-linear interaction between two or more dominant scales presents a complexity beyond present analytical understanding. For example, the recent review by Marusic et al. (2010) em-

[1] Reprinted with permission from Garrett H. Good and Zellman Warhaft, *Phys. Fluids*, Vol. 23, Pages 95-106, (2011).

phasizes problems relating the role of the large-scale motions in determining the overall boundary layers structure. The interaction of free stream turbulence with boundary layer turbulence is still not well understood (Hancock and Bradshaw, 1989; Hunt and Graham, 1978; Sharp et al., 2009). These types of flows are of importance in many applications; heat transfer and diffusive processes, for example, usually occur in complex turbulent flows (Cebeci and Bradshaw, 1977; Hunt, 1985). Here, our objective is to explore the nature of the probability distribution function (pdf) of the velocity field in a complex, inhomogeneous flow produced by means of a combination of active and passive grids.

Our interest is motivated by a better understanding of the wind field intercepted by wind turbines. It is commonly assumed that the turbulence has a Gaussian distribution. If, on the other hand, the pdf is non-Gaussian, with the probability of rare, high intensity events being much greater than that implied by a Gaussian distribution, then the wind turbine and its associated drive train may undergo frequent high stresses that may lead to failure [2]. While some field measurements (Naert et al., 1998) find non-Gaussian behavior in the atmospheric boundary layer (ABL) and the relationship between velocity skewness and kurtoses under convective conditions in the atmosphere has been documented (Alberghi et al., 2002; Lenchow et al., 1994), the nature of the velocity pdf does not appear to have been studied under controlled laboratory conditions, although there are some computational and theoretical studies on long tailed distributions in two dimensional turbulence (Bracco et al., 2000a; Jimenez, 1996). We note that the situation is different for scalar fields, where investigations in the 1990s showed that the scalar pdf may have stretched exponential

[2]Presently, the lifetime of a gear box is typically much less than their design life-goal of twenty years, and this is largely due to the intermittent stresses (Windpower Monthly, 2005)

tails in a velocity field that is Gaussian (Gollub et al., 1991; Jayesh and Warhaft, 1991). We ask under what conditions may we expect stretched tails in the velocity field?

In the present study, we engineer a wind field that departs significantly from that with a Gaussian distribution. We are particularly interested in the case of symmetric pdfs with broad tails, as have been observed for scalar fields, since skewed pdfs with a single long tail are trivial to obtain, and are not a good basis for comparison with Gaussian turbulence. We argue that the type of wind field studied here may be similar to that in the upper layers of the atmospheric boundary layer, where gusts of large scale turbulence penetrate into the boundary layer from above. Our flow is also of basic interest because of its novelty, and because of its relationship to recent work using grids with complex geometries (e.g., Mazellier and Vassilicos, 2010; Krogstad and Davidson, 2011).

2.2 Experimental Apparatus & Procedure[3]

The experiments were conducted in the DeFrees laboratory, 20 m open-circuit wind tunnel, which has a cross section of approximately 1×1 m (Ayyalasomayajula et al., 2006a). The flows were engineered to produce turbulence with long, symmetric tails in the velocity distributions. They were generated using an active grid, modified by the removal of the center rows of winglets (see figure 2.1) that randomly rotate to generate high Reynolds number turbulence (Mydlarski and Warhaft, 1996; Kang and Meneveau, 2008). We will sometimes

[3] Additional details of the experiments and data analysis are provided for the thesis in Appendix A

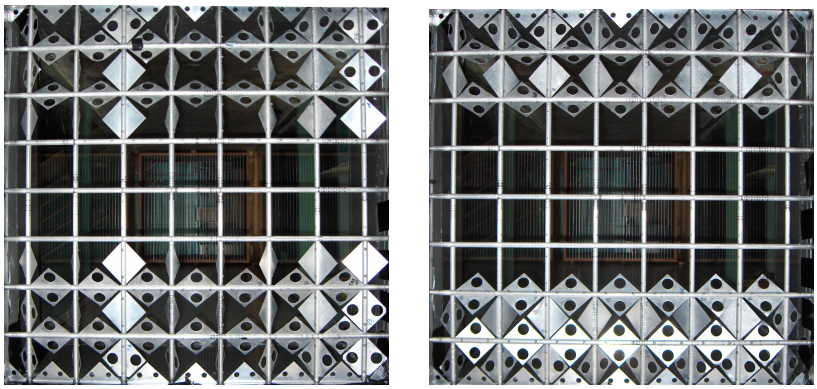

Figure 2.1: Photos of the active grid arrangements for flows 1 (left) and 2 (right). The grid has a mesh length of 10 cm. The perforated winglets were used to adjust the drag and shear produced by the active grid sections.

refer to this center section as the grid gap. In this way the flow is transversely symmetric and strongly inhomogeneous, with lower-level turbulence at its center, high-level turbulence generated on each side, and still stronger turbulence at the grid-grid gap interfaces due to shear. (There is shear because the active grid produces more drag than the passive grid bars). A schematic of the flow design is shown in figure 3.2. Two flows were studied, denoted as flows 1 & 2; flow 2 has a larger grid gap and higher flow speed than flow 1, and subsequently higher Reynolds numbers and more intense shear. The streamwise and transverse coordinates are x and y and have corresponding fluctuating velocity components u and v. The grid is at $x \equiv 0$, and the tunnel center is at $y \equiv 0$. The sketch includes qualitative profiles of the mean streamwise velocity, U, and the turbulence r.m.s., σ, whose components are defined as $\sigma_u \equiv \sqrt{u^2}$ and $\sigma_v \equiv \sqrt{v^2}$.

Measurements were by means of a TSI 1241 hot wire anemometer X-array with tungston wires (Mydlarski and Warhaft, 1996). The wires have a diameter of 3.2 μm and a length-to-diameter ratio of around 200. The measurement planes were placed at the streamwise locations of peak v kurtoses along $y = 0$ (at

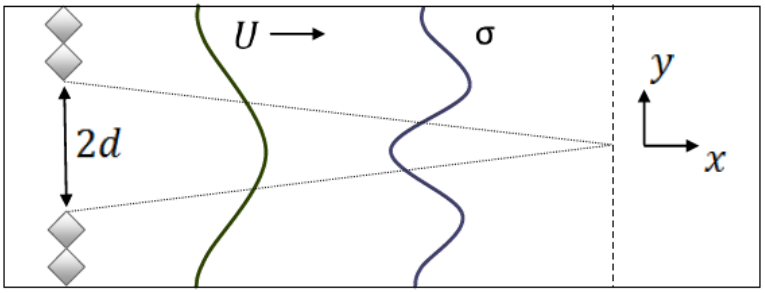

Figure 2.2: Sketch of the flow. The active grid (diamonds) gap dimension, d, is given in table 2.1, as is the measurement plane (dashed line) distance from the grid, X_K. The diagonal lines represent the growth of the two turbulent regions. U and σ are the mean and r.m.s. velocities. There is a thin boundary layer at each wall (not shown).

$x \equiv X_K$). These were 0.55 and 1.00 m downstream of the grid for flows 1 and 2, respectively. A streamwise peak in kurtoses was anticipated since immediately downstream of the grid the turbulent fluctuations would certainly fail to influence the flow center, and sufficiently downstream of the grid the inhomogeneity (and hence intermittency) would be mixed out. This evolution will be discussed in the results section. It should be noted, however, that while the measurement planes were not particularly far from the grid, they were sufficiently distant so that the near field inhomogeneities produced by the grid were insignificant[4].

[4]For a passive grid, the near field occurs within about 30 mesh lengths. Here, the energy of the grid-gap passive grid turbulence is insignificant compared to that generated by the active grid and shear.

2.3 Results and Analysis

2.3.1 Flow characterization

Figure 2.3a shows profiles of the mean streamwise velocity, U, in flows 1 and 2, while figure 2.3b shows the streamwise and transverse velocity r.m.s., σ_u and σ_v, at the measurement planes. Due to the strong transverse inhomogeneity, there is no single turbulence scale to collapse the measurements of flows 1 and 2. The transverse coordinate has been normalized instead by L, the distance from the flow centers to the peaks in turbulence r.m.s. (see figure 2.3b), which is similar to the grid gap half-widths. The geometric scale L is a natural choice for the flows and for the comparison of their velocity profiles. At the flow centers the mean velocity is close to uniform, with shear becoming significant beyond $|y/L| \gtrsim 0.5$ and $|y/L| \gtrsim 0.3$ for flows 1 and 2, respectively. The role of shear will be addressed later. The mean velocity for flow 2 is approximately double that of flow 1, as is the turbulence r.m.s. Outside their centers, both flows show anisotropy of $\sigma_u/\sigma_v \approx 1.3$, consistent with the active grid turbulence (Mydlarski and Warhaft, 1996). Anisotropy is nearly uniform through the measurement plane for flow 1, while for flow 2 the turbulence becomes nearly isotropic at the center ($\sigma_u/\sigma_v \approx 1.05$). The active grid turbulence, and its associated anisotropy, is less influential on the flow 2 center due to its larger grid gap and the increased role of shear-generated turbulence. The turbulence intensity, σ_u/U (figure 2.3c), is similar for both flows, ranging from 12.5 to 25% for flow 1 and 10 to 30% for flow 2 between the flow centers and the grid turbulence.

Profiles of the Taylor scale Reynolds number, $Re_\lambda \equiv \frac{\sigma_u \lambda}{\nu}$ are shown in figure 2.4a. (Here, $\lambda \equiv \sqrt{15\nu\sigma_u^2/\epsilon}$ is the Taylor microscale, where ν is the

kinematic viscosity and ϵ is the turbulence dissipation rate, estimated as $\epsilon \equiv 15(\nu/U^2)\langle(\partial u/\partial t)^2\rangle$ using Taylor's hypothesis). The Reynolds number peaks near the edge of the active grid (near $|y/L| = 1$), where the shear produces additional turbulence. Here, $Re_\lambda \approx 200$ and $Re_\lambda \approx 400$ for flows 1 and 2, respectively. Minimum Reynolds numbers ($Re_\lambda \approx 135$ and $Re_\lambda \approx 250$) occur at the flow centers. Figure 2.4b shows turbulence production, $\mathcal{P} \approx \langle uv\rangle\frac{\partial U}{\partial y}$, normalized by ϵ. The ratio indicates the importance of shear in the flows. Production is zero at the flow centers by symmetry, and remains weak for $|y/L| \lesssim 0.5$ in flow 1 and $|y/L| \lesssim 0.25$ for flow 2. The ratio $\mathcal{P}/\epsilon$ peaks near $|y/L| = 0.8$; the peak locations are inset from the grid-grid gap interfaces due to the lower turbulence levels and dissipation rates near the flow centers. Clearly, shear is more dominant in the energy balance for the high-speed flow 2, with the ratio $\mathcal{P}/\epsilon$ reaching about 1.25 at its peaks, where it is only approximately 0.5 for flow 1. The main flow characteristics are listed in table 2.1.

2.3.2 Flow evolution and turbulent shear structures

For the present study, we focus on the location of highest intermittency in "symmetric" turbulence, that is, where the velocity probability distributions are broadest while still symmetric. The measurement planes were set at the streamwise locations of peak v kurtoses, $K_4(v) \equiv \langle v^4\rangle/\sigma_v^4$, upstream of which the influence of the two turbulent regions on the flow centers is diminished by their seperation, and downstream of which the flow begins to mix out. This is captured in figure 2.5, which shows the evolution of both σ_v and $K_4(v)$ for one half of flow 1. Moving downstream from the grid, the shear layers grow and the highly turbulent regions ($|y/L| \gtrsim 1$) both decay and mix into the cen-

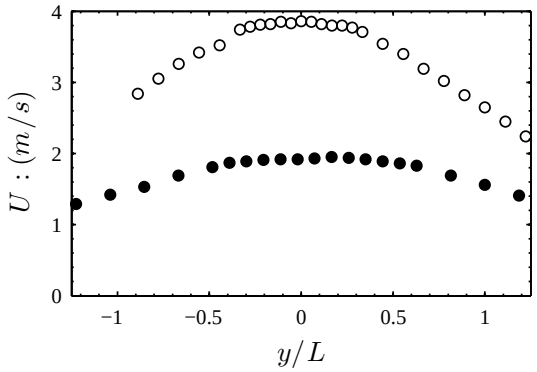

a) Mean streamwise velocity.

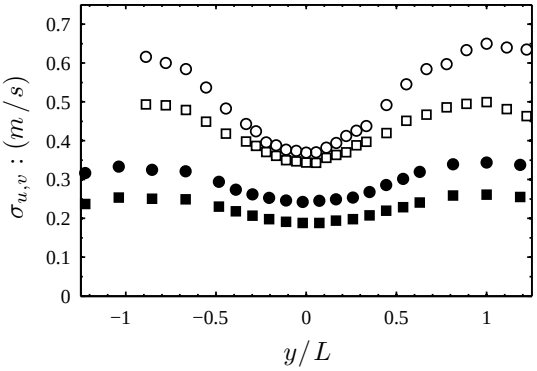

b) Turbulence r.m.s.

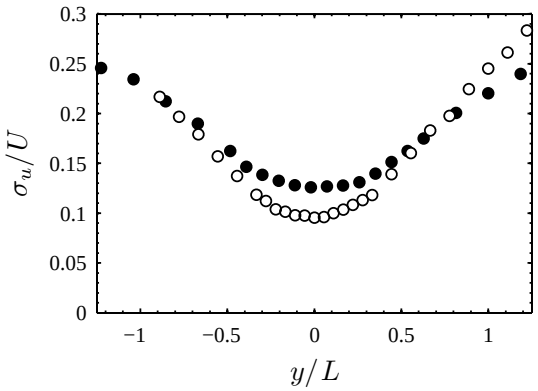

c) Turbulence intensity.

Figure 2.3: Profiles of the mean flow velocity (a) and turbulence r.m.s. (b) at the measurement planes for flows 1 (filled symbols) and 2 (open symbols), streamwise (circles) and transverse (squares) components. The turbulence intensity is shown in (c).

ter of the wind tunnel. As a result, inhomogeneity in σ declines (figure 2.5a). For the kurtoses, we note the off-center peak at $|y/L| \approx 0.3$ in $K_4(v)$ upstream of the measurement plane (figure 2.5b). Upstream of where the two turbulence regions interact, two local peaks in intermittency occur on the non-turbulence (grid gap) sides of the turbulence interfaces, where gusts of fluid cross into the weakly turbulent region. This is consistent with measurements of a turbulence-non-turbulence interface (Veeravalli and Warhaft, 1989). At the measurement plane, there is a single peak at the flow center, and downstream of this the flow

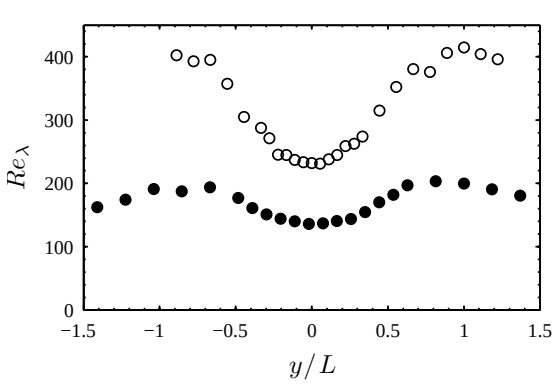

a) Taylor scale Reynolds number.

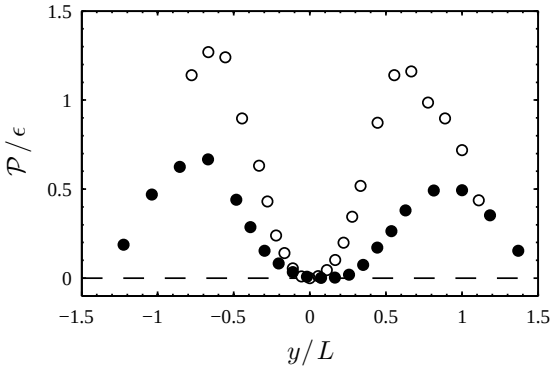

b) Production normalized by dissipation.

Figure 2.4: Dimensionless characteristics for flow 1 (filled symbols) and flow 2 (open symbols).

Table 2.1: Characteristic parameters for flows 1 and 2. Some values are reported for both $|y/L| = 0$ ($left$:) and $|y/L| = 1$ (: $right$).

Value	Flow 1	Flow 2
d : (cm)	15	20
X_K : (cm)	55	100
L : (cm)	13	20
U : (cm/s)	193 : 150	385 : 265
σ_u : (cm/s)	24.2 : 33.8	36.9 : 65
σ_v : (cm/s)	18.8 : 26.1	34.3 : 49.9
σ_u/σ_v	1.3 : 1.3	1.05 : 1.3
σ_u/U : $(\%)$	12.6 : 22	9.5 : 24
Re_λ	135 : 200	230 : 415
ϵ : $(m^2 s^{-1})$	0.185 : 0.345	0.35 : 1.03
ℓ : (cm)	7.7 : 11.2	14 : 27
η : (mm)	0.369 : 0.315	0.316 : 0.241

mixes out and the peak magnitude decreases. We reserve comment on the various features of the velocity moments for the analysis of the full profiles for flows 1 and 2 in the proceeding section.

The cross-correlations coefficients of u and v are shown in figure 2.6, defined as $\rho_{uv} = \frac{\langle uv \rangle}{\sigma_u \sigma_v}$. Peak magnitudes in the measurement planes are $|\rho_{uv}| \approx 0.4$ and $|\rho_{uv}| \approx 0.45$ for flows 1 and 2, respectively. These values match what are typical in the production regions of turbulent jets (Hussein et al., 1994) and in homogeneous turbulent shear flows (Tavoularis and Corrsin, 1981). Good symmetry is achieved in the flows; the kink at the flow 1 center suggests that the measurement plane may be slightly displaced from the streamwise location of peak intermittency. The discrete zero-value correlation region for flow 2 appears optimal for the intermittency, that is, the flow is most intermittent where the two shear layers which drive the strongest turbulence just meet. In this way, profiles of ρ_{uv} mark the flow evolution. This result was incidental, as the x locations of peak kurtoses were found directly from streamwise measurements along $y = 0$.

2.3.3 Velocity moments and intermittency

We examine the normalized moments of v at the measurement planes in figure 2.7, which shows the skewness, $S_3(v) \equiv \langle v^3 \rangle / \sigma_v^3$, kurtoses, $K_4(v)$, super skewness, $S_5(v) \equiv \langle v^5 \rangle / \sigma_v^5$, and super kurtoses, $K_6(v) \equiv \langle v^6 \rangle / \sigma_v^6$. The odd moments are zero at the flow centers as expected from symmetry, and the profiles are antisymmetric in y (figures 2.7a and 2.7b). Local extrema occur at $|y/L| \approx 0.3$, and are of nearly 0.5 and 0.7 in magnitude for the flow 1 and 2 skewnesses, and of 5 and 8 in magnitude for the super skewnesses. Between the peaks in turbulence r.m.s.

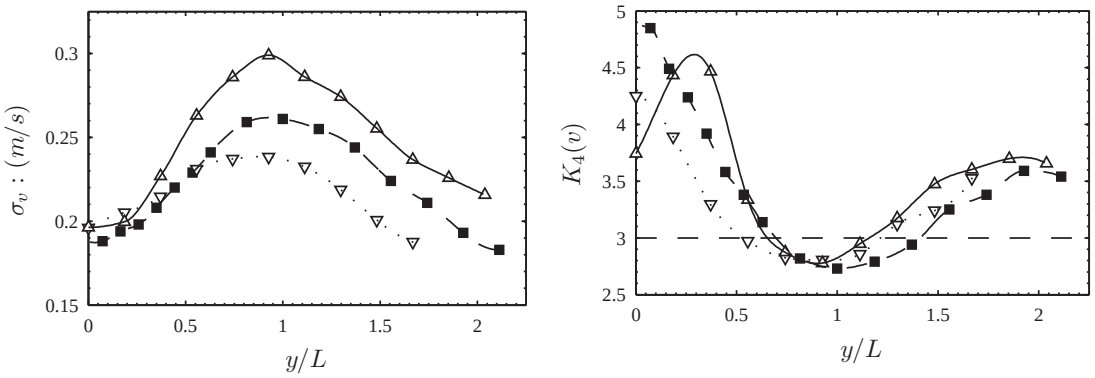

a) Transverse velocity r.m.s. b) Transverse velocity kurtoses.

Figure 2.5: Evolution of the second and fourth moments of v for flow 1. Upward- and downward- pointing triangles are profiles up- and downstream of the measurement plane ($x = (1 \mp 0.36) \cdot X_K$), while filled symbols are at the measurement plane. Curved lines connect the data points to clarify the flow evolution. (The flow 1 σ_v measurement plane data are the same as shown in figure 2.3b)

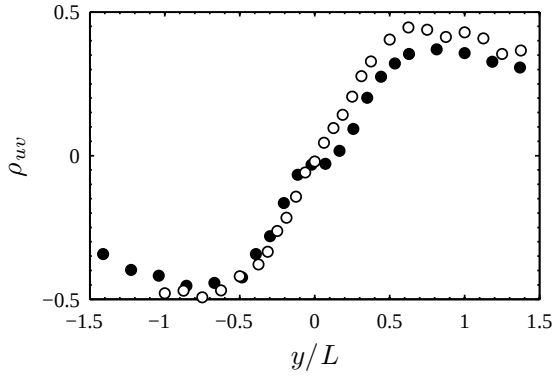

Figure 2.6: Cross-correlation coefficient, ρ_{uv}, for flows 1 (filled symbols) and 2 (open symbols) at the measurement planes.

(at $|y/L| \equiv 1$), the sign of the odd moments is opposite to that of y, with fluid bursting towards the flow centers from the outer, more turbulent regions. The odd moments are zero for both flows at the turbulence r.m.s. peaks, beyond which they switch sign as bursts of fluid from the regions with the strongest turbulence travel away from the σ-peaks and flow centers.

For the even moments of v (figures 2.7c and 2.7d), there are three extrema which correspond to the σ profiles (figure 2.3b). The turbulence is strongly super-Gaussian at the flow centers, with kurtoses of nearly 5 for both flows and super kurtoses of around 50 for flow 1 and 60 for flow 2. (The Gaussian value of K_6 is 15). Near $|y/L| = 0.9$, the turbulence is weakly sub-Gaussian ($K_4(v) \approx 2.8$ and $K_6(v) \approx 12$). This is consistent with the idea that the strongest fluctuations generally originate from furthest away (in a Lagrangian sense), and will be rare when the turbulence away from the measurement point is relatively weak.

It is evident from figure 2.7 that the odd moments of v go opposite the first spatial derivative, $\partial_y \sigma_v$, while the even go with the concavity, $\partial_{yy} \sigma_v$. (We define $\partial_y \equiv \frac{\partial}{\partial y}$ and $\partial_{yy} \equiv \frac{\partial^2}{\partial y^2}$). The skewness and kurtoses of v are plotted against the first and second spatial derivatives of σ_v in y in figure 2.8, and cross-correlation coefficients (indicating linearity) for the figure data are listed in table 2.2. The greatest error here is in estimating spatial derivatives of σ from discrete measurements. To this end, derivatives were calculated from σ profiles smoothed with polynomial fits. Despite this, we see strong linear trends between both the odd moments with $\partial_y \sigma_v$ and the even with $\partial_{yy} \sigma_v$. For all cases the cross-correlation coefficients are at least 0.9 in magnitude.

While the concavity, $\partial_{yy} \sigma_v$, is approximately equal in magnitude for both peaks and troughs in σ_v, the peaks measure as only weakly sub-Gaussian as

compared to the strongly super-Gaussian troughs. This is expected, as the absence of long tails in a pdf is far less influential on its normalized moments than their presence[5]. For the even moments, there is some bias towards weakly super-Gaussian values at the inflection points (figure 2.8b); here, the flow may remain intermittent due to skewness of v. While long, symmetric tails may cancel in the odd moments (hence we can have high kurtoses and zero skewness), asymetric tails won't necessarily yield Gaussian values of kurtoses. Given the observed linear relationship of the even moments on the concavity of σ (figure 2.8b), coupled with the fact that there is greater departure of the even moments from Gaussian values for super-Gaussian turbulence than there is for sub-Gaussian turbulence, the offset is required. The offset indicates added complexity to the relationship between the even moments and turbulence r.m.s., despite the strong linear trend, which may simply manifest itself in the observed vertical shift which likely corresponds to the skewness and/or gradient in σ at the inflection points. The two flows studied here may be insufficient to rigorously assess this point. We lastly note that the data in figure 2.8 trace figure eights moving between physically adjacent measurements; it is unclear whether this is simply due to calibration errors. Still, the trends in the data are convincing.

The moments of the streamwise component, u, are shown in figure 2.9. The behavior is symmetric and sub-Gaussian near the peaks in turbulence; this is similar to v. There are however notable differences in the grid gap region. As expected from symmetry, all moments here are symmetric in y, rather than antisymmetric, like the odd moments of v. The skewness of u, however, has three extrema. There are troughs in the skewness of -0.3 for flow 1 and -0.55 for flow

[5]With regards to the difference from the Gaussian value.

2 at $|y/L| \approx 0.4$, which correspond to the locations of the v odd moment extrema. The super skewness (not shown) likewise has troughs of -3 and -8 for flows 1 and 2, respectively. At the flow centers, however, the odd moments of u have local peaks for both flows 1 and 2. At $y = 0$, flow 1 has a skewness of approximately 0.2 and a super skewness of 2, while the flow 2 values are nearly zero. In this region, there is little streamwise gradient in σ, as convergence of turbulent kinetic energy from the mixing offsets its dissipation. We also note that the trends in u and v skewness are similar, excepting their sign.

In the case of the even moments of u (figure 2.9b), there are two peaks in the grid gap regions, roughly corresponding to the troughs in the odd moments. The u kurtoses peak at around 3.75 for flow 1 and 4.5 for flow 2, while the super kurtoses (not shown) peak at 25 and 45 for the flows. The values correspond well to the trends in v, with the exception of the dip in the flow centers, where the even moments of v grow to a single peak. This again may be associated with the weak streamwise variation in σ at the flow centers. The trends in $S_5(u)$ and $K_6(u)$ were similar to those of $S_3(u)$ and $K_4(u)$, respectively.

Finally, we look at the skewness and kurtoses of the velocity derivatives (figure 2.10). The derivatives are representative of the small scales of the turbulence, and have moments indicative of pdfs with exponential tails. The magnitudes of $S_3(\partial_x u)$, $K_4(\partial_x u)$ and $K_4(\partial_x v)$ are similar to measurements in homogeneous wind tunnel turbulence (Gylfason et al., 2004), particularly for flow 1. However, it is clear there is some interaction between the small scales and the large-scale intermittency in our flow, particularly for $S_3(\partial_x v)$. While the v derivative skewness is small in magnitude, as expected, the transverse variation is clearly (negatively) correlated to that of $S_3(v)$ (figure 2.7a). The kurtoses in figure 2.10 also show

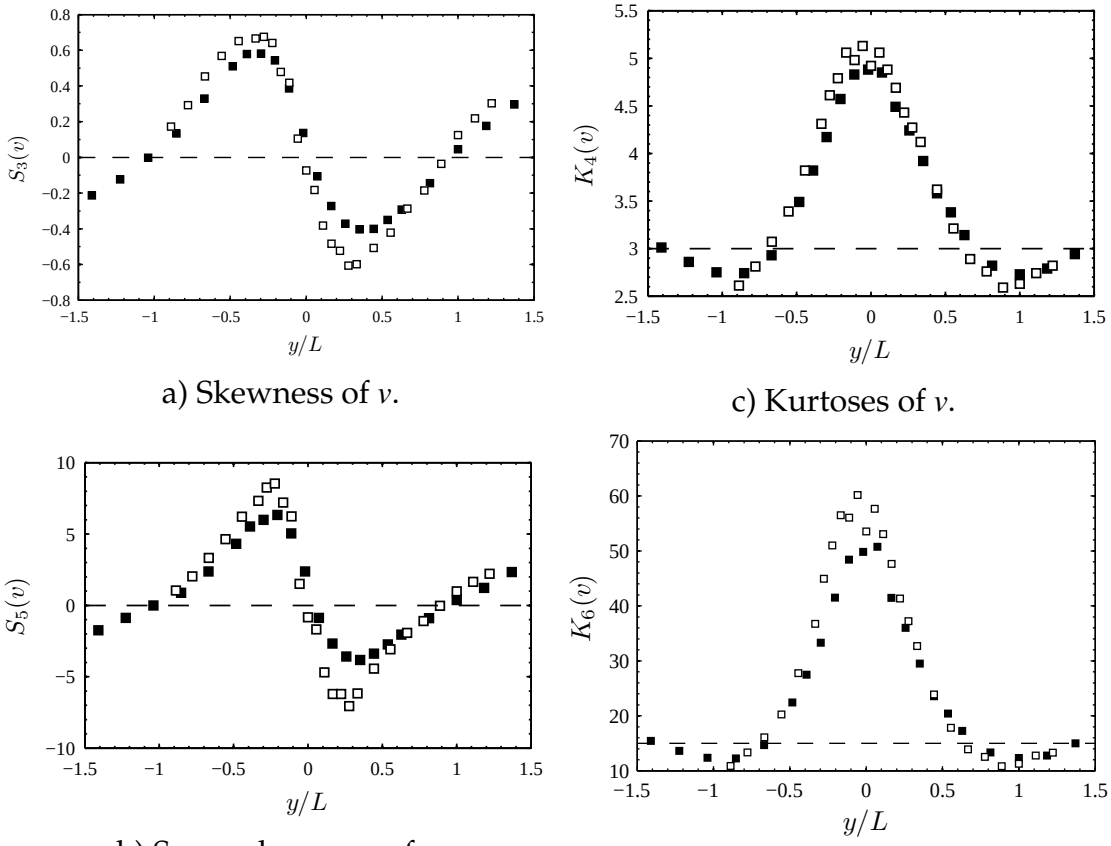

a) Skewness of v.

c) Kurtoses of v.

b) Super skewness of v.

d) Super kurtoses of v.

Figure 2.7: Normalized moments of v for flows 1 (filled symbols) and 2 (open symbols) at the measurement planes. The dashed lines are Gaussian values. (The flow 1 $K_4(v)$ data are the same as shown in figure 2.5b for one side of the flow).

increased values of the moments at the flow centers, and minimum values near $|y/L| = 1$, as for the velocity moments. $S_3(\partial_x u)$, , has positively-increased values at the flow centers. The interaction of the large and small scales has been documented in homogeneous shear flows (e.g. Shen and Warhaft (2000) and the references therein). In the present flow the interaction is more complex, and the large-scale intermittency has clearly played a role in determining the velocity derivative pdfs. These will be discussed further in the proceeding section.

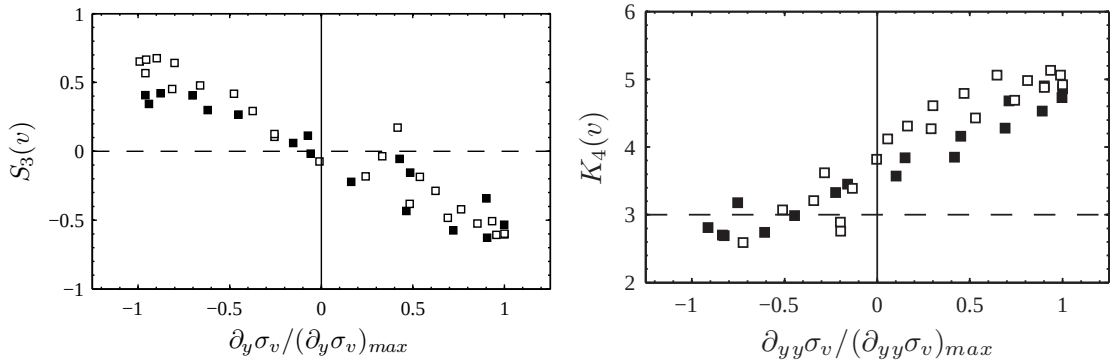

a) Skewness of v.

b) Kurtoses of v.

Figure 2.8: The skewness and kurtoses of v plotted against the y derivatives of σ_v for flows 1 (filled symbols) and 2 (open symbols). The dashed lines are Gaussian values and the solid lines are for homogeneous turbulence.

Table 2.2: Cross-correlation coefficients for the figure 2.8 data.

Cross-correlation coefficient (ρ)	Flow 1	Flow 2
$S_3(v)$ & $\partial_y\sigma_v$	−0.96	−0.97
$S_5(v)$ & $\partial_y\sigma_v$	−0.90	−0.93
$K_4(v)$ & $\partial_{yy}\sigma_v$	0.98	0.91
$K_6(v)$ & $\partial_{yy}\sigma_v$	0.96	0.90

2.3.4 Probability and spectral density functions

The probability density functions, $f(u)$ and $f(v)$ (figure 2.11), which encompass all of the moments described above, are shown at the two locations of nearly-symmetric turbulence, the local minima ($y \equiv 0$) and maxima ($|y/L| \equiv 1$) in the turbulence r.m.s. For v, the turbulence peak pdfs are nearly uniform between $\pm 1 \cdot \sigma_v$, and are otherwise weakly sub-Gaussian (figures 2.11a and 2.11b). At the flow centers, there are broad, long tails to the velocity distributions, being approximately three orders of magnitude above Gaussian values at $\pm 5 \cdot \sigma_v$ ($f \approx$

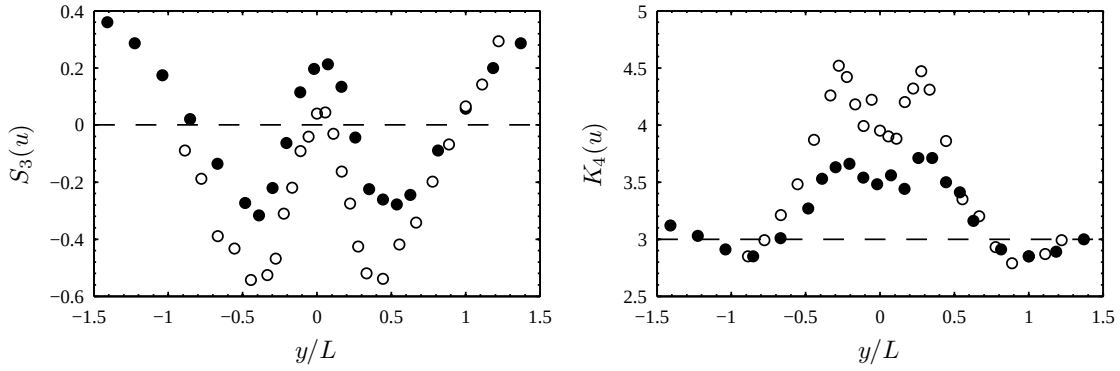

a) Skewness of u. b) Kurtoses of u.

Figure 2.9: Skewness and kurtoses of u for flows 1 (filled symbols) and 2 (open symbols) at the measurement planes. The dashed lines are Gaussian values.

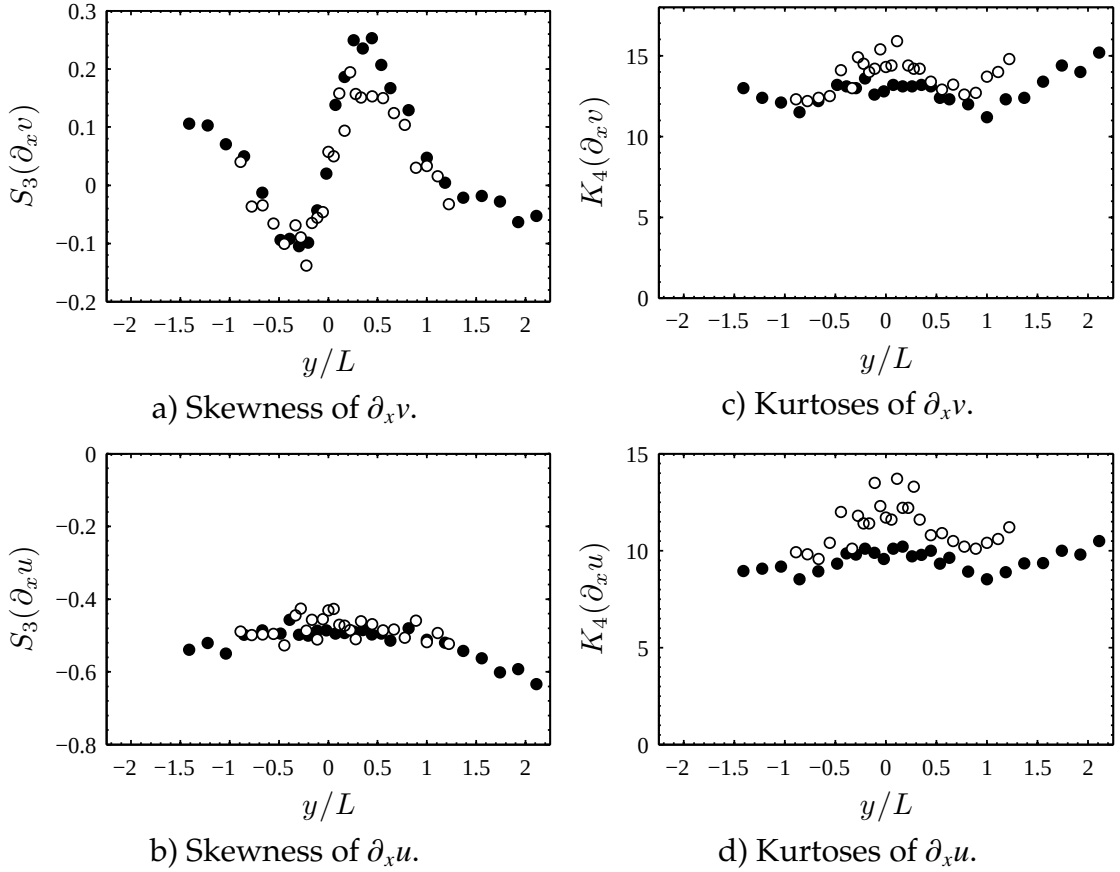

a) Skewness of $\partial_x v$. c) Kurtoses of $\partial_x v$.

b) Skewness of $\partial_x u$. d) Kurtoses of $\partial_x u$.

Figure 2.10: Normalized moments of $\partial_x u$ and $\partial_x v$ for flows 1 (filled symbols) and 2 (open symbols) at the measurement planes. The dashed lines are Gaussian values.

10^{-4}). We also note some bimodal behavior in the v pdfs at the flow centers, which have indents near $\pm 2 \cdot \sigma_v$. The corresponding u pdfs at the turbulence peaks are slightly skewed, but again weakly sub-Gaussian. At the flow centers the u pdfs are super-Gaussian like for v; in flow 1 it is slightly skewed, while for flow 2 it is clearly asymmetric (as reflected in $S_3(u)$ in figure 2.9a) with a pronounced bimodal turn near $-3 \cdot \sigma_u$.

Figure 2.12 shows the pdfs of the derivatives of u and v. The slight differences in width between the flow center and σ-maxima ($|y/L| = 1$) pdfs are in agreement with their kurtoses (figures 2.10c d). While the flow 1 and 2 difference can be attributed to the difference in Reynolds numbers, the difference between the flow center and σ-peak measurements is clearly due to the large-scale intermittency, as the σ peaks have the higher Re_λ (figure 2.4a). We anticipate that the $\partial_x u$ and $\partial_x v$ difference is also due to the increased intermittency of the v component. As previously indicated, the pdfs of $\partial_x u$ are negatively skewed.

Figures 2.13 and 2.14 show power and dissipation spectra (with dissipation scaling) for flows 1 and 2 at both $y = 0$ and $|y/L| = 1$. The noteable feature here is a bump reflected in both the u and v spectra at the low wavenumbers ($\kappa\eta \approx 2 \cdot 10^{-3}$), particularly at the flow centers (although it appears to be present at $|y/L| = 1$ as well). This bump probably indicates the intrusion of large scale motions which do not fit continuously with the local turbulent cascade. The "energy" spectra ($\kappa F(\kappa)$) confirm that the bump is not insignificant at the flow center, where the turbulence is strongly intermittent, and that it somewhat distorts the integral scale peak, since it is of similar scale. The bump stands out in particular in the dissipation spectra (figures 2.13b and 2.14b), where apparently this large scale, intermittent energy is not being transfered down the cascade.

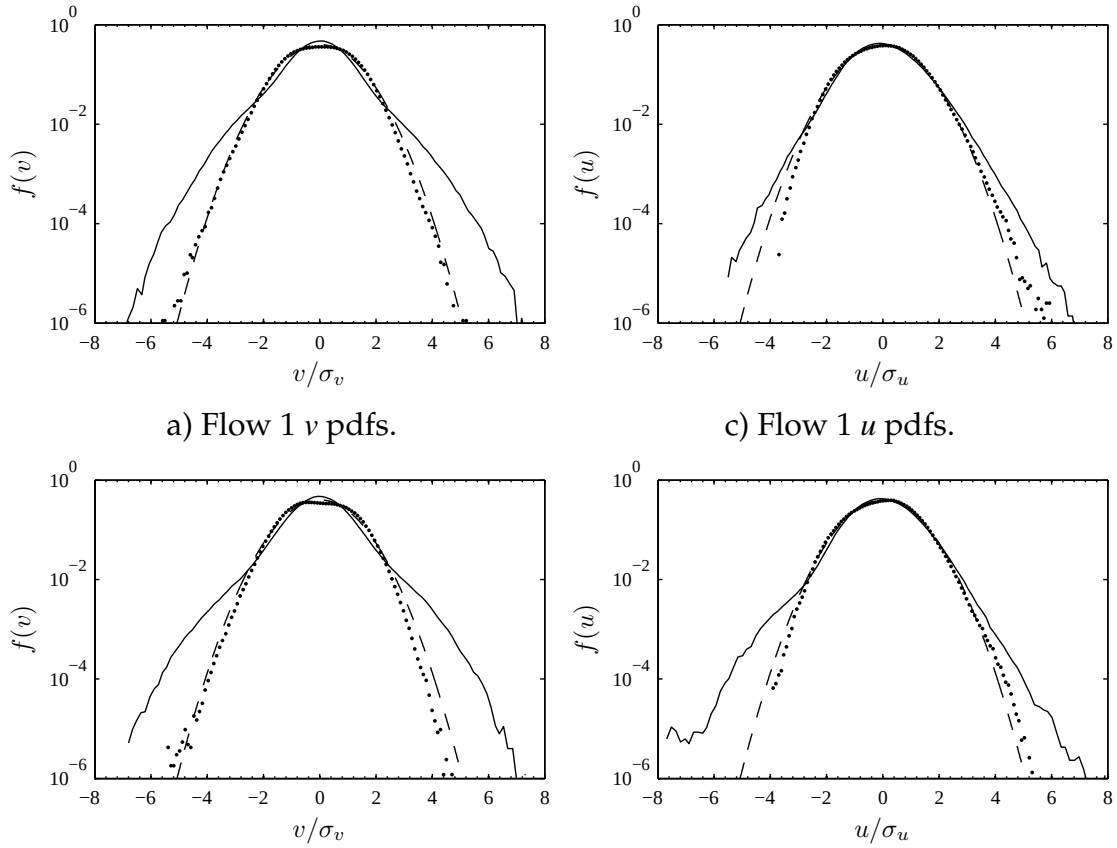

a) Flow 1 *v* pdfs. c) Flow 1 *u* pdfs.

b) Flow 2 *v* pdfs. d) Flow 2 *u* pdfs.

Figure 2.11: The pdfs of *u* and *v* in the flow 1 and 2 centers (solid lines) and turbulence peaks (dotted lines). The dashed lines are Gaussian values (3 for K_4 and 15 for K_6).

That is, the intermittent motions which are responsible for this intrusion have limited interaction with the surrounding turbulence. While our tunnel lacks a contraction and typically relies on the active grid to eliminate any noise from the inlet conditions, measurements at $x = y = 0$ showed no bumps in the spectra, and so we attribute these to the multi-scale nature of the flow.

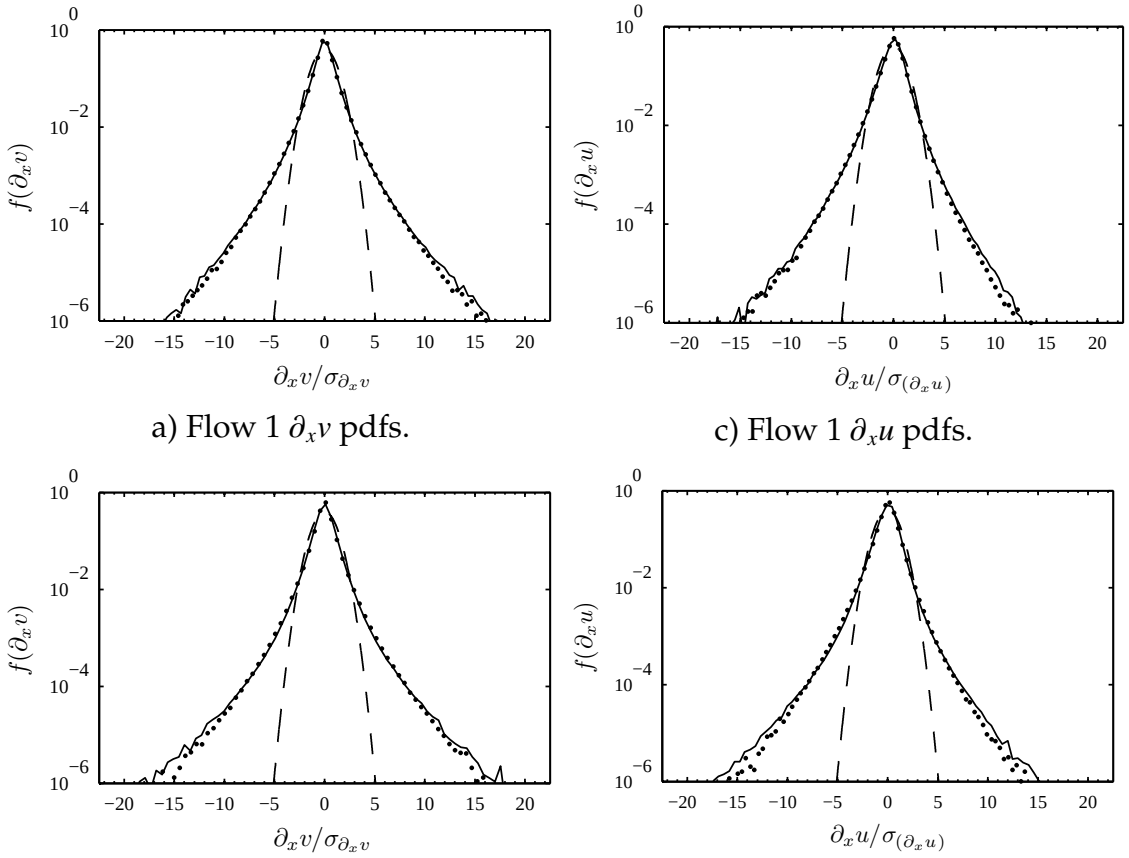

a) Flow 1 $\partial_x v$ pdfs.

c) Flow 1 $\partial_x u$ pdfs.

b) Flow 2 $\partial_x v$ pdfs.

d) Flow 2 $\partial_x u$ pdfs.

Figure 2.12: The pdfs of $\partial_x u$ and $\partial_x v$ in the flow 1 and 2 centers (solid lines) and turbulence peaks (dotted lines). The dashed lines are Gaussian values (3 for K_4 and 15 for K_6).

2.4 Discussion & Conclusions

Reports of extended tails in the probability distributions of turbulence statistics have not been limited to velocity derivatives. In fact, it has been shown that nonlinear theory predicts exponential tails in the pdfs of passive scalar fields if there is a mean scalar gradient (Pumir et al., 1991; Kerstein, 1991). In Jayesh and Warhaft (1991), this was demonstrated with measurements showing symmetric pdfs with strongly exponential tails having kurtoses peaking near 5 and super

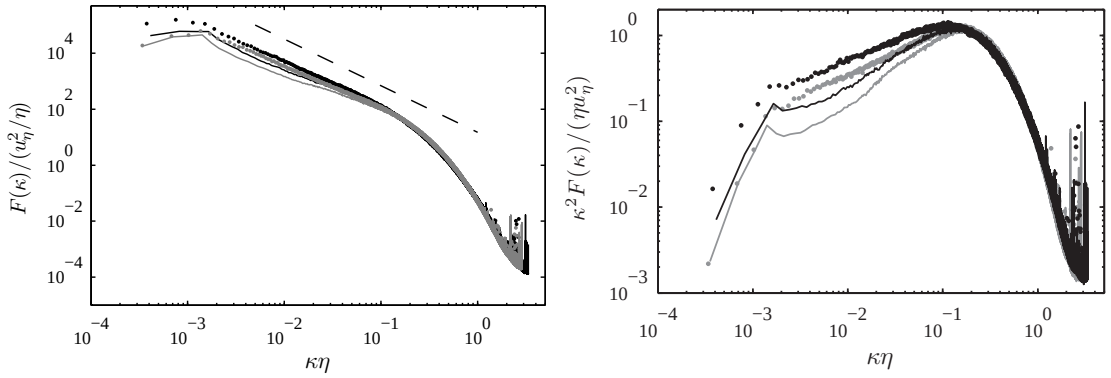

a) Flow 1 power spectra. b) Flow 1 dissipation spectra.

Figure 2.13: Flow 1 spectra of u (black) and v (gray) in the flow center (lines) and turbulence peaks (dots). The dashed line shows a minus five-thirds power law.

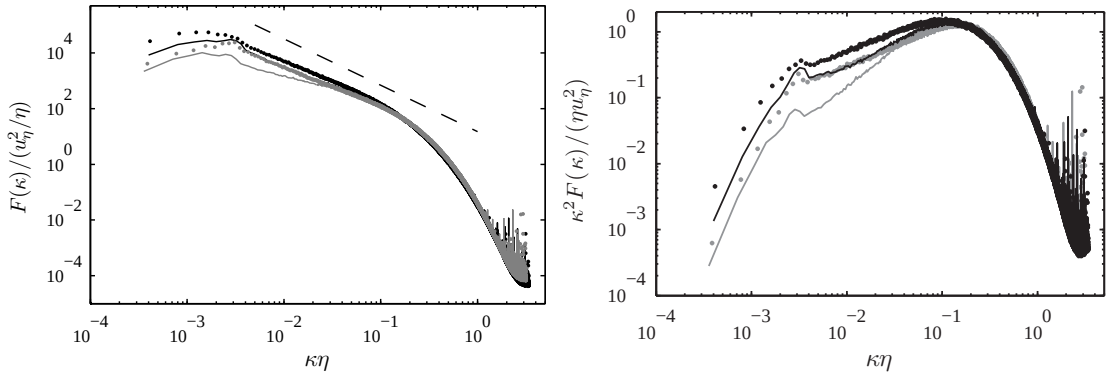

a) Flow 2 power spectra. b) Flow 2 dissipation spectra.

Figure 2.14: Flow 2 spectra of u (black) and v (gray) in the flow center (lines) and turbulence peaks (dots). The dashed line shows a minus five-thirds power law.

kurtoses peaking near 80. The scalar pdfs were similar to those shown for v in the present study (figure 2.7) up to $v = \pm 4 \cdot \sigma_v$, as indicated by their similar kurtoses. As mentioned in the introduction, velocity pdfs with stretched tails and bimodal behavior have also been reported, though have perhaps received insufficient attention. As a comparison of velocity pdf measurements, Jayesh and Warhaft (1991) showed velocity measurements immediately downstream (one

mesh length) of two passive grid bars. In this region, various pdf forms are observed, from box-like distributions with flat tops and sharp tails directly in the wakes of bars, to strongly bimodal, more Gaussian-like pdfs directly between them, with many others having long, skewed tails along the way. These various features, though less exagerated, are observed in the present study (figure 2.11).

The fractal grid community has reported strongly bimodal pdfs, very similar to those of the near-grid measurements (Jayesh and Warhaft, 1991). In the case of Mazellier and Vassilicos (2010), attention is drawn to regions of interaction between wakes of various grid bars, as the wakes of variously sized, variously spaced grid bars will meet at different downstream distances. This is similar to what was reported in Jayesh and Warhaft (1991). It is also qualitatively similar to the meeting of the two turbulent regions in our flows. In fact, our flow and grid gap are somewhat analogous to the near field between two (turbulence-generating) bars in a larger grid. In this way it is a *flow within a flow*. Like in many classical (e.g. the turbulent jet) and geophysical multi-scale flows, the intermittency in our flow is a result of the flow organization. In the case of environmental flows which are not limited to source-driven turbulence, like jets or wind tunnel flows, the inhomogeneity and multi-scale nature of the flow of course persist. It has been shown in the approximation of two-dimensional turbulence as a superposition of coherent vortices on a random background field, that these structures dominate the velocity field (Bracco et al., 2000a). The simulations of Bracco et al. (2000a) produced super-Gaussian, bimodal pdfs, as are observed in the ocean where long-lived coherent vortices and meandering jets produce organized, non-Gaussian flow fields (Bracco et al., 2000b).

The apparent coupling of the large and small scales in the present study (fig-

ure 2.10) is of particular interest regarding many multi-scale turbulent flows, such as those involving the interaction of sub-Kolmogorov scale particles. Take for instance the dependence of cloud evolution and droplet growth on the entrainment process at cloud boundaries, which is strongly intermittent. The role of turbulence in determining the rare events which trigger droplet collision and growth has sparked much interest in the fundamental study of inertial particle dispersion and dynamics (e.g. Siebert et al. (2010)), particularly of their accelerations and the small scale behavior. The dependence of the small scales (reflected in velocity derivative statistics) on large-scale inhomogeneity and intermittency is not well-understood, but has been clearly demonstrated here (figures 2.10). We expect that the pdf of the acceleration field, which is connected with the selective fluid sampling of inertial particles, will be similarly affected.

The necessary condition for Gaussian turbulence due to the central limit theorem, according to Mouri et al. (2002), is that the Fourier transforms of the fluctuating velocity components be independent of each other. In their study, the transforms were independent and near-Gaussian turbulence was observed at intermediate distances from a passive grid. In the near-field and far from their grid, this independence did not hold, where turbulence develops or decays, and is observed to be sub- and super-Gaussian, respectively. Mouri et al. (2002) attribute the sub-Gaussianity of the transverse velocity in the production region to quasiperiodic motions (while the streamwise velocity is super-Guassian by its intermittency), and reason that strongly super-Gaussian turbulence is observed in the decay region by the presence of intermitent, persistent large-scale structures. The correlation of the Fourier transforms was most obvious in a very sharp bump present in both the transverse and streamwise power spectra (Mouri et al., 2002). Low wavenumber bumps in the power spectra are also

found in the mixing and intermediate regions of turbulent jets (Fellouah et al., 2009). While not reported in these studies, also recall, pdf measurements in the very near-field of a passive grid show strongly bimodal pdfs (Jayesh and Warhaft, 1991). In the present study, less distinct bumps were shown in the measurement plane spectra, particularly where the turbulence was super-Gaussian and bimodal. The presence of energy in multi-scale turbulence with intermittent large scales which does not transfer down the cascade is of particular interest in its own light.

Super-Gaussian and weakly bimodal behavior of the turbulence measurements in our flow (figure 2.11) are themselves similar to atmospheric flows. Measurements in the atmospheric convective boundary layer by Alberghi et al. (2002), exploring the relationship of the skewness and kurtoses of the vertical velocity, show the skewness to range from 0 to 1 and the kurtoses from 2 to 5, similar to the present study. In the case of Alberghi et al. (2002), small and large skewness tended to correspond to sub- and super-Gaussian measurements of kurtoses. Velocity measurements in the atmospheric surface layer (Anfossi et al., 1996) show extended tails of similar width to those in our flows ($f(\pm 4 \cdot \sigma_v) \approx 10^{-3}$), with like bimodal trends. Boettcher et al. (2003) studied the statistics of wind gusts (the small scales of atmospheric turbulence), measuring the probability distributions of wind velocity increments over (and conditioned on) fixed time intervals. The results show highly exponential tails with widths like those of the small-scale statistics (e.g. $\partial_x u$) presented for our flow (figure 2.12). In a related effort, a new paper by Knebel et al. (2011) documents such incremental measurements under laboratory conditions in a novel active grid experiment which enhances the internal intermittency.

Elements of our flows are similar to the inversion present at the top of the atmospheric boundary layer, where there is a sharp, jet-like increase in mean wind speed coupled to a sharp decrease in turbulent kinetic energy (Caughey, 1982). It is well-known that turbulence here intermittently penetrates the ABL, and so the effect of the large-scale intermittency on the small scales is of particular interest.

In conclusion, we have described a new flow organized to produce a strongly non-Gaussian velocity field. The flow shares similar characteristics to a planar jet in freestream turbulence, the near field between bars in a standard grid, and geophysical flows. We have documented the moments of the flow velocity pdfs (figures 2.7 and 2.9), and have shown and described in particular their relationship to the spatial variation of the turbulence r.m.s. (figure 2.8). We find very strong linear trends between the odd moments and gradients in turbulence r.m.s., and between the even moments and the concavity of the r.m.s. field, confirming that super- and sub-Gaussian turbulence result from local troughs and peaks in the turbulence r.m.s., respectively. In inhomogeneous turbulence, inflection points in the r.m.s. field may still measure as intermittent due to the local skewness. We further found that the flow organization and the large-scale intermittency clearly affect the small scales and velocity derivative moments (figure 2.10), even at the relatively high Reynolds numbers of these flows.

The results are of interest to fundamental research in multi-scale flows. They should also be relavent to wind turbines, where it is often assumed that the incepted wind field is Gaussian, thereby strongly underestimating the effects of rare gusts. Such intermittency often occurs here because of the interaction of the ABL and free atmosphere.

We would like to thank Todd Cowen for the use of the DeFrees Hydraulics Laboratory wind tunnel. This work was supported by the US National Science Foundation.

CHAPTER 3

INTERMITTENCY AND INERTIAL PARTICLE ENTRAINMENT AT A TURBULENT INTERFACE: THE EFFECT OF THE LARGE-SCALE EDDIES[1]

We present measurements of mean and conditional number densities, radial distribution functions (r.d.f.s), velocities and accelerations of sub-Kolmogorov-scale water droplets entraining at a shearless turbulence-turbulence interface (TTI) and a turbulence-non-turbulence interface (TNI). We thus look at statistics of an inhomogeneous inertial particle field in both homogeneous and inhomogeneous turbulence. As in a previous communication (Gerashchenko et al., 2011), an active grid produces high-Reynolds number turbulence ($Re_\lambda = 275$) on either one or both sides of a splitter plate in a wind tunnel. Sprays seed droplets on one side of the splitter plate, while screens dampen turbulence in the adjacent flow for the TNI. Gravitational and inertial effects are isolated by turning of the apparatus with respect to gravity. We parameterize the droplets under homogeneous conditions, where it is demonstrated that both the sweeping and loitering effects on the droplet settling velocities are present. In the inhomogeneous conditions, we show that the droplets are entrained in bulk, resulting in large-scale clusters and preserving the droplet-ambient conditions of the seeded side of the flows.

3.1 Introduction

Entrainment, the means by which turbulent flows spread and grow, is fundamental to all turbulent flows with interfaces, be they interfaces with a laminar

[1]by G. H. Good, S. Gerashchenko and Z. Warhaft; *J. Fluid Mech.*, Volume 694 (March 2012), pp. 371-198.

flow, or another turbulent flow with different properties (e.g., length and energy scales). The subject has been extensively studied in traditional turbulent shear flows (e.g., Townsend, 1976) for both the velocity and passive scalar fields, and for reactions (e.g., Broadwell and Breidenthal, 1982). There have been entrainment studies of turbulent plumes (Turner, 1986), the atmospheric boundary layer (Deardorff, 1974), stable density interfaces (Kantha et al., 1977) and clouds (Shaw, 2003; Andrejczuk et al., 2004). Yet, while a significant amount of numerical and experimental work has been done for the above-mentioned cases, comparatively little is known about the entrainment of inertial particles, particles which are heavier than their surrounding fluid, such as the water droplets in clouds, the droplets formed by spray injectors, or the soot particles formed due to incomplete combustion in diesel engines.

While detailed knowledge is lacking on the entrainment of inertial particles, considerable work has been done on the effects of turbulence on their settling velocities (e.g., Aliseda et al., 2002; Wang and Maxey, 1993; Murray, 1970; Nielsen, 1993), their small-scale clustering in isotropic conditions (Squires and Eaton, 1991; Wang and Maxey, 1993; Sundaram and Collins, 1997; Wood et al., 2005; Saw et al., 2006; Salazar et al., 2008), their inertial-scale density fluctuations in isotropic conditions (Bec et al., 2007) and their mixing and preferential concentration in complex flows (Lázaro and Lasheras, 1989; Longmire and Eaton, 1992). It is our objective here to extend these investigations to explore the effects of entrainment on inertial particle fields. Our study follows on from the earlier experiments of Gerashchenko et al. (2011), here forth denoted as GGW.

The smoke-wire photo in figure 3.1 illustrates the type of entrainment process we are concerned with. The photo shows no droplets, but rather a turbulent

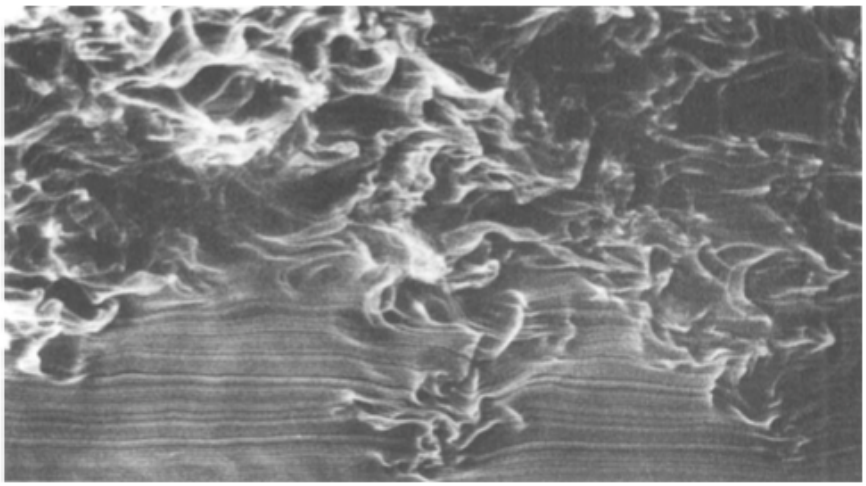

Figure 3.1: Smoke-wire image from Jayesh and Warhaft (1994) demonstrating large-scale intermittency at the interface between a highly turbulent and relatively quiescent flow. This is like the TNI case in the present work, albeit in Jayesh and Warhaft (1994) the flow was created using a combination of a passive grid and damping screens, and there were no droplets.

flow (above) which entrains fluid from the adjacent, quiescent flow below it. At the interface, the velocity field is intermittent at the large scales. We ask: what is the case when the turbulent side of the flow is droplet-laden, like at the boundary of a cloud? Might the particles entrain and cluster at the large scales? What is the role of gravity and inertia, and how will the entrainment affect the particle dynamics, size and spatial distributions? How dependent might such large-scale clustering be on the nature of the entraining velocity field? That is, what is the difference in the clustering characteristics of a particle field which has been entrained from a droplet-laden, turbulent region into a dry region which is in one case non-turbulent (figure 3.1) and in another having the same turbulence as the droplet-laden fluid?

We examine these questions by looking at two shearless interfaces, a homogeneous, turbulence-turbulence interface (TTI), and a turbulence-non-

turbulence interface (TNI), similar to that in figure 3.1. In our flows, water droplets are injected into intense grid turbulence on one side of a splitter plate; the adjacent, droplet-free flow is either equally turbulent or nearly laminar. Downstream of the splitter plate an interface forms. In the preliminary study of GGW, the mean particle density and size profiles were reported, as was some information on the mean particle velocities. Gravitational and inertial effects were isolated by turning the apparatus with respect to the gravitational field. It was shown that in the absence of gravity, the droplet size distribution did not change across the interfaces. This means firstly that the large scales (which could not distinguish between the variously sized droplets based on inertia) are responsible for the entrainment, and secondly, that the particle-laden side of the flow is entrained in bulk, such that the air ambient to the droplets remains saturated and they do not evaporate. When gravity was directed across the interfaces in GGW, the droplets were selectively transported based on their size. The TTI droplet mean number density profiles were error functions, while the TNI profiles indicated a sharper fall-off in the droplet mean number density. The mean velocity measurements of the particles showed enhanced bulk particle transport for the TTI as compared with the TNI, but they were unable to discern the effects of gravity.

In the present study, we use the same flow facility as in GGW to investigate the entrainment mechanism and address the questions we have posed above. Here, we have expanded the use of the word "entrainment," which may typically describe the drawing in of quiescent fluid by a turbulent flow (like at the TNI, as in figure 3.1). We expand its use to include the entrainment of particle-free fluid by a particle-laden flow with even the same turbulence (as in the TTI), since we will show that the effect of the large eddies on the particle field has

much in common with the classical entrainment situation. To this end, we examine the particle velocity field, including the higher-order moments, the particle radial distribution functions (r.d.f.s), conditional statistics and acceleration measurements. Apart from background information and a reexamination of the droplet mean number density data shown in GGW, all of the results presented here are new.

The outline of the paper is as follows: In § 3.2 we describe the experimental apparatus. This is followed by the results section. We first provide documentation on the velocity field, including higher-order moments and spectra, before describing the properties of the droplets in homogeneous conditions. We show that the settling speeds of the polydispersed droplets may be either enhanced or reduced with respect to their Stokes velocities, due to the competing effects of the turbulence on particle settling (Nielsen, 1993), as discussed in § 3.3.2. After parameterizing the droplets, we turn our attention to the inhomogeneous particle fields of the droplet mixing layers, and investigate their mean number density profiles, radial distribution functions (r.d.f.s) (defined in § 3.3.3) and some conditional statistics. This is followed by an analysis of the droplet velocity and acceleration data. In particular, we discern the subtle effects of gravity and inertia on the particle field, and show that within the intermittent, large-scale clusters which contain most of the droplets in the initially dry sides of the flows, the particle and fluid conditions are similar to those in the droplet-laden side.

3.2 Experimental Setup[2]

The experimental set-up is the same as in GGW. It allows for six different configurations — two flows with three gravity cases each. The wind tunnel is divided with a splitter plate and water droplets are injected via sprays into strongly turbulent flow on one side (figure 3.2), downstream of an active grid (Mydlarski and Warhaft, 1996; Kang and Meneveau, 2008). The adjacent, droplet-free flow is made either turbulent or non-turbulent by means of the same active grid or damping screens. Downstream of the 2.5 m splitter plate there is either a TTI or TNI, and a mixing layer develops. The mixing layer is kept shearless in both cases, such that only turbulence-turbulence interactions are present (GGW; Veeravalli and Warhaft, 1989). The sprays consist of three 1 mm diameter coflowing air and water nozzles, placed 5 cm downstream of the active grid (Gerashchenko et al., 2008). As shown in Gerashchenko et al. (2008), by the time the droplets reach the test section the effect of excess momentum produced by the sprays is diluted such that no abnormalities in the mean profiles are observed. The flow configurations (figure 3.2) may be rotated by 90 and 180 degrees such that the splitter plate is horizontal and gravity either aids ($g+$) or impedes ($g-$) droplet transport into the adjacent flow, or is vertical such that gravity is orthogonal to the mixing layer ($g0$).

The longitudinal and transverse coordinates are defined as x and y, with the origin at the splitter plate trailing edge; positive y values denote distance into the droplet injection region. The test section is at $x = 1.17$ m, which is 0.7 large-eddy turnover times from the splitter plate trailing edge. The mean

[2]Additional details of the experiments and data analysis are provided for the thesis in Appendix A

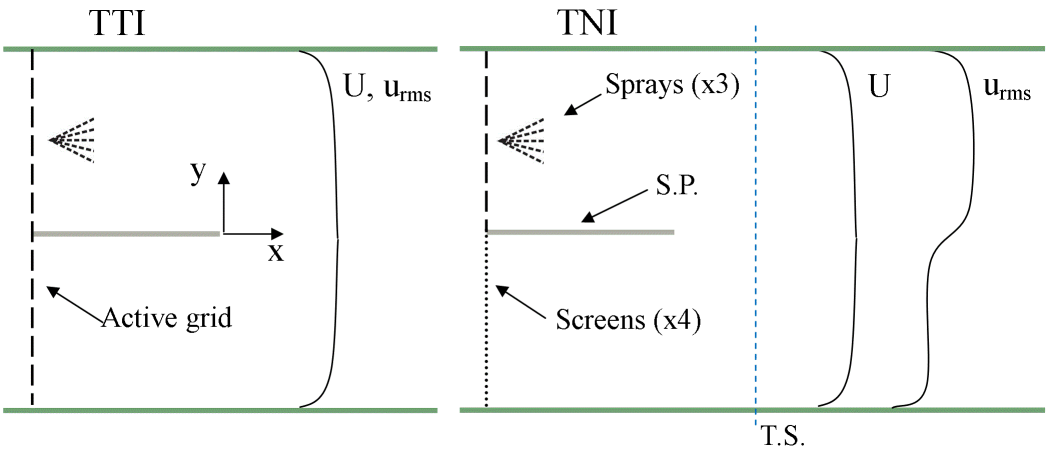

Figure 3.2: Sketches of the TTI (left) and TNI (right) flow apparatus. For the sketches, the $g+$, $g-$, and $g0$ cases are with gravity directed down, up and into the page, respectively. The active grid (black dashed line) has mesh length 10 cm, while the screens (dotted line) have mesh length 2 mm. Sprays inject droplets into the turbulent side of the flows. The splitter plate (SP) is 2.5 m long and the test section (TS), where the bulk of the measurements are done, is 1.17 m beyond its trailing edge.

tunnel velocity is $U = 2.15\ ms^{-1}$, with fluctuating longitudinal and transverse components defined as u and v, respectively. The negative of the transverse velocity, $-v$, will be presented in figures such that mean transport across the mixing layers is seen as positive. Fluid velocity components were measured using a hot-wire anemometer X-array with $3.05\ \mu m$ tungsten wires (Mydlarski and Warhaft, 1996). Droplet size, velocity and linear (one-dimensional, 1D) density statistics were measured with a two-component Phase Doppler Particle Analyzer (PDPA, TSI Inc.). Within the droplet-laden side of the flows, the air is saturated or nearly saturated and calculations show evaporative effects to be negligible. Droplet size distribution measurements at both the initial condition and test section confirm this. Given the flight time of the particles to the test section, calculations do show that a droplet in the ambient conditions of the dry side of the flows should experience severe evaporative effects, altering their

numbers and size distribution. The $g0$ droplet size profiles of GGW showed this not to be the case, however, and the reasons for this are the purview of the present study. Calculations also show the temperature differences across the interface to be too small to result in buoyancy effects. The small PDPA measurement volume ($300 \times 50 \times 50\ \mu m$) and seeding density ($m_{water}/m_{air} \approx 10^{-5}$) allow accurate velocity, size and number density measurements (Gerashchenko et al., 2008). PDPA and hot-wire measurements confirm that the particle and velocity fields are statistically homogeneous in the z direction, that is, parallel to the splitter plate trailing edge. The number of PDPA droplet measurements depended on the location, but they were generally of order 10^4 for the number density and 10^5 for the velocity data. The difference is due to the periodic need for number density reference measurements due to long-time fluctuations in the spray output.

Some droplet acceleration measurements are also shown. These were performed using a unique, Lagrangian particle tracking system which utilizes a high-speed camera (Phantom v7.1) attached to a precision, linearly translating sled developed by Armann Gylfason (Ayyalasomayajula et al., 2006b). The sled is pneumatically driven at the mean flow speed in order to track particles over many frames. The sled moves outside of and parallel to the wind tunnel's glass walls. The camera delivered 8000 frames per second and its resolution was 512 $\times$ 512 pixels. The particles were illuminated by means of forward scattering from a laser beam (Nd-YAG, 20 W, pulse width 120 ns, 40 KHz pulse) connected to the sled via a fiber optic cable and projected in the Lagrangian frame. The forward scattering was achieved by reflection of the beam off of a mirror on the far wall of the tunnel, as in Gerashchenko et al. (2008). (For some measurements, a periscope assembly was introduced to the sled to measure at various y loca-

tions in the gravitational cases, where the splitter plate is horizontal). The particles were tracked over a distance of 50 *cm*, centered at the test section, through which the sled velocity is constant. This large measurement window (compared with the PDPA measurement volume) is necessary in order to achieve adequate particle tracks for determining accelerations statistics. Each movie is individually postprocessed by subtracting the minimum observed brightness for each pixel. The particle tracking algorithm developed by the Bodenschatz group (Voth et al., 2002; Ouellette et al., 2006) was used, and the accelerations were calculated by the convolution of the measured particle tracks with a Gaussian smoothing and differentiating filter (Mordant et al., 2004). The acceleration data shown are based on individual droplet acceleration measurements numbering on the order of 10^6.

3.3 Results

In this section, we characterize the air flows with hot-wire measurements, and this is followed by the droplet data, which were measured using both PDPA and Lagrangian particle tracking techniques.

3.3.1 The velocity field

We begin with velocity profiles of the TTI and TNI and use these to define the dominant turbulence scales. This is followed by an examination of the velocity spectra and the fluid velocity moments, the latter of which describe large-scale intermittency in the flows.

Re'_λ	$\epsilon' : (m^2 s^{-3})$	$U : (m/s)$	$u'_{rms} : (m/s)$	$v'_{rms} : (m/s)$	$T.I.' : (\%)$
275(12)	0.138(0.006)	2.15(0.05)	0.31(0.01)	0.24(0.01)	14.4(0.8)
$\lambda' : (cm)$	$\eta' : (mm)$	$\tau_\eta{}' : (ms)$	$u'_\eta : (cm/s)$	$\ell' : (cm)$	$\tau'_\ell : (s)$
1.3(0.04)	0.397(0.006)	10.5(0.3)	3.8(0.6)	24(2)	0.8(0.09)

Table 3.1: Flow Parameters in the TNI high turbulence, or equivalently, the TTI turbulence, as signified by the primes. The mean velocity does not vary across the shearless interfaces. The Taylor microscale and its Reynolds number are defined as $\lambda \equiv \sqrt{15\nu u'^2_{rms}/\epsilon}$ and $Re_\lambda \equiv u_{rms}\lambda/\nu$. The turbulence intensity, $T.I.'$, is defined as u'_{rms}/U.

The turbulence interfaces

Longitudinal, u, and transverse, v, velocity root mean square (r.m.s.) components are shown in figure 3.3, as is the turbulence dissipation rate, calculated as $\epsilon \approx 15(\nu/U^2)\langle(\partial u/\partial t)^2\rangle$ based on Taylor's hypothesis, where ν is the kinematic viscosity of air. The values are nearly constant across the TTI, while for the TNI, as shown by Veeravalli and Warhaft (1989), the profiles are approximately error functions. The turbulent kinetic energy ($k \approx \frac{1}{2}(u'^2_{rms} + 2 \cdot v'^2_{rms})$) ratio across the TNI is approximately 30, and the interface is thus dominated by the highly turbulent side of the flow and its scales (GGW). The transverse coordinate, y, is normalized by the integral length scale, ℓ', as determined from the longitudinal velocity spectra in the TTI (or the high-turbulence side of the TNI). Table 3.1 shows characteristic flow parameters at the test section, as measured in the high-energy turbulence of the TTI and the high-turbulence side of the TNI. Primes denote the (constant) values in this turbulence. The turbulence anisotropy, u'_{rms}/v'_{rms}, is around 1.3, consistent with Mydlarski and Warhaft (1996). The Kolmogorov eddy velocity and time microscales are defined as $u_\eta \equiv (\nu\epsilon)^{1/4}$ and $\tau_\eta \equiv \sqrt{\nu/\epsilon}$.

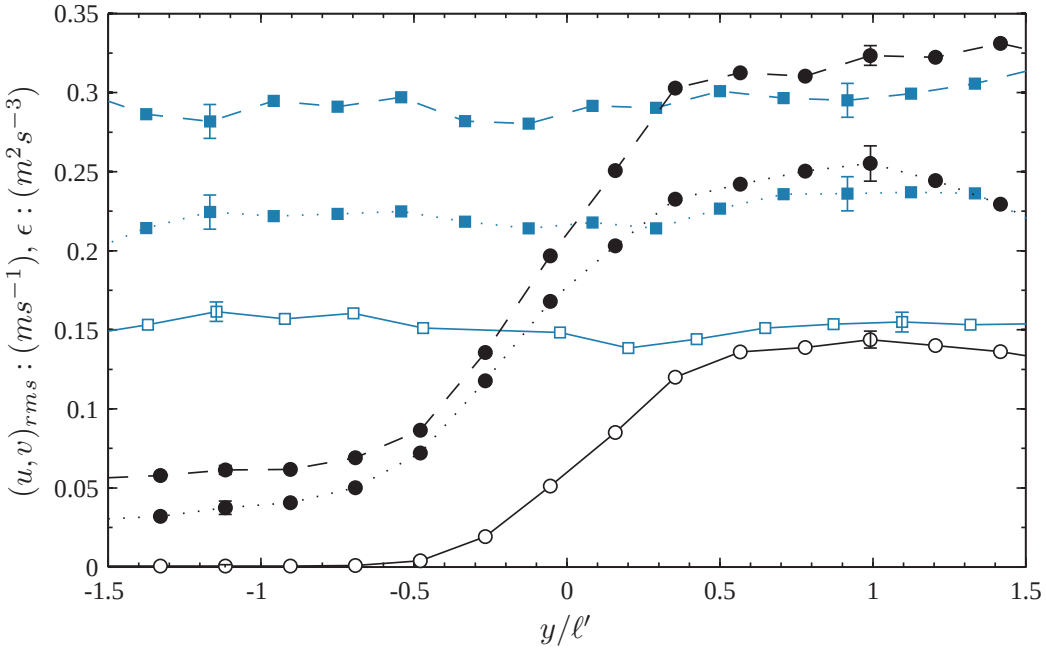

Figure 3.3: Hot-wire profiles of the velocity r.m.s. (filled symbols) and dissipation (open symbols) at the test section for the TTI (squares) and TNI (circles). The u and v velocity r.m.s. components have dashed and dotted lines, respectively. To avoid clutter, error bars are shown at representative locations only.

The velocity spectra

Figure 3.4a shows the longitudinal velocity power spectra, $F_{11}(\kappa)$, across the TNI, normalized with local dissipation scaling. Energy spectra, $\kappa F_{11}(\kappa)$, are shown in figure 3.4b, normalized by the high-turbulence side large-eddy scales. The spectra locations are denoted in the figure 3.4b inset, which also shows the variation of the mean dissipation length scale, $\eta \equiv (\nu^3/\epsilon)^{1/4}$. As the TNI is traversed from the high- to low-turbulence sides, the energy decreases. (This is most evident in figure 3.4b). However, there is some low-energy, large-scale noise on the low-turbulence side, present also at the initial condition. Its low energy suggests that it does not play a significant role in the turbulence dynam-

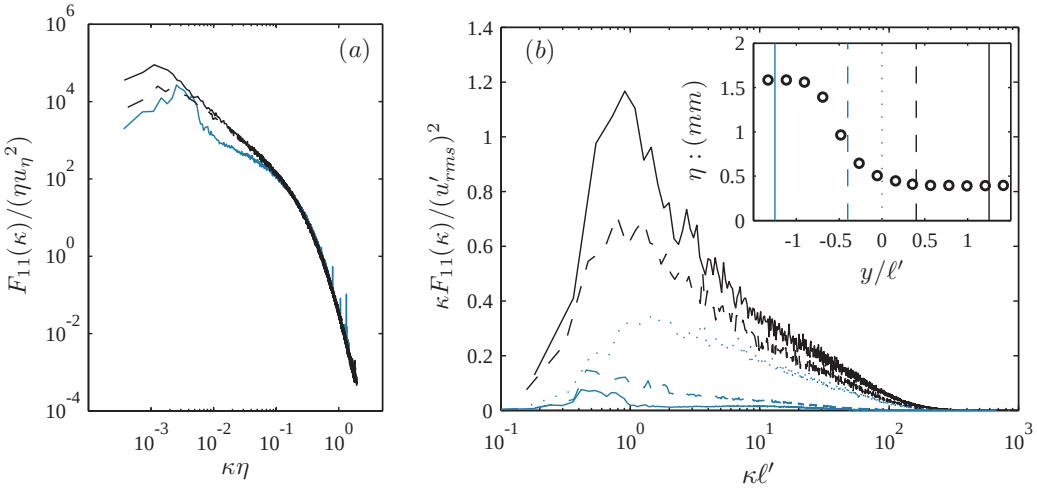

Figure 3.4: Power (*a*) and energy spectra (*b*) for the TNI, normalized with local dissipation scaling (*a*) and the high-turbulence side large-eddy scales (*b*). The inset shows the profile of η at the test section; vertical lines illustrate the locations of the spectra in the main figures ($y/\ell' \approx \pm 1.25, \pm 0.4, 0$), with lines from left to right in the inset corresponding to spectra from bottom to top in the figures. Only three power spectra are shown to avoid clutter from the collapse ($y/\ell' \approx -1.25, 0.4, 1.25$).

ics.

Large-scale intermittency and "bursting"

Figure 3.5 shows the normalized third and fourth fluid fluctuating velocity moments. For the TTI case these are close to Gaussian, as expected, while for the TNI case the values become strongly non-Gaussian and peak in the low-turbulence region. Peaks of skewness and kurtosis coincide and their displacement grows with the mixing layer, as does ℓ. There is additionally slight but monotonic growth in the peak magnitudes of both the skewness and kurtosis downstream of the splitter plate. At the test section the peak location is $y/\ell' \approx -1/3$, where intermittent, large-scale turbulent "bursts" penetrate into the

adjacent, quiescent flow, resulting in the strong departure from Gaussian statistics (GGW; Veeravalli and Warhaft, 1989). The bursting events dominate the low-turbulence-side velocity moments. As referred to in the introduction, figure 3.1 (from Jayesh and Warhaft (1994)) shows a smoke-wire image of a multi-scale interface between a very turbulent and relatively quiescent flow generated by a passive grid and damping screens in a wind tunnel. The interface is similar to the TNI. The fluid within the interface-penetrating, large-scale "bursts" is quite distinct from that in the quiescent region and appears to have the same turbulence characteristics as the flow above. In both the TTI and TNI, it is expected that the large scales which penetrate the interfaces are also particle-laden and will result in large-scale droplet clusters. (While such "bursts" for the TTI are indistinguishable in the velocity field, we show that they are distinguishable by their droplet content.) The role of the large scales and their intermittency in the droplet entrainment mechanisms for the TTI and TNI will be discussed in §§ 3.3.3-3.3.5.

3.3.2 The droplets in homogeneous conditions

Here, we describe the droplet size distribution as measured far into the seeded side of the flows at the test section ($y/\ell' \approx 1$). We call this the homogeneous region, as it has neither gradients in the turbulence mean quantities nor in the droplet mean number density. The primed values of tables 1 and 2 apply for all data here. The relevant droplet parameters are discussed, as is the resulting bifurcation in settling effects, whereby the turbulence enhances the settling of the small droplets while diminishing that of the large droplets as compared with their Stokes velocities.

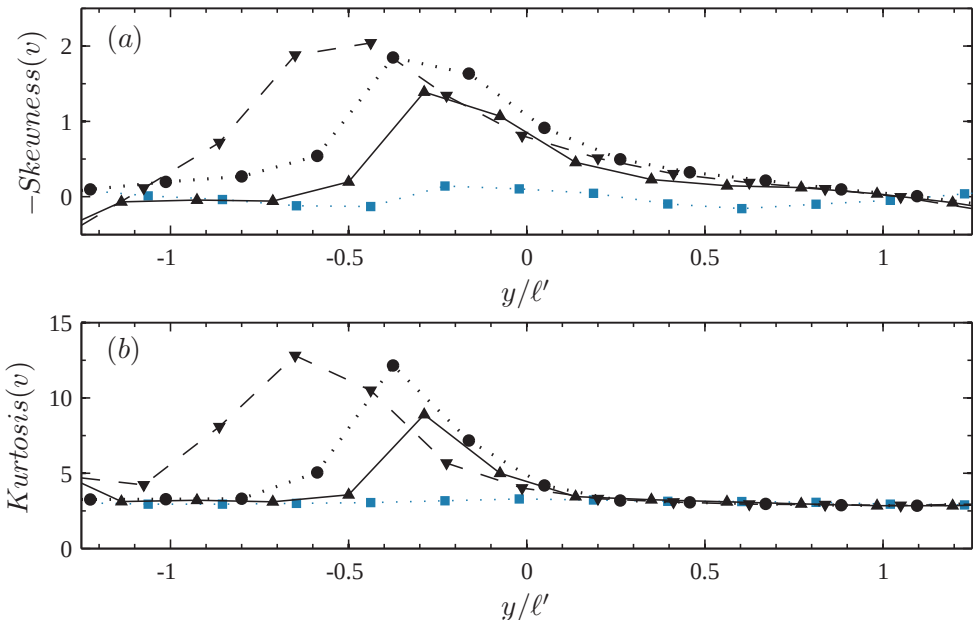

Figure 3.5: Profiles of the velocity skewness (a) and kurtosis (b). Squares are TTI profiles at the test section. TNI profiles upstream ($t/\tau_{\ell'} \approx 0.4$, $x = 0.7m$), downstream ($t/\tau_{\ell'} \approx 1.1$, $x = 1.8m$) and at the test section ($t/\tau_{\ell'} \approx 0.7$, $x = 1.20m$) are denoted by upward- and downward-pointing triangles and circles, respectively.

The droplet size distribution

Figure 3.6 shows the droplet size (diameter, d) distribution in the homogeneous region. For the purposes of the present study the distribution has been conditioned primarily into two groups, $d \leq 20\ \mu m$ and $d \geq 40\ \mu m$, here forth referred to as the small and large droplet groups, respectively (delineated in figure 3.6). The droplet group Stokes and settling parameters are listed in table 3.2, and are defined as $St_\eta \equiv \tau_p/\tau_\eta$ and $Sv_\eta \equiv \tau_p g/u_\eta$ for the Kolmogorov microscales, and as $St_\ell \equiv \tau_p/\tau_\ell$ and $Sv_\ell \equiv \tau_p g/v_{rms}$ for the large scales of the turbulence, where the particle response time $\tau_p \equiv \rho_p \langle d^2 \rangle / 18\mu$ and $\tau_\ell \equiv \ell/u_{rms}$. We note that while the full droplet size distribution can vary strongly as a function of y in the gravitational

Droplet Group	$\langle d \rangle : (\mu m)$	$\langle St_{\eta'} \rangle$	$\langle Sv_{\eta'} \rangle$	$\langle St_{\ell'} \rangle$	$\langle Sv_{\ell'} \rangle$
Small :	13.8(0.3)	0.061(0.002)	0.17(0.026)	$8(0.9) \cdot 10^{-4}$	0.026(0.001)
Intermediate :	27.2(0.3)	0.225(0.006)	0.61(0.01)	$3(0.3) \cdot 10^{-3}$	0.096(0.004)
Large :	51.2(0.5)	0.81(0.02)	2.2(0.3)	0.011(0.001)	0.35(0.01)
All :	22.7(0.7)	0.2(0.03)	0.54(0.01)	$2.8(0.1) \cdot 10^{-3}$	0.07(0.002)

Table 3.2: Droplet parameters in the injection side of the flows. Droplets with $d \leq 20$, $20 \leq d \leq 40$ and $d \geq 40$ μm belong to the small, intermediate and large droplet groups, respectively.

cases (due to the selective transport of the droplets, GGW), the variation is weak within the subdistributions presented here. Both the large- and small-scale settling parameters, $Sv_{\ell'}$ and $Sv_{\eta'}$, respectively (table 3.2), have order one values for the large droplets, and comparatively small values for the small droplets. The range of $St_{\eta'}$ values is similarly comprehensive; $St_{\ell'}$, however, is very small for all droplets, and so we do not anticipate that the large scales of the flow may effectively discriminate between the variously sized droplets due to their inertia.

Droplet settling

A number of mechanisms exist by which small, heavy particles may have their settling velocities enhanced or reduced in turbulent flows, and this requires some background. Settling enhancement may be facilitated via mass loading (Aliseda et al., 2002) or more generally via the "sweeping" or "fast-tracking"

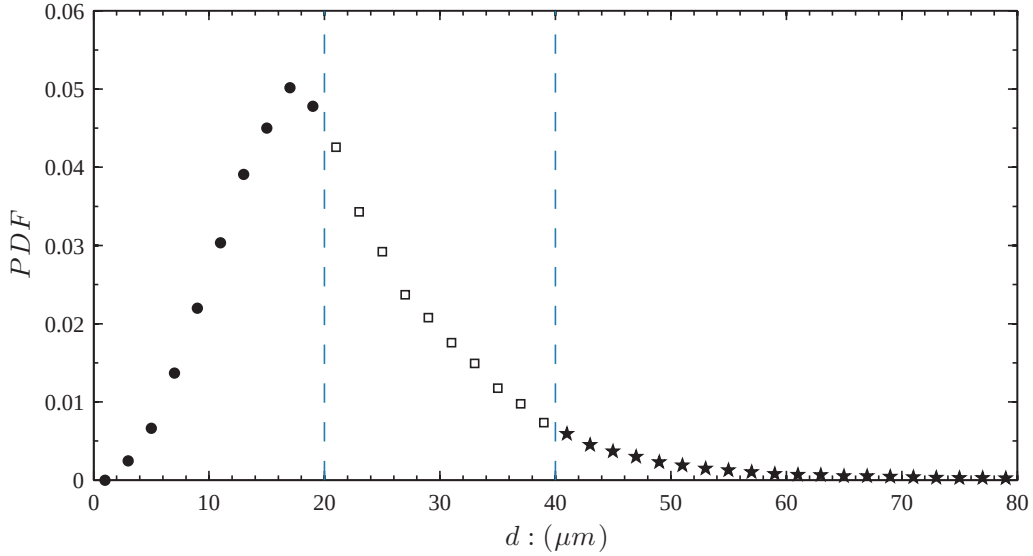

Figure 3.6: Normalized droplet diameter probability distribution as measured in the droplet bulk ($y/\ell' \approx 1$) at the test section. Circles, squares and stars represent the small, intermediate and large droplet groups, respectively, separated by dashed lines. This smoother PDF was measured under nominally the same conditions as that shown in GGW, but is based on substantially longer data sets consisting of hundreds of thousands rather than tens of thousands of measurements.

mechanism, by which falling particles show preference for the downward-sweeping sides of eddies. This mechanism has been well-documented in experiments (Aliseda et al., 2002), direct numerical simulations (DNSs) (Wang and Maxey, 1993; Hill, 2005), and theory (Dávila and Hunt, 2001). The effect is substantial for order one microscale Stokes and settling parameters (Wang and Maxey, 1993). The numerical simulations of Yang and Lei (1998), however, have also shown this effect to be strongly dependent on the large eddies.

Settling velocity reduction may be achieved for small, tracer-like particles by vortex trapping (Manton, 1974; Tooby et al., 1977), by nonlinear drag for large, heavy particles (Mei, 1994), or by the loitering effect. The loitering effect,

as described by Nielsen (1993), occurs when the turbulence is weak relative to the particle Stokes velocities, and thus the particles fall too quickly through the flow field to react to the eddies and spend more time on average in upward-moving regions of the flow. This may result in a mean settling velocity reduction of up to 40% when compared with a particle's Stokes velocity (Nielsen, 1993). Experiments (Murray, 1970; Nielsen, 1993; Kawanisi and Shiozaki, 2008) have shown the relevant parameter to be $S\,v_\ell$. Transition from settling enhancement to reduction occurs in the $S\,v_\ell$ range $10^{-1} - 10^{0}$, with the critical value varying with Stokes number (Kawanisi and Shiozaki, 2008). When the $S\,v_\ell$ number is sufficiently large, there is a return to the quiescent terminal velocity.

Our droplets are too heavy to undergo vortex trapping and are generally too small to undergo non-linear drag due to either large Reynolds numbers or significant deformation, with only the largest droplets having particle Reynolds numbers based on slip velocity (approximated as $Re_p \approx \frac{\tau_p g d}{\nu}$) greater than order 10^{-1}, or droplet Weber numbers ($We \equiv \rho_p v_{St}^2 d/\sigma$, σ being the surface tension) greater than order 10^{-2}. The droplet $S\,v_\ell$ range, however, is sufficient for both enhancement of the small droplet settling velocities by the fast-tracking mechanism and reduction of the large droplet settling velocities due to the loitering effect. This is shown in figure 3.7, where, following the Nielsen (1993) scaling, the settling velocity (W) enhancement is plotted as a function of $S\,v_\ell$ in the homogeneous region. (Whereas Nielsen (1993) adjusted turbulence levels in a flume seeded with monodispersed particles, in the present study we observe polydispered particles in a shared turbulent flow). Clearly, the measurements show a transition from settling enhancement to reduction to occur in the $S\,v_\ell$ range of $10^{-1} - 10^{0}$, and this is in agreement with Kawanisi and Shiozaki (2008).

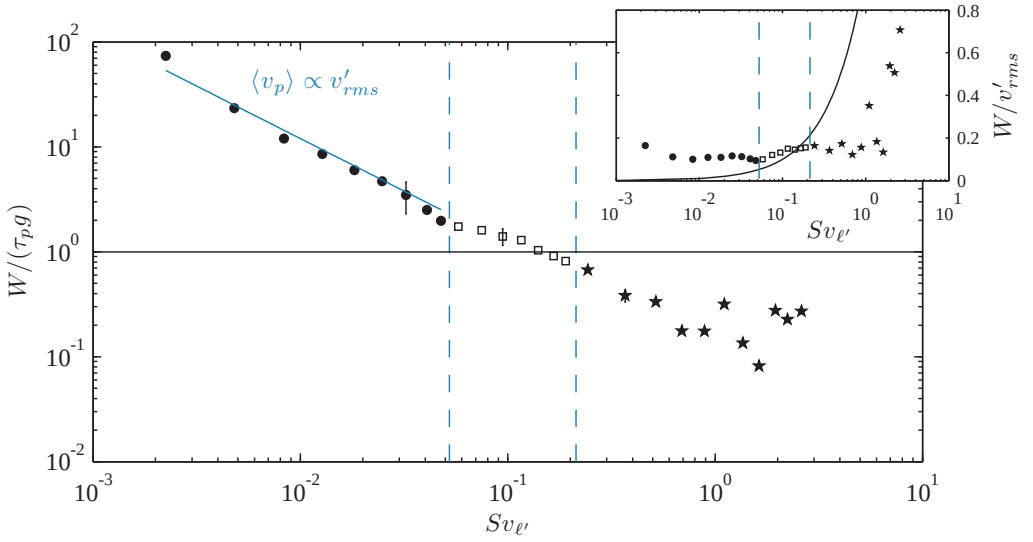

Figure 3.7: Settling velocity enhancement versus settling parameter, Sv_ℓ, in the homogeneous, high-turbulence side of the flows with homogeneous particle seeding. Black circles, open squares and stars represent the small, intermediate and large droplet groups, respectively. The inset shows the settling velocity normalized by v'_{rms}. The black line shows the droplet Stokes velocities. (Dissertation note: the settling velocities presented here (Good et al., 2012) do not correct for a weak background flow; in particular, this exaggerates the enhancement values for the small droplets).

To the best of the authors' knowledge, this is the first report of the loitering effect in wind tunnel turbulence. The loitering effect has been largely overlooked outside the fields of sedimentation and hydrology. For small Sv_ℓ, the turbulence is strong relative to the particle Stokes velocities. The settling speed of these particles is insensitive to differences in Stokes velocities, and is instead proportional to the velocities of the eddies which fast-track them. This is further illustrated in the inset to figure 3.7, where W/v'_{rms} is shown to be approximately constant up to $Sv_\ell \sim 1$. From the inset, $W/v'_{rms} \approx 0.1$, but there was variation between data sets, with some showing a proportionality constant closer to 0.2, although the same trend. These values are within the range documented by

Kawanisi and Shiozaki (2008). (The rising velocities of λ-scale, buoyant particles has also been shown by Friedman and Katz (2002) to be proportional to 25% of the turbulence r.m.s. velocity, regardless of Stokes number variation). For the large Sv_ℓ droplets in our flow (the scatter is due to the relatively low numbers of these droplets), there is the expected increase in W, although it always remains less than the droplet Stokes velocities ($\tau_p g$), as is clear from both the main figure and the Stokes velocities line in the inset.

The large-scale settling parameter, $Sv_\ell \equiv \tau_p g/v_{rms}$, may alternatively be expressed as $Sv_\ell \equiv \tau_\ell/(\ell/\tau_p g)$, the ratio of the characteristic time of a large eddy to the time for a particle traveling at its Stokes velocity to pass it, and the same interpretation is true for Sv_η and the interaction of particles with smaller eddies. Particles which fall too quickly through the flow field to effectively preference the downward-sweeping sides of eddies will experience a net reduction in their mean settling velocity, spending more time "loitering" in upward-moving regions of the flow than they do "fast-tracking" through downward-moving regions. Looking again to the figure 3.7 inset and the black line representing the Stokes velocities, it is clear that as a result of both the fast-tracking and loitering effects, the range of settling velocities observed for the droplet distribution is much diminished from what is predicted by Stokes drag.

Table 3.3 compares our parameter range with studies focused on particle settling. It is evident that there is large scale separation, $(\ell/\eta)'$, in the intense turbulence of the present flow. This is particularly true when compared with the well-known DNS study of Wang and Maxey (1993), but also with the experiments of Yang and Shy (2005). Particle loitering was not observed in Yang and Shy (2005), which has a similar Sv_ℓ range to the present study, but also

much greater St_ℓ values. Our large-scale droplet parameters are comparable with the flume study of Kawanisi and Shiozaki (2008). The settling parameters in our flow are considerably larger than in the passive grid turbulence study of Aliseda et al. (2002), while the droplet parameters are comparable in general with Wang and Maxey (1993).

3.3.3 The droplet mixing layers

We now turn to the particles in the inhomogeneous conditions of the droplet mixing layers, addressing both their mean droplet number density profiles and radial distribution functions (r.d.f.s). While the mean number density profiles describe the droplet mixing layers by their mean quantities, the r.d.f.s measure how the droplets are spatially distributed. We show that the mean droplet number density (n) evolves analogously to the (Fickian) diffusion of a concentration species. This is the case for both the TTI and TNI, despite the large-scale intermittency of the TNI. We also show the effect of the entrainment on the r.d.f.s, and lay the groundwork for the proceeding sections.

Mean droplet number density profiles

The mean droplet number density (n) profiles for the large and small droplet groups are shown for the TTI and TNI cases in figure 3.8. (The droplet number density is determined from the linear density of droplets measured by the PDPA, and normalized by the maximum value at that downstream location, n_{max}.) (Figure 4 of GGW shows profiles from the same data sets for the full distribution and for droplets with $d \geq 50\,\mu m$.) There are two important aspects: the

$Study$:	Present	Kawanisi and Shiozaki (2008)	Aliseda et al. (2002)	Wang and Maxey (1993)	Yang and Shy (2005)
$Type$:	Active Grid	Flume & KS	Passive Grid	DNS	FWM
Re_λ :	275	N/A	75	20 – 60	73 – 202
u_{rms}/u_η :	8	N/A	2.8 – 3.7	2.3 – 4.3	4.4 – 7.2
ℓ/η :	600	N/A	180 – 205	21 – 33	43 – 83
d : (μm) :	5 – 75	40 – 600	5 – 50	N/A	12 – 40
St_η :	0.007 – 6	N/A	0.01 – 5	1 – 2.7	0.36 – 1.9
Sv_η :	0.02 – 15	N/A	10^{-4} – 0.014	0.4 – 4	0.9 – 6
St_ℓ :	10^{-4} – .08	0.0003 – 0.06	10^{-3} – 0.1	0.002 – 0.012	0.01 – 10.4
Sv_ℓ :	10^{-3} – 2.5	0.05 – 5	< 0.005	0.1 – 1.7	0.12 – 1.4

Table 3.3: Comparison with studies on particle settling. Values are approximate, and for the present study reflect the full range shown in figures 7 and 8. In the flume studies showing bifurcated settling effects (Nielsen, 1993; Kawanisi and Shiozaki, 2008), we note that the turbulence r.m.s. was estimated from the particle r.m.s. velocities, which is reasonable for scaling purposes. Those statistics which are either not available or not applicable are listed as "N/A." For Kawanisi and Shiozaki (2008), KS stands for kinematic simulation. FWM denotes 'French washing machine', a general description of the air turbulence experimental apparatus of Yang and Shy (2005).

shape of the profiles and their relative positions (abscissa).

The mean droplet number density profiles for the TTI case are error functions (as reported in GGW). This indicates that for the TTI, n evolves to first order like any concentration species does from a step initial condition in a domain with a homogeneous diffusivity. The TNI case by contrast is strongly inhomogeneous, and so error function profiles of n are neither expected nor observed. The TNI n profiles (figure 3.8b) are overlaid with solutions from a simple, advection-diffusion model for n in a domain with variable (turbulent) diffusivity (as opposed to the homogeneous diffusivity of the TTI mixing layer), which is described in appendix B.1. The purpose of the model is to demonstrate what properties of the droplet mixing layers can be easily modeled, despite a number of simplifying assumptions and the complexities of both turbulent entrainment and multiscale turbulence. It is evident from the fits that the time evolution of the mean quantity n may be captured by a simple advection-diffusion model for the TNI, just like for the TTI.

The insets to figure 3.8 show the main figure fits artificially shifted to converge at the tails. Since the first-order effect of the particle settling on the n profiles (as a function of droplet size) is a lateral shift, we take their shape to be indicative of the turbulent mixing alone. Here, "mixing" is defined for the mean particle number density analogously as for a diffusive scalar, that is, as the ability of the flow and mean number density gradients to cause the mean number density field to become more uniform. A droplet mixing layer with a more gradual fall-off in its mean droplet number density is hence more effectively "mixed" than one with a steeper fall-off and narrower interface, regardless of abscissa. We see in the insets that there is some discernable change in the profile

shapes for the large droplets with gravity as compared with the small droplet and $g0$ cases. The large droplet cases have a sharper fall-off in n for the TTI and TNI $g+$ cases, but not for the TNI $g-$ case. The more gradual fall-off in n for the TNI $g-$ large droplet case can be explained by the fact that its droplets are shifted further into the high-turbulence side of the TNI. The large droplet $g0$ case has been omitted to avoid clutter. It was shown in GGW that for the g0 cases n is insensitive to droplet size, and thus that the large scales which do not effectively discriminate between the droplets due to their inertia (see $St_{\ell'}$ in table 3.2), dominate the entrainment. From the inset to figure 3.8a, however, it is apparent that the turbulent mixing may be sensitive to Sv_ℓ when gravity is directed across the interface, with the droplet number density effective diffusivities being diminished for the large droplets with gravity.

The relative shifting of the n profiles (figure 3.8) is of the order expected from gravitational settling (GGW). Apart from this, however, we also observed comparable shifts due to slight difference in the initial conditions for the flows, and these are discussed in appendix B.2. Valid comparisons of the profile abscissae may still be made within a given flow case, however. For example, the shift between the small and large droplet number density profiles is relatively small for the TTI $g-$ case as compared with the TTI $g+$ case. This indicates the broken symmetry of gravity aiding versus inhibiting the droplet transport.

Droplet r.d.f.s and conditional number densities

The r.d.f. is the established measurement of particle clustering, and is defined as the average density of the particles in a volume shell/slice at a fixed distance from a central particle, normalized by the mean density of the particles in

the domain (McQuarrie, 1976). Both the r.d.f., $g(r)$, and related pair correlation function, $h(r) \equiv g(r) - 1$, have been used to study the inertial clustering of heavy particles in homogeneous turbulence (e.g., Sundaram and Collins, 1997; Wood et al., 2005; Saw et al., 2006; Salazar et al., 2008). The r.d.f. is of particular interest in cloud physics because it contains vital information for predicting particle collisions (Shaw et al., 2002; Shaw, 2003). (Shaw et al. (2002) computed the pair correlation function for droplets both within a cloud and for traverses including ambient air). The 1D r.d.f. is defined as $g(r) \equiv (N_r/\delta r)/(N/L)$ (e.g., Holtzer and Collins (2002)), that is, the average number of particle pairs with separation distance r, (N_r, with a bin width of δr), normalized by the mean droplet linear number density, $n \equiv N/L$. The droplet separations were determined using Taylor's hypothesis and the Eulerian PDPA data.

The important features of our r.d.f.s did not differ qualitatively between the flow (TTI and TNI) and gravitational cases, nor between the droplet groups (except that the r.d.f.s are sensitive to the relative positions of the mean number density profiles of figure 3.8). Figure 3.9 thus shows r.d.f.s for the $g+$ small droplets only, as they are most numerous and their statistical error is lowest. Looking at the seeded region, ($y/\ell' \approx 1$), $g(r)$ is relatively uniform. This is particularly true for the small droplets, whose St_η (table 3.2) is too small for significant, small-scale inertial clustering. For the large droplets (not shown), the values do tend to increase for very small r, consistent with their order one St_η (Saw et al., 2006). Moving across the droplet mixing layers to negative y/ℓ', the magnitude of $g(r/\ell' < 1)$ increases strongly and monotonically, consistent with the decreasing mean number densities (figure 3.8). There is however a sharp decrease with r in the r.d.f. through $r/\ell' \approx 1$. This indicates that the droplets are organized into integral-scale clusters. There is a dip in $g(r)$ at $r/\ell' \approx 2$ to

subunity values which grows across the mixing layers. This dip is a result of the droplet-free gaps between the large-scale clusters. It is useful to refer back to the figure 3.1 image, imagining the turbulent bursts to be droplet-laden. The 1D $g(r)$ functions measure the droplet spatial distribution along lines tracing horizontally through the flow. The large-scale clustering is indicated where the lines trace through alternating droplet-free and droplet-laden regions of fluid. Since droplet-laden large scales penetrate both the TTI and the TNI, the large-scale clusters result for both, despite the absence of large-scale intermittency in the TTI velocity field. By clustering, we simply mean the state of the particle field as being spatially correlated rather than randomly distributed. While the large-scale clusters might be expected (and a passive scalar would likely behave in a similar way to the particles), it is not entirely obvious since it is not clear how the time scale of the formation of such clusters compares with that of their breakup/dispersion as a result of the ambient turbulence.

The large-scale clusters are observed for both the small and large droplet groups. Unlike for inertial clustering, large-scale clusters due to entrainment should persist as $St \to 0$. In fact, the mechanism should only be less effective for very heavy particles as $St, Sv \to \infty$, since such particles may not effectively follow turbulent bursts across the interface. We expect some differences in the clustering for the large and small droplet groups in the presence of gravity due to their Sv_ℓ values (table 3.2). This is difficult to determine with our r.d.f.s, however, since the two droplet groups can have very different local mean number densities in the gravitational cases.

The sharp increases in $g(r)$ for $r/\ell' < 1$ (figure 3.9) are clearly due to the declining mean number densities (figure 3.8), but the question remains as to

whether the properties within the large-scale clusters remain unchanged. While figure 3.9 presents the r.d.f.s in the typical fashion, it is instructive in our case to correct for the mean number density differences at each y/ℓ' location by multiplying the r.d.f.s by n/n_{max}. This is done in figure 3.10, which allows us to see the density changes in the mixing layers of droplet pairs with various separation distances. The values at the right end of the r/ℓ' axes in figure 3.10 show the local mean number density (since $\lim_{r\to\infty} g(r) = 1$), while the values on the left extreme ($r/\ell' \ll 1$) essentially show the droplet densities within the large-scale clusters. While the droplet mean number densities at $y/\ell' = -1/2$ are one and two orders of magnitude less than that in the source region for the TTI and TNI (figure 3.8), respectively, the droplet densities within the large-scale clusters only appear to be diminished by tens of percents. The droplet densities are thus largely preserved within the large-scale clusters in the entrainment zone.

Figure 3.11 shows conditioned profiles of the mean droplet number densities for the TTI and TNI $g0$ cases; the unconditioned mean number density profiles are also shown for comparison. For the conditioned profiles, the large, droplet-free spaces in the droplet measurement time series are ignored in calculating the mean number densities. These spaces are identified using a threshold value of the largest droplet separations in the seeded side of the flows, where there are no large-scale droplet clusters. The conditional profiles show that the droplet number densities within the large-scale clusters vary far less than the mean number densities, confirming the results of figure 3.10. The profiles also indicate that the conditional densities for the TNI are in fact higher than for the TTI, which is opposite to the case for the mean profiles. This is due to the nature of the entrainment mechanism. The droplets are entrained in droplet-laden, large-scale clusters which break up and disperse over time such that the

droplets become more uniformly distributed. The ambient turbulence of the TTI aids in this dispersal, while the quiescent conditions of the TNI allow the clusters to endure. We also note that the conditional profiles are not monotonic in y, and this fits with our description of the entrainment. The growing droplet mixing layer introduces droplets to previously droplet-free regions via the clusters described above. The clusters in the low-mean-density, "growth" region have shorter regional time histories than those in the central portion of the mixing layer, since the growth region has only clusters which have recently penetrated to their current position. These droplet clusters have had little time to break up and disperse, and so it is possible for the droplets and turbulence within them to retain a state more similar to the source region than to the "dispersed," or mixed region in between, where the large-scale clusters have had time to break up are less dense on average. In figure 3.11, we may then identify the growth regions by their increase in the cluster-conditioned droplet densities. These regions roughly correspond to where the unconditioned droplet mean number density $n/n_{max} \lesssim 10^{-2}$. Referring back to figure 3.10, we note that the $(n/n_{max}) \cdot g(r/\ell' \ll 1)$ values were similarly non-monotonic in y.

3.3.4 Droplet entrainment and velocity statistics

In this section we examine the droplet entrainment using their velocity data. In particular, we examine the role of the mean number density gradients and large-scale clustering on the mean droplet velocities and the moments of the velocity distributions.

Droplet mean velocities and transport

Mean droplet velocity ($-V_p$) profiles are shown in figure 3.12. Clearly, the mean velocities increase across the mixing layers for both the small and large droplet groups and all flow cases. In GGW we could not discern velocity differences between the $g+$ and $g-$ cases due to poorer resolution of the velocity data. Here, we discern the velocity differences between the small and large droplets; the difference is generally smaller than that predicted by the droplet group Stokes velocities ($\Delta S v_{\ell'} \equiv \Delta\tau_p g/v'_{rms} \approx 0.3$, table 3.2), consistent with the turbulence settling effects described in § 3.3.2. We note that in figure 3.12 there is a crossing of the large- and small-droplet velocity profiles for the TNI $g+$ case. The other flow case velocity profiles also show a tendency to converge (at large negative y), but they are not seen to cross. There are two mechanisms by which these trends may result; the first relates to gradient-driven transport and may result in crossing, and the second to the intermittent penetration of the large scales across the interfaces.

The crossing of mean velocity profiles is expected when the mean velocity is tied to gradients in the local number density field, as it is in Fickian mixing. If the droplet field shifts due to gravitational settling, so do the velocity profiles. In this scenario, a shift in abscissa for a given droplet group due to gravitational settling has an effect opposite to that of the particle settling velocity on the local mean velocity. This is perhaps best understood in the following way: If a particle $g0$ case has number density $n_0(y,t)$ and mean velocity profile $V_0(y,t)$, where t is the advection time from the initial condition ($t = 0$), then, to first order, the $g+$ case has $n_+(y,t) = n_0(y+Wt,t)$ and $V_+(y,t) = V_0(y+Wt,t)+W$, where W is the particle settling velocity. While the W term increases the mean velocity uniformly, the

downstream shift in abscissa (Wt) moves the gravity case down the V_0 curve for a local velocity reduction. Eventually, a crossover in the mean velocities due to differences in W for two differing particle groups is expected. This is quite clear for the TNI $g+$ case. Here, we see that the tails of the large and small droplet number density profiles (figure 3.8) are separated by $y/\ell' \sim 0.2$ near $y/\ell' = -0.5$. In figure 3.12, such a shift in abscissa corresponds to a velocity reduction for the TNI $g+$ large particles of $V_p/v' \sim 0.3$, which is similar to the change in the large versus small droplet group V_p difference between this location ($y/\ell' = -0.5$) and the homogeneous region ($y/\ell' \approx 1$).

Owing to the configuration of the wind tunnel, we were only able to measure the transverse velocity for the $g+$ and $g-$ cases. In order to further examine the degree to which the mean droplet transport is gradient-driven, the theoretical mean droplet velocities based on a purely Fickian mixing model are also plotted in figure 3.12 based on the $g0$, small droplet group number density profile fits (figure 3.8). For the TTI case this has the analytic form

$$V_p(x,y) \equiv -\frac{D_n}{n}\frac{\partial n}{\partial y} = -\sqrt{\frac{D_n U}{\pi x}} \cdot \frac{exp(-(y-y_o)^2/(4D_n(x/U)))}{1 + erf((y-y_o)/\sqrt{4D_n(x/U)})}. \tag{3.1}$$

The Fickian model velocities do not account for changes in V_p due to particle settling. The model profiles are however similar in shape to the measured profiles, although for the TTI the model values increase more slowly across the interface than do the measurements. The agreement is particularly good for the TNI. We note that the TTI cases have greater mean droplet velocities in general.

For the TTI, and the TNI $g-$ case, the velocity difference between the droplet groups narrows across the particle mixing layers, but the profiles do not cross.

The degree to which this is a result of the shifting effect described above is unclear, as there is a second mechanism for the convergence. Figure 3.13 shows the mean velocity of the droplets conditioned on and as a function of the distance, r, between adjacent droplets (based on interarrival times). This is shown at $y/\ell' = -1/4$, where figure 3.9 demonstrated high degrees of large-scale droplet clustering. It is clear that the droplets which travel fastest across the interfaces are also those which are most densely grouped (small r/ℓ'). The fast-moving, dense droplet clusters are swept unidirectionally by the large scales from the seeded region and thus have the greatest mean velocities. Since the flux, J, of particles with separation distance r goes as $J(r) \propto V_p(r) \cdot r^{-3}$ (since the volumetric number density goes as r^{-3}), it is clear from figure 3.13 that the droplet-laden bursts dominate the particle entrainment. We note that the mean velocity differences between the droplet groups and gravitational cases in figure 3.13 become negligible for small r/ℓ', as velocities for clustered droplets within intermittent bursts are determined by the fluid burst velocities and are less sensitive to the mean droplet number density gradients. Thus, as we traverse the particle mixing layers from positive to negative y, where there is progressively more large-scale clustering, we expect both the convergence of the velocity profiles and the departure from the Fickian model lines (figure 3.12).

Moments of the droplet velocity distributions

Figure 3.14 shows the droplet velocity r.m.s. profiles for the v component, normalized by v'_{rms}. We note that the profiles were qualitatively the same for the u component, and that when compared with the fluid velocity hot wire measurements, the particle r.m.s. velocities were greater by about 10 and 20% in

the homogeneous region for the u and v components, respectively, presumably reflecting the way the particles sample the fluid. Moving across the particle mixing layers, there is a decrease in the droplet velocity r.m.s. for even the TTI case, which has transversely homogeneous turbulence. In general, particles which sample a fluid velocity probability density function (pdf) should see a decrease in their velocity r.m.s. when there is a mean number density gradient. Here, however, the situation is complicated by the bursting.

In the entrainment region, there are both droplets which have crossed the interfaces well upstream of the test section and have had time to disperse and adjust to the local fluid velocity field, and still densely clustered droplets recently ejected in bursts from the seeded region. The velocities of such bursts are associated with those of the tail of the high-turbulence fluid velocity pdf (in the seeded side of the flows). It is expected then that the droplet velocity r.m.s. contribution from the variance of these burst velocities thus declines as one moves across the particle mixing layers to where only successively stronger bursts can penetrate, and droplets are observed to be increasingly clustered at the large scales. As expected, there is a greater reduction in the droplet velocity r.m.s. for the TNI than for the TTI, due to the sampling of the low-turbulence fluid velocity field, and possibly more invariant penetration of the fluid bursts into relatively quiescent rather than highly turbulent fluid.

The differences in the droplet velocity r.m.s. profiles between the droplet groups or gravitational cases are small. In general, however, we expect the droplet velocity statistics to be more reflective of the fluid velocity field where the droplets are least clustered at the large scales, where their mean number density is relatively high. For the TTI and the high-turbulence side of the TNI,

the velocity field has a higher r.m.s. than that we expect is associated with the bursting droplets. Here, the $g+$ droplets have higher velocity r.m.s. than do the $g-$ droplets, consistent with their greater number density which better reflects the fluid velocity field. For the TNI there is a switch near $y/\ell' \approx 0$. The fluid velocity field r.m.s. becomes very small through this region (figure 3.3), and we see that the TNI $g+$ droplet velocity r.m.s. becomes reduced as compared with the TNI $g-$ droplet cases. While the differences in the measurements presented in figure 3.14 (& 3.15) are small (although confirmed by the confidence intervals), the trends are remarkably consistent with the DNS results of an analogous mixing layer by Ireland and Collins (2012).

Figure 3.15 shows the (negative) droplet velocity skewness, such that we may refer to the velocity being skewed with (positive values) or against (negative values) the mean transport direction. In the homogeneous regions ($y/\ell' = 1$), the droplet velocity skewness is nearly zero for both the TTI and TNI, like for the fluid velocity fields. Proceeding into the mixing layers where there is little or no large-scale clustering ($0.5 < y/\ell' < 1$, figure 3.9), the skewnesses become weakly positive. For $y/\ell' < 0.5$, the droplet velocity skewness continues to grow positively for the TNI cases, while it decreases and becomes weakly negative for the TTI cases.

The moments of the droplet velocity pdfs indicate how the droplets sample the fluid velocity field. Although the TTI velocity field is unskewed, figure 3.13 clearly shows that the droplets in the bursting region heavily sample the high-velocity events that are in the positive tail of the fluid velocity pdf. As a result, the TTI particle velocity pdfs in the bursting region have elongated negative tails and negative skewnesses. For the TNI, the droplets sample a velocity

field which is largely positively skewed (figure 3.5) due to its large-scale intermittency, and the droplet velocity distributions reflect this skewness. Although the shape of the droplet number density profiles certainly has some effect on the droplet velocity statistics, the measurements are very consistent in light of the clustered entrainment. Those droplet groups and flow cases which show comparatively more large-scale clustering at a particular y/ℓ' location (see figure 3.9), also have more negative transverse droplet velocity (v_p) skewness. Where the mean number densities are higher, the v_p skewness is more positive and closer to the velocity field values (figure 3.5). We lastly note that the skewed pdfs also have super-Gaussian values of kurtosis, with values reaching ~ 4 at $y/\ell' = -0.5$ for the TNI g+ large droplets, and ~ 3.5 for the other cases.

3.3.5 Droplet accelerations

We have thus far documented the large-scale entrainment and clustering of water droplets in both the TTI and TNI. Given the results of GGW, this has helped explain the absence of evaporative effects without a full description of the humidity field and its correlation to the droplet field. While the only distinguishing factor between the air flows on either side of the TTI may be its vapor content, for the case of the TNI, the turbulence levels are also quite distinct. In this final section we look at the droplet accelerations, which, being indicative of the small scales of the turbulence, give us insight into the particle-fluid interactions in the entrainment zone.

Figure 3.16 shows a profile of the droplet acceleration r.m.s. in the TNI. The full distribution $g0$ data is shown, as the Lagrangian particle tracking system is

unable to discern particle sizes, and the particle size distribution is not a function of y in the $g0$ case (GGW). While the dashed line shows the variation of the Kolmogorov eddy acceleration, $a_\eta \equiv (\epsilon^3/\nu)^{1/4}$, based on the TNI mean dissipation profile (figure 3.3), the symbols show measurements of the droplet r.m.s. accelerations. The streamwise component is shown, although the measurements are not strongly sensitive to this choice. We take the r.m.s. values to be the proper scale of the droplet accelerations, as the mean accelerations are zero in the shearless interfaces. The large error bars are due to the pixel-limited spatial resolution of the particle tracking system.

Clearly, the droplet accelerations do not differ substantially across the TNI, despite the large step in the turbulence levels. This indicates that the turbulence within the bursts and large-scale droplet clusters is similar to that in the high-turbulence, droplet-laden side of the flows. This is like in the droplet-free, figure 3.1 image. Since the sub-Kolmogorov-sized droplets only feel the small scales of the turbulence, and these small scales do not differ within the fluid bursts which transport the bulk of the droplets, the particle-fluid interactions remain only weakly changed in even the TNI. Measurements in the gravitational cases at $y/\ell' = \pm 1/4$ also showed only small differences in the acceleration r.m.s., although these differences were also consistent with changes in the droplet size distributions due to gravity (see GGW). The acceleration measurements are thus consistent with the general results of the present study, that the intermittent entrainment mechanism preserves the droplet-ambient conditions that are present in the injection side of the flows.

3.4 Conclusions

We have studied the entrainment of inertial particles across two shearless interfaces. Water droplets injected into the turbulent side of the flows were entrained into a coflow that was in one case close to laminar (TNI) and in another having the same turbulence characteristics as the droplet carrier flow (TTI). The effects of gravity were isolated by turning the apparatus with respect to the gravitational field. The study followed from the earlier work of Gerashchenko et al. (2011), which focused mainly on the mean droplet statistics. Here, we have studied higher-order statistics as well as particle pair and Lagrangian acceleration data.

Our main findings are as follows. In homogeneous conditions, the polydispersed droplets (ranging in size from a few micrometers to approximately eighty micrometers, figure 3.6) were shown to exhibit both enhanced and reduced settling velocities (compared with their Stokes velocities in a quiescent flow), depending on their large-scale settling parameter, the ratio of the characteristic time of an eddy to the time for a particle traveling at its Stokes velocity to pass it (§ 3.3.2). While the small particles fell faster than their Stokes velocities in a quiescent flow due to their preference for the downward-sweeping sides of eddies, the large droplet settling velocities were reduced due to droplets loitering in upward-moving regions of the flow. This 'loitering' effect appears not to have been previously reported in wind tunnel experiments.

In the particle mixing layers of the TTI and TNI, the mean particle transport velocities increased across the entrainment region for all particle sizes and for gravity both aiding and inhibiting the mixing process ($g+$ and $g-$, figure 3.12).

Consistent with the turbulence settling effects, the differences in the mean velocities of the large and small droplets was smaller than predicted from their Stokes velocities. For the g+, TNI case, there was a crossing of the large and small droplet velocity profiles, with the small droplets traveling faster than the larger ones far into the entrainment region. This was attributed mainly to the shifting of the mean number density profiles relative to each other due to gravitational settling (§ 3.3.4). Convergence of the velocity profiles in this region was observed for the other cases. While the relative shifting of the number density profiles may be partially responsible for this convergence, conditional velocity statistics (figure 3.13) showed that the turbulent bursts which transport most droplets are insensitive to droplet size and gravitational case, and thus, that the convergence is expected by this intermittent entrainment mechanism. Still, a Fickian, mean-gradient mixing model was able to capture the form of the mean velocity profiles, particularly for the TNI case (figure 3.12). The droplet r.m.s. velocities decreased across the entrainment region for both the TNI and TTI, although this was less pronounced for the latter (figure 3.14). The ability of a burst of droplets to penetrate deeply into the entrainment region depends on its energy, and thus the droplet velocity probability distributions narrow across the particle mixing layers. The skewness of the droplet velocity distributions was also documented (figure 3.15), showing that the droplets in regions with more pronounced large-scale clustering also exhibit more negative (counter-entrainment) velocity skewness.

The droplet r.d.f.s were used to show the droplet spatial organization throughout the flows. Radial distribution functions have traditionally been used to show small-scale (inertial) clustering in isotropic particle fields, where inertial particles are centrifuged out of the regions of high vorticity into regions

of high strain (Shaw et al. (1998)). Here, we have shown the large-scale clustering of droplets due to the intermittent entrainment process. This clustering was evident in the velocity fields of not only the inhomogeneous TNI, but the homogeneous TTI as well (figure 3.9). The large-scale clustering presented in increased magnitudes in the r.d.f.s for $r/\ell' < 1$ and decreased magnitudes for order one r/ℓ', representing the droplet-free gaps between large-scale clusters.

At the small scales, there was little change in the nature of the r.d.f.s as compared with in the homogeneous, droplet-laden side of the flows. Thus, the bursting associated with the entrainment appears not to affect the small-scale clustering. Lagrangian measurements of the droplet accelerations (figure 3.16) also showed little change in this small-scale quantity for even the strongly inhomogeneous TNI velocity field. The ability of the entrainment process to transport large, macroscale bursts without affecting the small-scale properties is consistent with the earlier finding of GGW, that the droplet size distribution does not change across the interfaces for the $g0$ cases, in which gravity does not play a role (GGW, figure 5a). The lack of a change in the particle size distribution for the $g0$ cases indicates that the large-scale bursts transport the droplet-laden fluid in bulk. Evaporative effects thus appear to be negligible in our flows. Conditional statistics of the mean droplet number densities (figure 3.11) showed that, as may be expected, the large-scale clusters were more dense in the TNI than for the TTI, where the background turbulence is more effective in dispersing the particles. Both the conditional statistics and the r.d.f.s provided information on the time histories of the large-scale droplet clusters. In particular, the droplet-laden bursts which have penetrated farthest across the growing mixing layers may have properties more similar to their source region than to the intermediate, center portion of the mixing layer (figure 3.11 and related discussion).

In this central region, droplet clusters transported earlier by smaller turbulence scales will have had more time to break up and disperse, and their droplets will be more uniformly distributed and less dense as a result (§ 3.3.3).

The experiments help in our understanding of cloud boundaries, whether they be at the floors, sides or ceilings of clouds. As noted in GGW, the experimental parameters (with the exception of the low Reynolds numbers) are in the range observed in typical cumulous clouds (Siebert et al., 2010). The $S\,v_\ell$ range of the experiment ($0.03 - 0.35$) and clouds ($10^{-3} - 10^{0}$) is noteworthy, as some micrometeorological models which neglect the role of turbulence in droplet coalescence and cloud evolution rely on Stokes velocity differences between large and small droplets (Shaw, 2003), which may actually be diminished due to turbulence. The results relate more broadly to particle entrainment in environmental flows, like the atmospheric boundary layer, as well as to industrial and energy-related applications concerned with the mixing or dispersion of heavy particles.

We thank Peter Ireland and Lance Collins for their discussion, and refer the reader to Ireland and Collins (2012) for a comparison of the results with DNS studies. We also thank Todd Cowen for the use of the Defrees Hydraulics Lab wind tunnel. This work was supported by the US National Science Foundation.

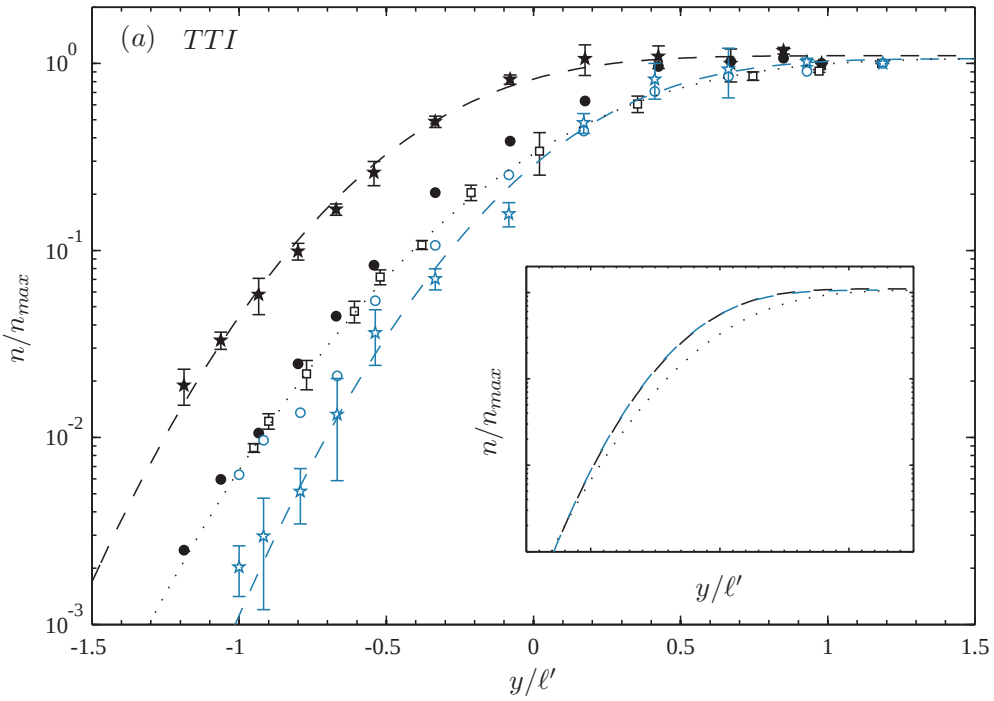

Figure 3.8: Droplet number density profiles for the TTI (a) and TNI (b) (next page). Circles and stars denote the small and large droplet groups, respectively, for both the $g+$ (filled symbols) and $g-$ (open symbols) cases. Open squares denote the $g0$ small droplet case. Lines are error function fits for the TTI and finite-element method (FEM) fits for the TNI (see the text); the insets show the main figure fits shifted to converge asymptotically.

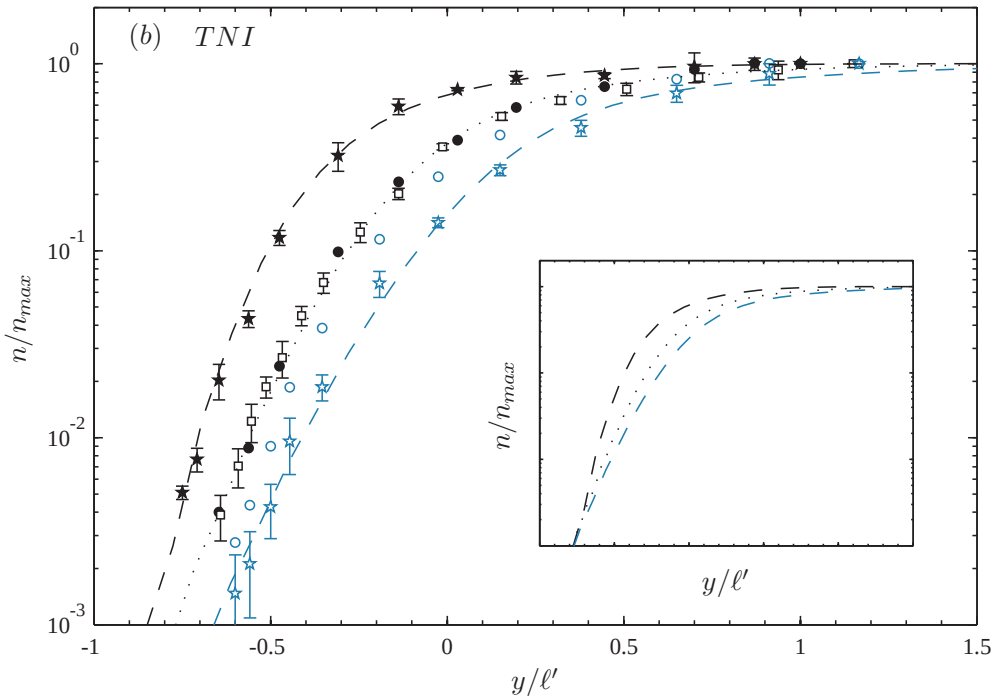

Figure 3.8 (continued)

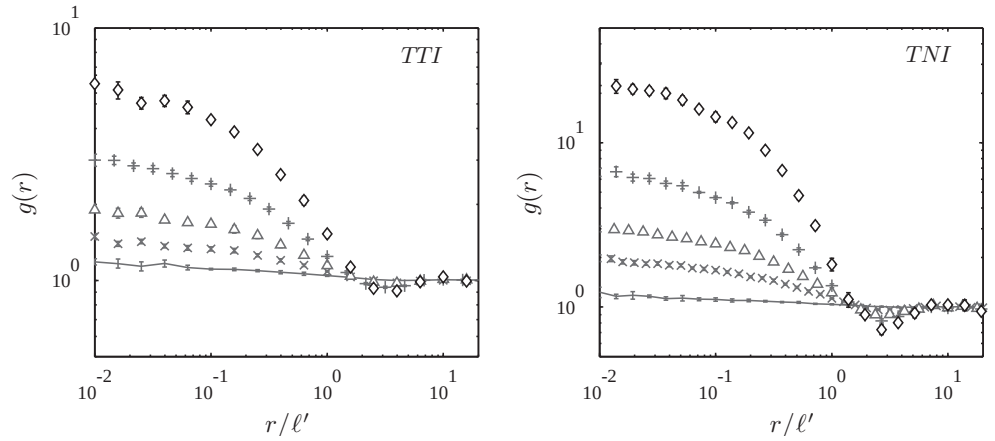

Figure 3.9: Radial distribution function, $g(r)$, for the $g+$ case with small droplets for the TTI (left) and TNI (right). The measurement locations are at $y/\ell' = 1,\ 1/4,\ 0,\ -1/4,\ \&\ -1/2$ for the TTI and $y/\ell' = 5/6,\ 0,\ -1/6,\ -1/3$ and $-1/2$ for the TNI, denoted by the solid line, $\times$, $\triangle$, $+$ and $\diamond$, respectively.

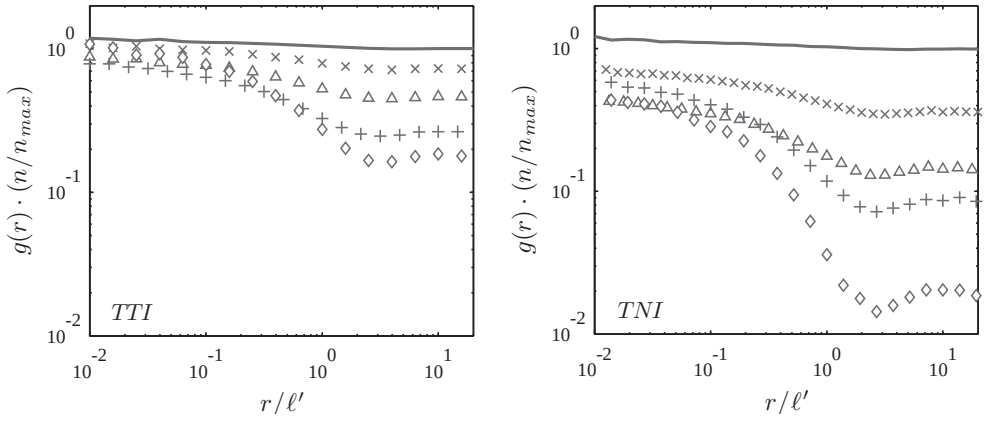

Figure 3.10: Product $g(r) \cdot (n/n_{max})$ for the $g+$ case small droplets for the TTI (left) and TNI (right). The measurement locations are at $y/\ell' = 1,\ 1/4,\ 0,\ -1/4,$ and $-1/2$ for the TTI and $y/\ell' = 5/6,\ 0,\ -1/6,\ -1/3,$ and $-1/2$ for the TNI, denoted by the solid line, $\times$, $\triangle$, $+$ and $\diamond$, respectively.

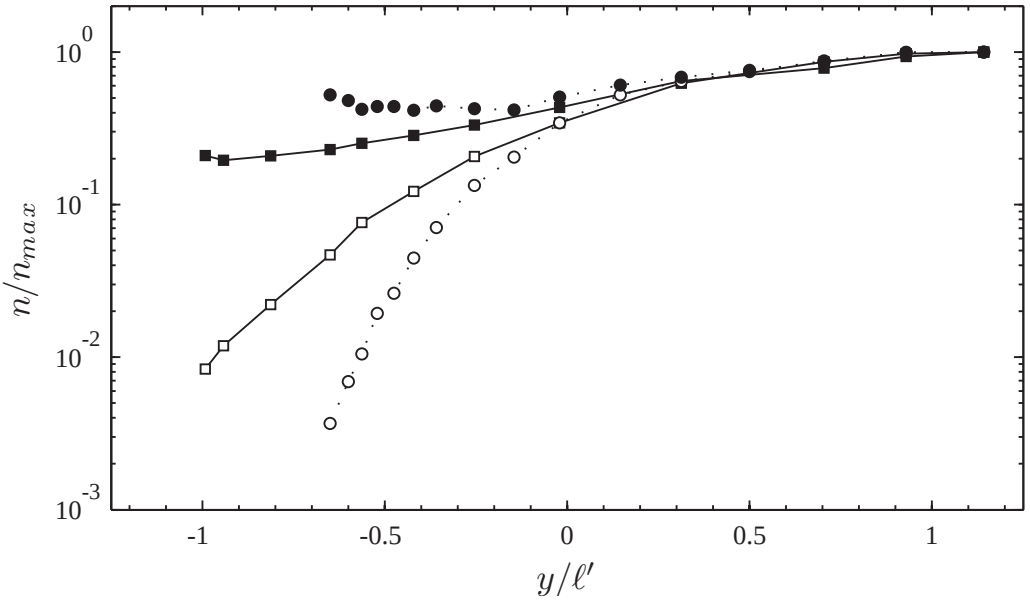

Figure 3.11: Conditional (filled symbols) and regular (open symbols) mean droplet number density profiles for the TTI (squares) and TNI (circles) $g0$ cases. The unconditioned profiles are the same as in figure 3.8.

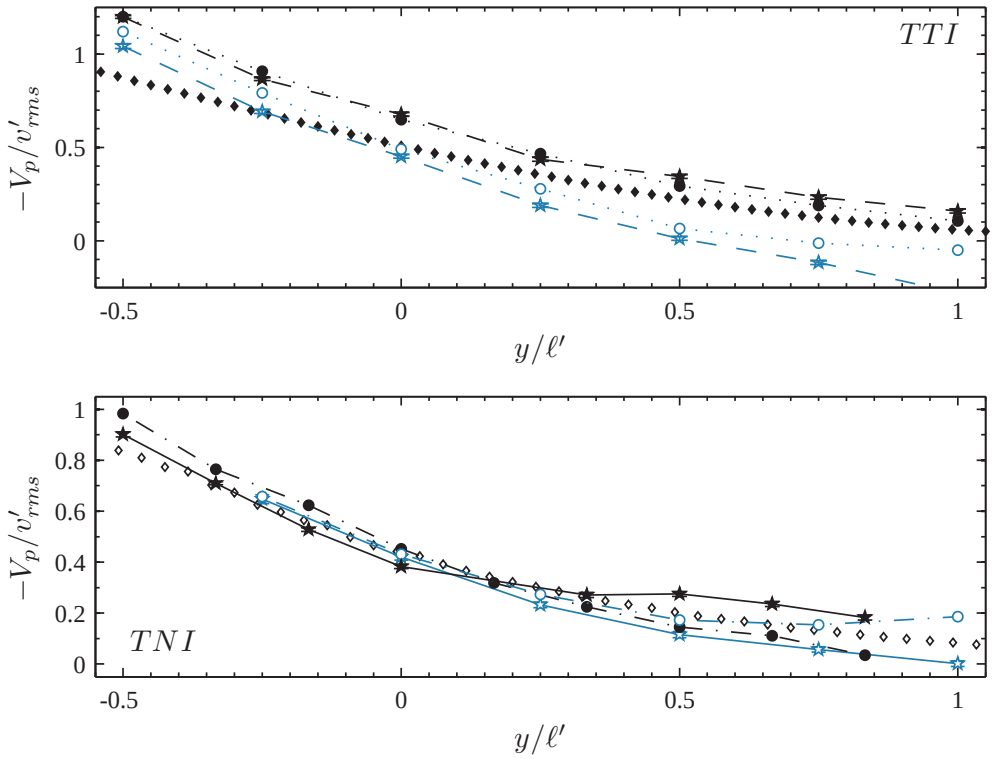

Figure 3.12: TTI (top) and TNI (bottom) mean transverse droplet velocity profiles across the mixing layers. Circles and stars denote small and large droplet groups, respectively, for both the $g+$ (filled symbols) and $g-$ (open symbols) cases. The small and large droplet groups are further distinguished by dotted and dashed lines for the TTI, and mixed-dashed and solid lines for the TNI. Filled and open diamonds, for the TTI and TNI, respectively, show the expected mean velocity based on a Fickian mixing model and the $g0$ number density profile fits of figure 3.8. The error bars shown here and for figures 3.14-3.15 are 95% confidence intervals, and in some cases are similar in size to the data point symbols. They are shown only for the (less numerous) large droplet data to avoid clutter.

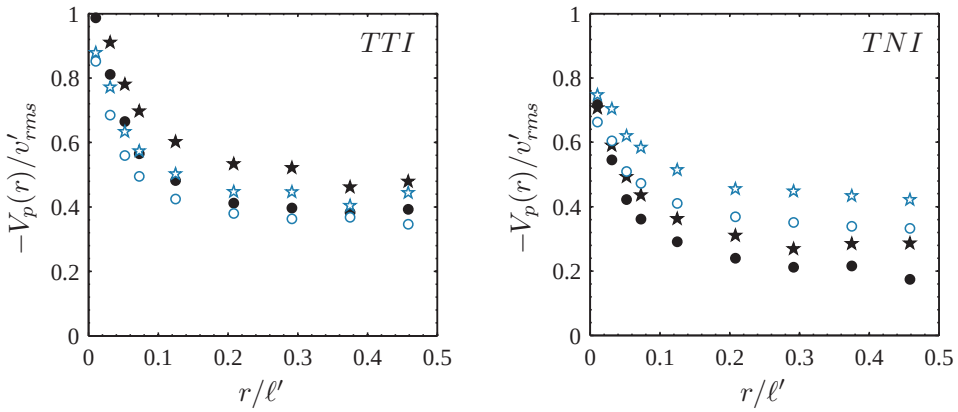

Figure 3.13: TTI (left) and TNI (right) mean droplet velocity as a function of local droplet separation distance, r, for the $g+$ (filled symbols) and $g-$ (open symbols) cases. Circles and stars denote the small and large droplet groups at $y/\ell' = -1/4$.

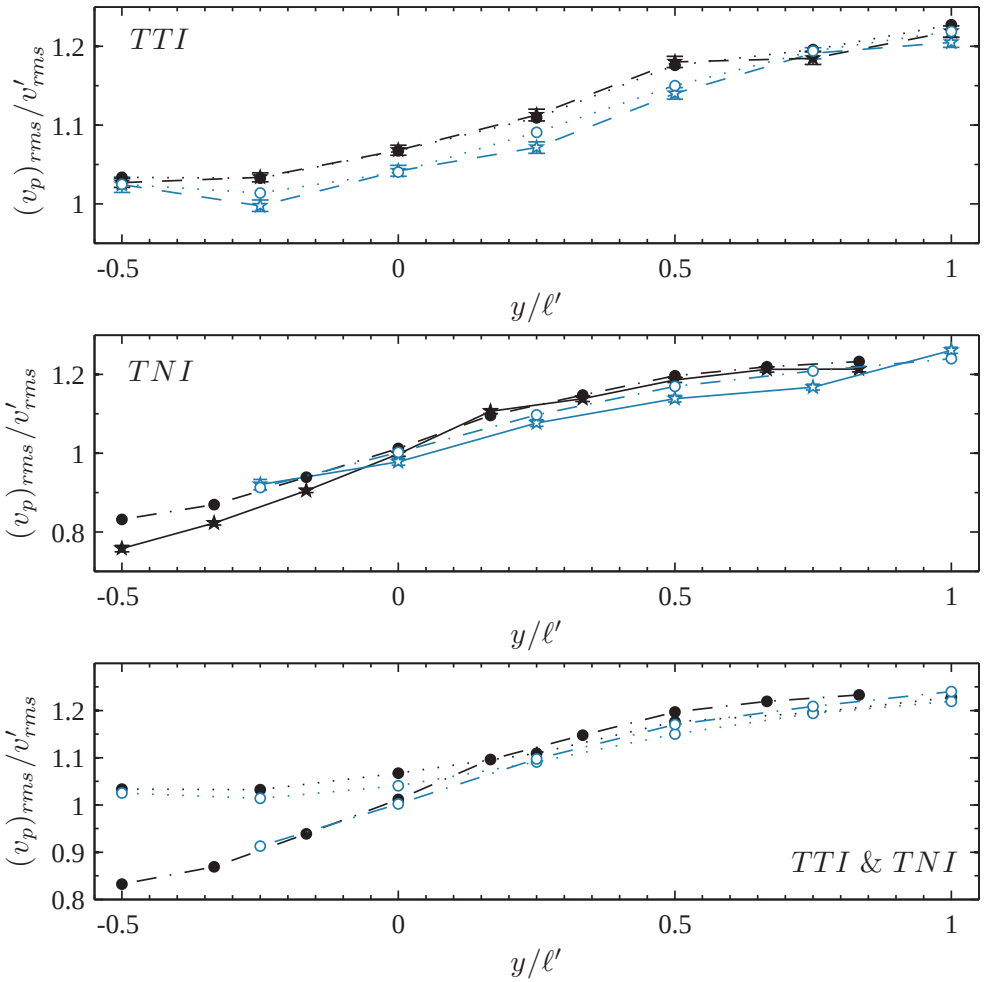

Figure 3.14: TTI (top plot) and TNI (center plot) droplet $(v_p)_{rms}$ profiles across the mixing layers. Circles and stars denote the small and large droplet groups, respectively, for both the $g+$ (filled symbols) and $g-$ (open symbols) cases. The small and large droplet groups are further distinguished by dotted and dashed lines for the TTI, and mixed-dashed and solid lines for the TNI. The small droplet TTI and TNI cases are also shown together for comparison (bottom plot).

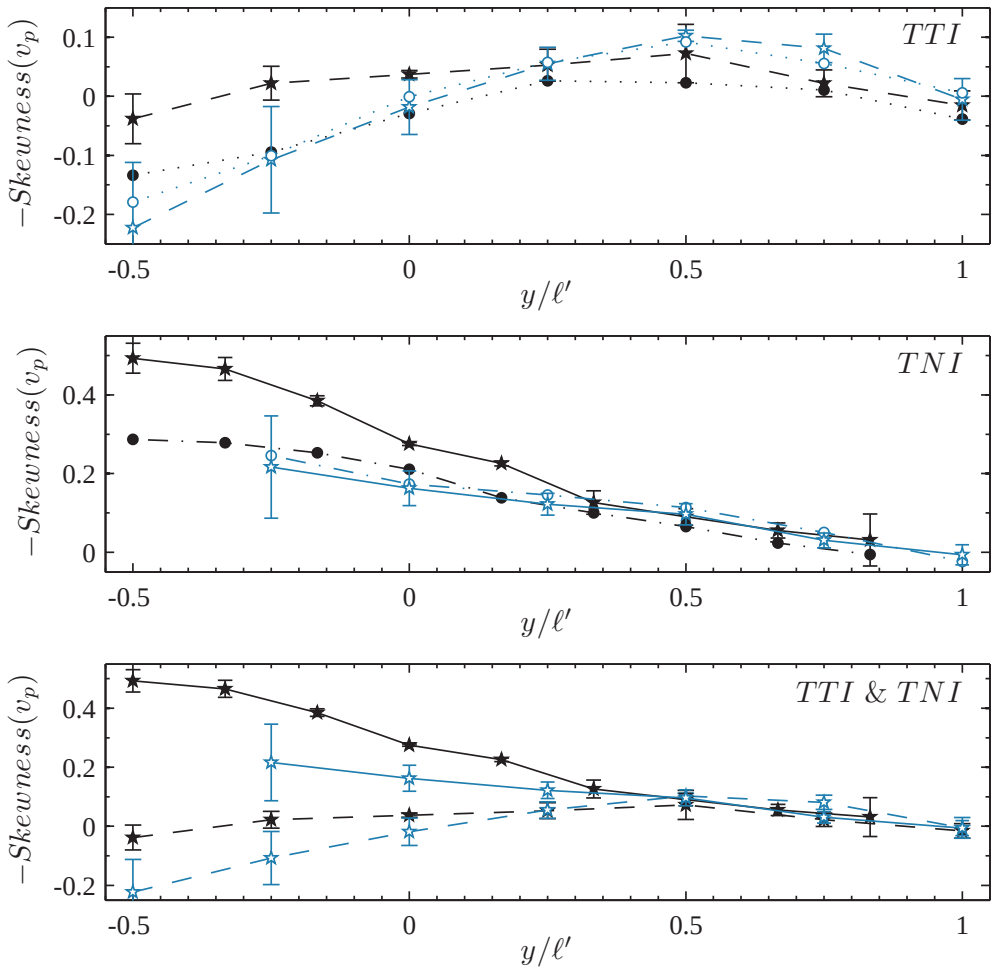

Figure 3.15: TTI (top plot) and TNI (center plot) droplet velocity skewness profiles across the mixing layers. Circles and stars denote the small and large droplet groups, respectively, for both the $g+$ (filled symbols) and $g-$ (open symbols) cases. The small and large droplet groups are further distinguished by dotted and dashed lines for the TTI, and mixed-dashed and solid lines for the TNI. The large droplet TTI and TNI cases are also shown together for comparison (bottom plot).

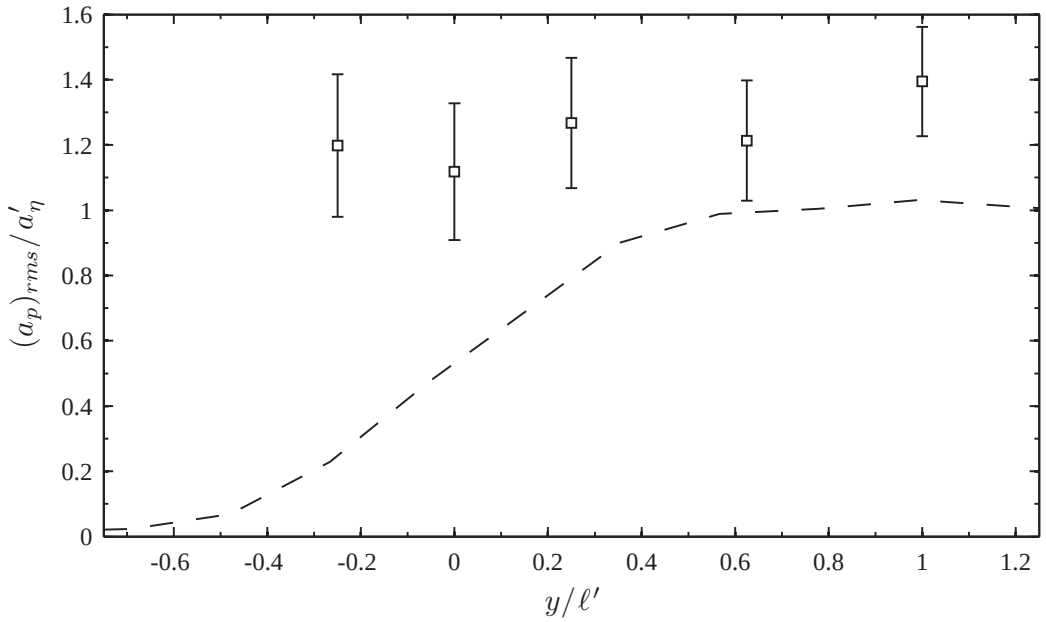

Figure 3.16: Profile of the droplet acceleration r.m.s. (symbols) for the full droplet size distribution ($g0$ case) in the TNI. The streamwise acceleration data is shown. The dashed line shows the variation of the Kolmogorov acceleration, $a_\eta \equiv (\epsilon^3/\nu)^{1/4}$, as determined from the mean dissipation profile for the TNI (figure 3.3).

CHAPTER 4

SETTLING REGIMES OF INERTIAL PARTICLES IN ISOTROPIC TURBULENCE[1]

We investigate the settling speed, velocity r.m.s. and velocity r.m.s. anisotropy of an unprecedented range of inertial particles in isotropic turbulence with gravity using direct numerical simulations (with and without nonlinear drag) and experiments with water droplets in air turbulence from 32 loudspeaker jets. We identify five important parameters related to particle buoyancy and response time ($\propto g$, τ_p, $\tau_p g$, $\tau_p^2 g$ and $\tau_p^3 g^2$) and many regimes and particle classes for which any one may be dominant in determining inertial particle response to turbulence. We isolate the three mechanisms of turbulence settling modification, including for the first time the loitering effect described by Nielsen (1993). We show horizontal fluctuations to be relevant to settling enhancement and vertical fluctuations to be to both the loitering and nonlinear drag settling reduction mechanisms.

4.1 Introduction

The behavior of heavy, inertial particles in turbulent flows is of broad interest for both environmental and engineering problems. Applications include sediment transport in surface water flows, water droplets or aerosols in atmospheric turbulence, volcanic eruptions, dust storms, powder snow avalanches, fluidized beds and soot particle dispersion.

Inertial particles are known to avoid vortical regions in favor of regions of

[1]Intened for publication in *J. Fluid Mech.* (2013)

strain (Squires and Eaton, 1991; Wang and Maxey, 1993). The subsequent small-scale clustering of sub-Kolmogorov-sized particles, which is usually attributed to centrifugal forces in vortical structures, affects many natural phenomena, such as the rates of cloud droplet collision, coalescence and growth (Shaw, 2003). Much work has also detailed the mean settling speeds of heavy particles through turbulence. While weakly inertial particles may become indefinitely trapped in a forced vortex (Tooby et al., 1977), it has instead been observed that the transient eddies of turbulence result in increased settling speeds for particles below some critical size, as they show preference for the downward-sweeping sides of eddies while circumventing vortex cores (Wang and Maxey, 1993; Dávila and Hunt, 2001; Aliseda et al., 2002; Hill, 2005). These biased paths through the fluid are sometimes called 'fast-tracks' (Nielsen, 1993). When a particle is unable to side-step eddies due to its weight, it instead equally bisects upward- and downward-moving flow, spending more time crossing the former and being slowed on average. Nielsen (1993) described this as 'loitering'. Particles with nonlinear drag effects may also be slowed, given the higher slip velocities, particle Reynolds numbers and drag of crossing upward-moving flow (Mei, 1994; Yang and Shy, 2003). The turbulent settling speeds of particles are therefore determined by the balance of the fast-tracking, loitering and nonlinear drag effects, and the descriptions emphasize the importance of vertical fluctuations as compared to the lateral motions necessary to circumvent upward-moving flow.

The fast-tracking effect is maximized for particles which couple best to the smallest eddies (Wang and Maxey, 1993); smaller particles behave like tracers, and the coupling of larger particles to larger eddies is disrupted by the smaller scales. Fast-tracking fails to enhance settling speeds for particles unable to cou-

ple to even the largest vortices of the flow (Nielsen, 1993; Yang and Lei, 1998; Dávila and Hunt, 2001; Yang and Shy, 2005; Ghosh et al., 2005; Kawanisi and Shiozaki, 2008). Any reduction in settling speed also reaches some maximum before becoming negligible in the limit of infinite particle inertia.

The loitering mechanism can only be distinguished in the linear-drag regime, where several studies show only enhanced settling velocities, indicating that fast-tracking dominates (Wang and Maxey, 1993; Yang and Lei, 1998; Aliseda et al., 2002; Yang and Shy, 2003; Ireland and Collins, 2012). This contrasts models and some experiments (Nielsen, 1993; Dávila and Hunt, 2001; Kawanisi and Shiozaki, 2008). The present work is motivated by the bifurcated settling effects like in Nielsen (1993) observed in the entrainment experiments of Good et al. (2012), but not in the matched DNS of Ireland and Collins (2012). (We note the enhancement regime in Good et al. (2012) is exaggerated for small droplets by non-negligible background flows).

It is the objective of this paper to use new numerical and experimental results to identify the mechanisms by which turbulence modifies particle settling speeds, to quantify the regimes of particle settling behavior and to determine what non-dimensional parameters are the key to each. The two-parameter space of particle weight and inertia are resolved for isotropic turbulence in unprecedented detail using a wide variety of particle fields in DNS. Key results are validated experimentally. We proceed with the methodology section, defining the nomenclature and definitions of the study and detailing the DNS and experiments. The results (§4.3) and subsequent conclusions (§4.4) will then be discussed.

4.2 Methodology

4.2.1 Nomenclature and conditions

We are concerned with the isotropic turbulent flow of a fluid with density ρ and kinematic viscosity ν. The velocity field, $\vec{u}$, has zero mean, turbulent kinetic energy $k \equiv \frac{1}{2}\langle\vec{u}^2\rangle$, r.m.s. velocity $u' \equiv \sqrt{2k/3}$, and energy dissipation rate $\epsilon \equiv \nu\langle\partial_j u_i + \partial_i u_j\rangle^2$.

The turbulence has a spectrum of eddy scales and we may generally refer to any given one as having size r and corresponding time, velocity and acceleration scales τ_r, $u_r = r/\tau_r$ and $a_r = u_r/\tau_r$, respectively. The large eddies are represented by the scales $u_\ell \equiv u'$ and $r \equiv \ell$, with ℓ being the integral scale. The Kolmogorov microscales represent the smallest eddies with r and τ_r being $\eta \equiv (\nu^3/\epsilon)^{1/4}$ and $\tau_\eta \equiv (\nu/\epsilon)^{1/2}$, respectively. The turbulence has the Taylor-scale Reynolds number $R_\lambda \equiv \sqrt{\frac{20}{3}\frac{k^2}{\nu\epsilon}}$ and acceleration r.m.s. $a' = a'_o a_\eta$, where order one constant a'_o depends on R_λ (Sawford et al., 2003).

The flow contains spherical (*inertial*) particles of density ρ_p ($\gg \rho$), diameter $d < \eta$, response time $\tau_p \equiv d^2(\rho_p/\rho - 1)/18\nu$, and velocity $\vec{u}_p$. The particle drag coefficient is C_D, such that the still fluid settling velocity is $W_o \equiv \tau_p g/C_D$, with $g \approx g(1-\rho/\rho_p)$ being the gravitational acceleration in the *vertical* direction, about which the system is axisymmetric. For linear (Stokes) drag, $C_D = 1$ and W_o is the Stokes velocity. We otherwise use the nonlinear drag model $C_D = 1 + 0.15 \cdot R_p^{0.687}$ (Clift et al., 1978; Mei, 1994; Wang and Maxey, 1993), where the particle Reynolds number is $R_p \equiv d \cdot |\vec{u} - \vec{u}_p|/\nu$. We set $R_p = W_o d/\nu$ to determine W_o. The particle velocity field has turbulent settling velocity W, vertical and horizontal

r.m.s. velocities w'_p and v'_p, and $u'_p \equiv \sqrt{(w'^2_p + 2v'^2_p)/3)}$.

Two particle parameters are necessary to describe inertial and gravitational effects. These may be $St \equiv \tau_p/\tau_r$ and $Sv = \tau_p g/u_r$, where r is a chosen turbulence scale for normalization. From St and Sv we may express other parameters with possible physical significance, including a flow Froude number, $Fr \equiv g/a_r = Sv/St$, and the particle-transit Stokes and Froude numbers $\mathring{S}t \equiv \tau_p/(r/\tau_p g) = SvSt$ and $\mathring{F}r \equiv \tau_p^2 g/(ru_r/\tau_p g) = Sv^2 St$, which compare particle response time and stopping distance to particle transit time and typical path length around an eddy (Dávila and Hunt, 2001; Ghosh et al., 2005). Subscripts shall be used to specify $r = \eta$ or $r = \ell$. We lastly have $Fr_{a'} \equiv g/a' = Fr_\eta/a'_o$.

We restrict ourselves to the physics of one-way coupling between the flow field and single particles. Physically, this requires the particles be sufficiently dilute so as to not interact or modify the flow field by their collective drag. It also requires they be physically smaller than the smallest structures of the flow, of size η, and even in the conditions of nonlinear drag, that non-Stokesian flows around the particles are insufficient to affect the turbulence. By satisfying these conditions we study the effect of an independent turbulent flow on the single-point velocity statistics of inertial particles.

4.2.2 Direct Numerical Simulations

For the DNS, we simulate particle-laden flow in isotropic (box) turbulence using a pseudospectral code to solve the three-dimensional, incompressible Navier-Stokes equations in a periodic cube of dimension $\mathcal{L}$ (Ireland et al., 2013). The computing resources of the Max Planck Institute for Dynamics and Self-

Organization are used. The details of the three simulations are shown in table 4.1. We simulate one-way coupling between the flow and particle fields, with particle motion evolving by the Maxey-Riley equation, $\partial_t \vec{u}_p = (\vec{u} - \vec{u}_p)/(\tau_p/C_D) - \vec{g}$. 513 independent particle classes are simulated simultaneously, each denoted in figure 4.1, with the $g = 0$ groups omitted in log space. Their Stokes numbers are set by changing τ_p, while their settling parameters are independently set by changing g as well. In this way multiple Froude numbers are investigated at fixed Reynolds numbers, allowing us to discern their effects. Two particle fields are simulated for every particle class, one with the linear Stokes drag and one with the nonlinear drag model. For the nonlinear drag case, d is defined assuming the particles are water droplets in air ($\rho_p/\rho = 877$).

Simulations S1, S2 and S3 increase in R_λ in that order. Statistical stationarity of the fluid field is achieved through a deterministic large-scale forcing scheme (Witkowska et al., 1997). The particle fields reach stationarity after 5 large eddy times (τ_ℓ) and statistics are then averaged over an additional 10. Fast-falling particles could sense the periodicity of the box by recrossing it within one τ_ℓ (e.g., Woittiez et al., 2009). S2 and S3 have $\mathcal{L}/\ell \approx 4.5$, such that this is feasible for $S v_\ell > 5$. To test the effect of the finite domain size, S1 has the same small-scale resolution and ϵ as S2, but with $\mathcal{L}/\ell \approx 8$, such that the criterion is $S v_\ell > 13$. This difference yielded no observable effect on the results, however, and we thus observe no sensitivity to domain periodicity. S2 and S3 have similar large-scale parameters u' and ℓ and also small-scale resolution, allowing us to safely isolate R_λ effects on particle statistics. A fourth, 'forced-loitering' simulation has the same parameters as S2, but with particles confined to vertical paths, experiencing only linear Stokes drag forces in the vertical direction.

4.2.3 Experiment[2]

For the experiment, air turbulence is generated at the center of a one-meter diameter ball via thirty-two randomly driven loudspeaker jets mounted through its surface (figure 4.2). It is an acrylic version of the Chang et al. (2012) device, with the jet axes normal to the faces of a truncated icosahedron (soccer ball). The jets are focused by truncated cones and a homogeneous region of shearless, isotropic turbulence of about 10 cm in size is thus generated at the center of the ball, where all measurements are taken.

Water droplets are seeded at the top of the ball by an ultrasonic nozzle (Sono-Tek, Inc.). A syringe pump continuously wets the nozzle's conical tip, which vibrates piezeoelectrically, forming droplets by capillary wave instabilities, which thus enter the apparatus with negligible added momentum. The droplets are measured in two dimensions by high speed camera ($\geq$ 4000 Hz) shadow-imaging. The optics are the same as in Bewley et al. (2013) (3.2 microns/pixel resolution, 1.6^2 mm^2 window), but with increased depth of field for better data rates. Droplet size is determined by the major axis of the smallest ellipse which contains a droplet image; the droplet surface mean diameter (based on d^2, like τ_p) is ~75 microns, with 90% of the droplets in the 25 – 150 micron range. Droplets are measured over multiple frames and velocities are determined using the particle-tracking algorithm of Kelley and Ouellette (2011); only the median diameter and velocity measurement of each tracked particle is used. The turbulence mean and u' velocities are extrapolated from those of the smallest droplets; ϵ is then calculated from the Bewley et al. (2013) measure-

[2] Additional details of the experiments and data analysis are provided for the thesis in Appendix A

ments in the same apparatus. The particle volume fraction is about 10^{-6} and the energy added to the flow by the particles' collective drag is about 1% of ϵ, sufficiently small as to not modify the turbulence (Elghobashi and Truesdell, 1993; Sundaram and Collins, 1999; Bosse and Kleiser, 2006).

The experiment is similar in principle to that of Yang and Shy (2005). All droplets fall a sufficient distance to reach W_o under quiescent conditions, but their time in the isotropic region at the center is limited by their speed. The majority of the droplets cross order 10^1 to 10^2 times their stopping distance within the isotropic region. We exclude droplets with $d > 150$ microns as misrepresentative, as they are measured before crossing at least their stopping distance within the ~5 cm radius of the isotropic region.

We show experimental results from the three flows described in table 4.1 with the ranges of particles shown in figure 4.1. The error bars shown later account for the particle size distribution, and are 95% confidence intervals. In contrast to the DNS, we are unable to change gravity, and so different Froude numbers (Fr) are achieved by adjusting R_λ. The DNS results let us however isolate R_λ effects over an even much larger range.

4.3 Results

4.3.1 Settling modification

The DNS yield detailed contour plots of the normalized settling velocity difference, $(W - W_o)/u'$. They are shown as functions of St_η and Sv_η in figure 4.3,

	R_λ	$Fr_{a'}$	a'_o	u'/u_η	ℓ/η	u'	ϵ	η
S1	105	0-10^3	1.60	5.19	68.1	0.640	0.277	6.73E-3
S2	138	0-10^3	1.69	7.44	105	0.915	0.275	13.0E-3
S3	227	0-10^3	1.84	7.65	206	0.915	0.246	6.94E-3
E1	150	2.0(2)	1.70(6)	6.2(2)	97(12)	0.260(5)	0.20(3)	360E-6
E2	160	1.1	1.72(5)	6.4(2)	106(13)	0.330(5)	0.46(5)	290E-6
E3	176(9)	0.44(2)	1.75(5)	6.7(2)	122(12)	0.47	1.6	220E-6

Table 4.1: Properties of simulations (S1, S2 & S3) and experiments (E1, E2 & E3). Dimensional values have standard units for the experiments; the DNS have arbitrary units and 256^3 (S2) or 512^3 (S1 & S3) grid points.

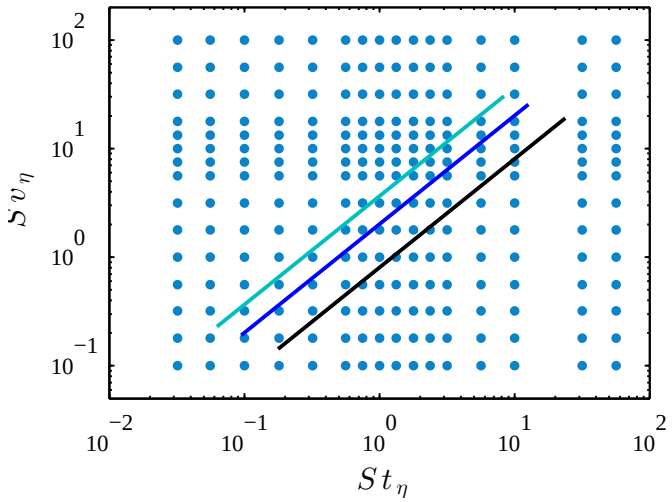

Figure 4.1: Particle classes in St-Sv space, points (DNS) and light (E1) and dark (E2) blue and black (E3) lines for the experiments.

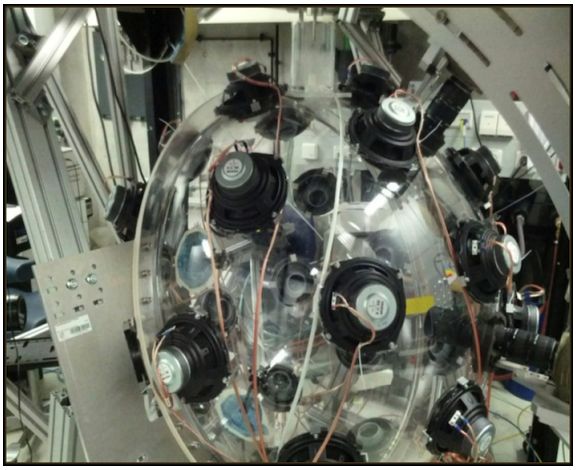

Figure 4.2: 'Soccer ball' apparatus with 32 loudspeaker jets, ultrasonic nozzle (top) and high-speed camera (right).

with lines showing critical values of the other particle parameters. The various regions of interest in the plots are lettered for reference and comparison to other figures.

The settling velocity enhancement is maximum in region m and approximately constant for our R_λ range at $0.18u'$, though Yang and Lei (1998) showed the value to increase slightly from $R_\lambda = 22.6$ to 153. The figure 4.3a-d contours are elliptical in log-log space, but become roughly parallel to lines of constant $\mathring{S}t = SvSt$, $Fr = Sv/St$ and Sv in regions n, o and p, respectively, such that $(W - W_o)/u'$ varies dominantly with one parameter in these regions. The parameter is the transit Stokes number $\mathring{S}t_\eta = \tau_p/(\eta/W_o)$ in region n, where $Fr_\eta > 1$ and $(W - W_o)/u'$ is independent of apparently saturated Froude effects, with the result that the timescale η/W_o dictates particle inertial response, not τ_η. In region o, the opposite is true, with $St_\eta > 1$ and $(W - W_o)/u'$ being a dominantly a function of $Fr_\eta < 1$ (independent of particle size). Inertial effects should have their maximum for $St_\eta \sim 1$ particles, and $(W - W_o)/u'$ is here instead sensitive to changes in Sv, which is particularly clear for $Sv_\ell > 1$ and contours in region p.

Comparing plots 4.3c-d shows the elliptical contours of the fast-tracking regime ($W > W_o$) to be the same, indicating that nonlinear drag effects are weak for the particle classes there.

Fast-tracking is ineffective for sufficiently heavy particles. For the Froude numbers with particle classes having strong fast-tracking effects, there is a transition at q and for $\mathring{F}r_\ell > 1$, such that $W \to W_o$ for the linear drag case and $W \to W < W_o$ with nonlinear drag. The contours here are parallel to $\mathring{F}r$, showing it to be the critical parameter. This dependence is expected, as there are no eddies large enough to accelerate these particles over their stopping distance (Dávila and Hunt, 2001; Ghosh et al., 2005). With nonlinear drag, the highest reductions of $\sim 0.2u'$ are seen in region H ($\mathring{F}r_\ell > 1 > Fr_\eta$). Reduced settling speeds extend somewhat beyond region H, with contours parallel to its Fr_η and $\mathring{F}r_\ell$ bounds, thus the key parameters for settling reductions by nonlinear drag.

The figure 4.3a-c results match for small values of St_η and Sv_η and the large-scale dependencies compare as well; the Sv_ℓ and $\mathring{F}r_\ell$ lines simply move in $St_\eta - Sv_\eta$ space with growing R_λ. The various described regions in the plots thus simply 'stretch' with growing scale separation, as they maintain both their small- and large-scale bounds, while being qualitatively the same, despite R_λ differences.

From figure 4.3d it is clear that loitering effects do not coincide with nonlinear drag effects, as there would be reduced settling velocities where fast-tracking is absent. It cannot however be distinguished whether loitering effects are unobserved due to fast-tracking events in regions *m*-*p*. The ultimate picture of loitering is when particles respond fully to the vertical fluctuations of the flow, but cannot move laterally to fast-track around eddies (Nielsen, 1993).

Figure 4.3e shows the same simulation as 4.3d, but where particles are confined to vertical paths, thus preventing fast-tracking. Real loitering effects could not exceed this model's, which reach $W - W_o = -0.4u'$. The reduction is a function of Sv for $St_\eta < 1$ and peaks at $Sv_\ell \approx 1$, matching Kawanisi and Shiozaki (2008). The turbulent fluctuations have a negligible effect on W for $Sv_\ell \equiv W_o/u' \gg 1$ and are too short-lived for $Sv_\ell \ll 1$ particles to achieve the frozen-flow picture of loitering. There is no loitering response for $St_\eta > 30$ or $\mathring{F}r_\ell > 1$. It is clear from the settling enhancements in figure 4.3d that fast-tracking events are prevalent in place of loitering ones in real turbulence. It could however be the case that the $(W - W_o)/u'$ decrease with Sv_ℓ in region p (figure 4.3e) corresponds to a relative increase in the number of loitering events.

Figure 4.3f shows the experimental data as well. The magnitude of the settling enhancements agrees with the DNS, although we cannot say how it varies with Fr, as each experiment has an abscissa error of about $0.05u'$ due to mean flow uncertainty. There is quantitative disagreement in the magnitude of settling reductions between DNS and experiment. The DNS show reductions of up to $15 - 20\%$ of u', but they appear to be greater for the experiment, although the minimum is not captured in the studied particle range. The experimental data does however begin to inflect and does reach a minimum of $W/W_o \approx 80\%$ (not plotted), in agreement with Dávila and Hunt (2001); Kawanisi and Shiozaki (2008). We expect a return to the Stokes velocity in the limit $\tau_p \to \infty$, like in Kawanisi and Shiozaki (2008). The S2 data collapse on both ends, as its R_λ is fixed, unlike for the experimental data, which diverge at the small scales. The experiment confirms that fast-tracking is ineffective for $\mathring{F}r_\ell > 1$. The earlier transition to $W < W_o$, and great reductions, may indicate nonlinear drag effects to be stronger in the experiment; the decade differences in the transition point does

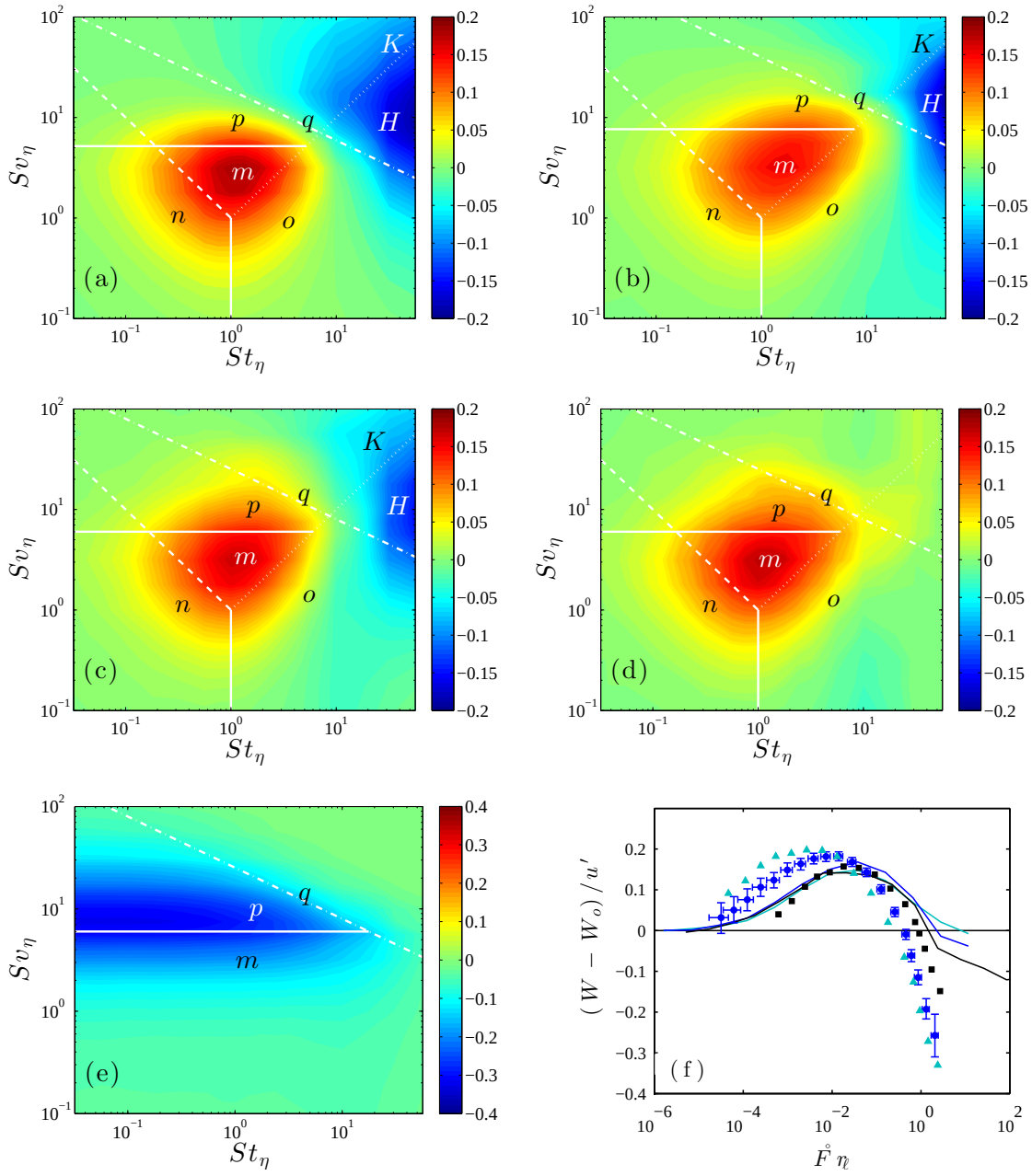

Figure 4.3: $(W - W_o)/u'$: S1 (a) and S3 (b) (nonlinear drag); S2 with nonlinear drag (c), linear drag (d) and forced loitering (e) models. Contour plots have lines of unity St_η, Sv_ℓ, $\mathring{S}t_\eta$ (-1 slope), Fr_η ($+1$ slope) and $\mathring{F}r_\ell$ ($-1/2$ slope). Plot (f) has E1, E2 and E3 (light and dark blue and black symbols), sample error bars for E2, and S2 (nonlinear drag) data lines interpolated to each experiment's fixed $Fr_{a'}$, matched by color. Each experiment has an abscissa error of $\sim 0.05u'$, separate from the error bars.

not indicate a false choice of scale, as $\mathring{F}r_\ell/\mathring{F}r_\eta = 5820$ (S2).

4.3.2 Particle fluctuating velocities

We proceed by looking at the particle r.m.s. velocities as being indicative of their motion. We are interested in both the characteristic particle velocity fluctuations as compared to the turbulence, u'_p/u', and the anisotropy of the particle motion, v'_p/w'_p.

A contour plot of u'_p/u' is shown in figure 4.4a. For $St_\eta, \mathring{S}t_\eta < 1$ (region N), inertial effects are minimal and u'_p/u' is approximately unity. The response is attenuated for heavier particle classes, and u'_p decreases as a function of $St = \tau_p/\tau_r$ for $Sv_\ell < 1$ (region J) and of $\mathring{S}t \equiv \tau_p/(r/W_o)$ for $Sv_\ell > 1$ (region P). This shows St to be the appropriate inertial parameter where gravitational effects are weak or absent and $\mathring{S}t$ again to be where they are strong, with Sv_ℓ determining which timescale is relevant. The experimental data confirm the new result of region P in figure 4.4b; the measurements collapse on constant Fr lines as functions of $\mathring{S}t_\eta$. The decreases are similar to in the S2 (nonlinear drag) data.

The particle motion anisotropy, v'_p/w'_p, is shown in figure 4.5. In region N, inertial and buoyancy effects are minimal and particles closely reflect the isotropy of the turbulence. The anisotropy is otherwise such that the vertical r.m.s. is greater, likely as particles have more time to respond to vertical fluctuations than horizontal ones while falling over vertical distances, since the longitudinal integral scale is twice the transverse one. The anisotropy decreases as a function of St in region j ($Sv_\eta < 1$) and of $\mathring{S}t$ in region P ($Fr_\eta > 1$). Like with u'_p, these Stokes numbers dominate for weak and strong gravitational effects, re-

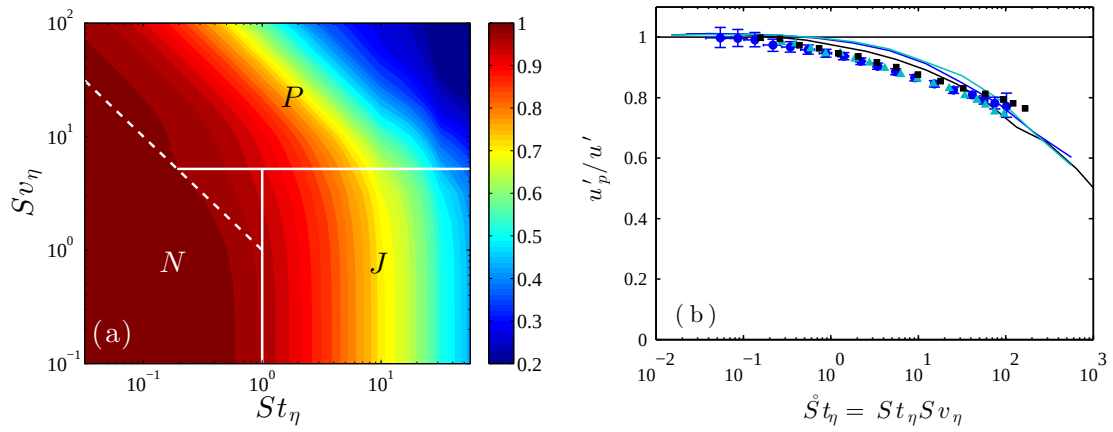

Figure 4.4: u'_p/u': S1 (linear drag) (a) and lines of unity St_η, Sv_ℓ and $\mathring{S}t_\eta$ (-1 slope); Plot (b) has E1, E2 and E3 (light and dark blue and black symbols), sample error bars for E2, and S2 (nonlinear drag) data lines interpolated to each experiment's fixed $Fr_{a'}$, matched by color.

spectively, though the criteria are different than for figure 4.4a. v'_p/w'_p is also a function of St for $Sv_\eta < 1$ and there are Sv-parallel contours for $Sv_\ell \sim 1$ in region H. Particle motion anisotropy is significant here, and most so in region K. The DNS indicate the variation to go dominantly with Sv_ℓ for the Froude numbers of the experiments, and we in fact see excellent agreement between experiment and DNS for v'_p/w'_p in figure 4.5b.

The other simulation results are qualitatively the same. The general difference is that the picture is stretched either with greater R_λ (and thus scale separation) or with with nonlinear drag, with which the particles have a lower effective response time, τ_p/C_D. The S1 linear drag case thus shows the fullest picture across the same St_η range. We see for instance from v'_p/w'_p in figure 4.5a that for $St_\eta \gtrsim 10^2$, particle motion anisotropy starts to return to unity for $St \to \infty$ (constant Sv), a feature not captured in the other simulations' more limited ranges

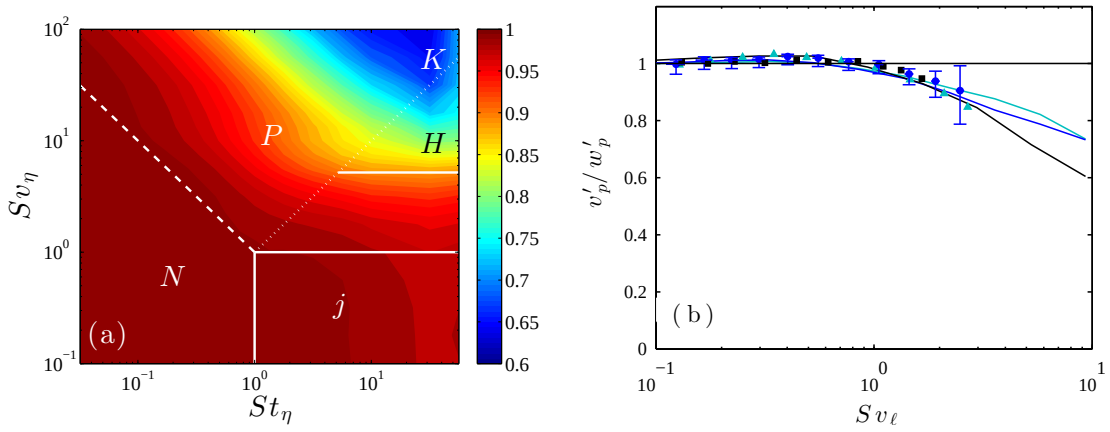

Figure 4.5: v'_p/w'_p: S1 (linear drag) (a) with lines of unity St_η, Sv_η, Sv_ℓ, $\mathring{S}t_\eta$ (-1 slope) and Fr_η (+1 slope); Plot (b) has E1, E2 and E3 (light and dark blue and black symbols), sample error bars for E2, and S2 (nonlinear drag) data lines interpolated to each experiment's fixed $Fr_{a'}$, matched by color.

of inertial effects. The Sv limit is not obvious, as the lowest value of 0.6 is not a minimum, and it is likely that v'_p/w'_p tends to either zero or 0.5 (the transverse to longitudinal integral scale ratio) for infinite gravitational effects, as these limits maintain the two-dimensionality of the axisymmetric system with gravity.

The $w'_p > v'_p$ and $W < W_o$ (figure 4.3a-c) regions largely coincide, with particles whose settling is strongly slowed by nonlinear drag effects also much more sensitive to the vertical rather than to the horizontal motions of the turbulence. This builds on the general picture that horizontal motions allow fast-tracking, while vertical ones are important to both the loitering and nonlinear drag settling-speed-reducing mechanisms.

4.4 Conclusions

Particle response to turbulence varies widely based on inertia and buoyancy, and we find a variety of particle parameterizations to be key in different regimes. The results closely detail this parameter space using a large array of particle fields simulated by DNS and show good agreement with new experiments.

Within the fast-tracking regime (regions *m*-*p*, figure 4.3a-d), we identify regimes with $\mathring{S}t$, Fr or Sv as key to determining $(W - W_o)/u'$. The $\mathring{S}t$-dependence ($\propto g\tau_p^2$) is a new result, perhaps not previously observed in turbulence models (Dávila and Hunt, 2001) due to their stationary or reduced dimensionality. We also confirm the dependence and bounding of the fast-tracking regime on $\mathring{F}r_\ell$, as proposed by Dávila and Hunt (2001).

The loitering mechanism (figure 4.3e) is likewise bounded by $\mathring{F}r_\ell = 1$ and is strongly a function of Sv for $St_\eta < 1$, peaking at $Sv_\ell \approx 1$ (Kawanisi and Shiozaki, 2008). It would be significant except for horizontal motions and prevalent fast-tracking events increasing settling speeds overall. It may however physically explain decreases in $(W - W_o)/u'$ with increasing Sv. At least for water droplets in air or simulations thereof, the loitering and nonlinear drag settling reduction mechanisms do not coincide. The nonlinear drag mechanism reduces settling velocities in regions H and K (figures 4.3a-c), as determined by its critical parameters, Fr_η and $\mathring{F}r_\ell$.

Two parameters are necessary criteria for a particle to behave like a tracer and reflect the mean flow, variance and isotropy of the underlying turbulence: St_η and $\mathring{S}t_\eta$ (figures 4.3a-d, 4.4-4.5). The latter is generally overlooked and of

some real-world utility. u'_p, decreases with St for $Sv_\ell < 1$ and with $\mathring{S}t$ for $Sv_\ell > 1$ (figure 4.4). For the anisotropy, there is always greater response to vertical fluctuations ($v'_p/w'_p < 1$), likely as the longitudinal integral scale is twice the transverse one. The anisotropy has regimes where it is strongly dependent upon St, $\mathring{S}t$, or Sv (figure 4.5). Anisotropy and settling reduction effects vanish for infinite St, while v'_p/w'_p should tend to 0.5 or zero for infinite Sv. Strong anisotropy coincides with settling speed reductions due to nonlinear drag, which together with the loitering description show that while horizontal motions are responsible for fast-tracking, vertical fluctuations are rather responsible for both settling reduction mechanisms.

We would like to thank Heng-Dong Xi and Ewe Wei Saw for their helpful discussions and Denny Fliegner for his assistance with computational resources. This work was supported with the generosity of the German-American Fulbright Commission, the Max Planck Society, and the National Science Foundation.

CHAPTER 5
CONCLUDING THOUGHTS

Three independent studies have been completed as part of this dissertation. In chapter 2, a novel flow was presented in which turbulence with both narrow and extended tails of the velocity distribution were observed. Such flows are common in nature, such as in the atmospheric boundary layer, where the increased frequency of strong gusts in multi-scale turbulence reduces the lifetimes of wind turbines. In particular, the moments of the distributions were shown to depend upon the spatial variation of the velocity r.m.s., with odd moments and even moments dependent upon the first and second spatial derivatives, respectively. Unskewed, sub- and super-Gaussian turbulence results from spatial troughs and peaks in the turbulent kinetic energy, due to the flux of this energy. Some effect was even clear on the moments of the derivative of the velocity field, which is rather representative of the small scales of the turbulence. Comparisons are drawn to planar jets and environmental flows, fractal grids, and the near and far fields of typical grid turbulence.

Chapter 3 presented two particle mixing layers in which a particle-laden flow entrains a dry air flow. In one case, the turbulence was homogeneous across the wind tunnel. In the other, the dry flow was originally quiescent, with a steep gradient in turbulent kinetic energy following downstream. This inhomogeneous interface, like in the chapter 2 flows and at the boundary of a cloud, is characterized by the expulsion and entrainment of large-scale swaths of fluid. Such swaths exist even in the case of homogeneous turbulence, though they are distinguishable only by their droplet content there, and not by any difference in turbulence properties. The droplets were shown to penetrate far

across the interface in large-scale clusters, before dispersing to become more homogeneously distributed. Due to this process, droplets found furthest from the seeded region actually had the most similar ambient conditions to it, as they were most freshly deposited. The mean velocities and number densities of the droplets were shown to be similar to those expected from a smooth, diffusive process, despite the intermittent nature of the turbulent entrainment. Particle size measurements, radial distribution functions, conditional statistics, and the moments of their velocity pdfs gave evidence to their sampling of the velocity field and the preservation of their ambient conditions by entrainment in bulk.

Chapter 4 took a more fundamental look at the motion and settling of single particles in isotropic turbulence. We used a new turbulence apparatus to study particle settling in isotropic conditions and validate results from an unprecedented range of inertial particles studied by direct numerical simulation. By doing a simulation in which particles were confined to vertical paths, we were also able to isolate the three settling-speed-modifying mechanism of fast-tracking, nonlinear drag and loitering for the first time. We also showed the settling speed modification, particle field velocity variance and anisotropy to vary based on a number of particle parameters. While only two are needed to describe the two-parameter space of inertia and buoyancy, any of five has its own physical significant and effect, comparing gravitational accelerations to fluid ones, or particle response time, Stokes velocity, falling time past an eddy or typical path length around an eddy to turbulent eddy scales of the carrier flow. The anisotropy is always such that particles are more sensitive to vertical fluctuations, since they fall mostly vertical paths and the longitudinal correlations of a turbulent velocity field are greatest. We show the vertical fluctuations to be responsible for both the loitering and nonlinear drag mechanisms, which

slow settling speeds, while the horizontal motions are those critical to settling speed enhancements. We paint the most comprehensive picture to date of inertial particle response to turbulence.

The three projects motivate a number of avenues for further work. Regarding the study of multi-scale flows in Chapter 2, we note that the large-scale intermittency was generated by inhomogeneity between two mixing layers with shear. The cross-correlation coefficient was a good indicator that large-scale intermittency was greatest where the two mixing layers exactly met. The role of shear should however be examined by removing it from the flow. It might be removed by placing screens in the grid gap so that the turbulence is generated between two shearless TNIs, each like that in Chapter 3 or found in Veeravalli and Warhaft (1989).

The more interesting case may be to see what features of the Chapter 2 flows can be mimicked under statistically stationery and isotropic conditions, without the mean turbulent kinetic energy gradients of the flows in the present work. Both DNS and soccer-ball type turbulence might be ideal to this end. In DNS, turbulence can be forced, for example, at two distinct scales. Of particular interest are the bimodal nature of the measured velocity pdfs and a possible connection to bumps in the velocity spectra, which perhaps contain energy supplied at two scales which does not transfer down the combined spectrum in a way which makes it smooth. The forcing conditions of the soccer ball are also easily manipulated. The noise functions controlling the amplitudes of each jet could certainly be made to be of a form which would produce long tails for the velocity pdf, or perhaps signals with different correlation times could create a multi-scale signature in the flow, though the integral scale varies by small amounts in

the Göttingen apparatus. Such numerical and laboratory studies could be very revealing regarding the common, though not well understood irregularities in the velocity spectra of turbulent flows in nature.

In the case of Chapter 3, the TNI droplet mixing layer was compared to mixing in homogeneous turbulence and the role of gravity was isolated by rotating the apparatus, isolating many effects present at boundaries above, below and at the sides of clouds. Shear and coherent structures are however also typical at cloud boundaries. These may play a significant role in determining the rate and scales at which entrainment occurs. The TNI mixing layer studied here could be easily modified to have shear.

The entrainment of particles with yet greater inertia than those studied in Chapter 3 is also of interest, particularly with regards to at which point entrainment no longer occurs in bulk, and to what conditions of turbulence and humidity such particles instead see. It is also uncertain which of the particle parameterizations of Chapter 4 the particle entrainment depends upon and whether this varies in the three gravitational cases of the different sides of clouds.

For larger droplets in clouds, settling clearly plays a role in droplet dynamics, as studied in Chapter 4. It was shown there that settling particles respond anisotropically to even isotropic turbulence. We ask the question as to the case where turbulence is anisotropic, as is common in many real flows. Bewley et al. (2012) showed that in turbulence with axisymmetric anisotropy, the ratio of the integral scales along and orthogonal to the line of symmetry goes nearly as the cube of the anisotropy in the velocity r.m.s, and could thus be as much as 5 or more in typical shear flows. This is important in the picture of settling particles requiring transverse motions to side-step upward-moving flow, as turbulence of

a given Reynolds number may have very different horizontal spacing of these regions, thus affecting whether the turbulence enhances or reduces particle settling speeds. Particles may be more able to fast-track if the larger eddies are thin and long in the vertical direction, and vice versa. On the other hand, it may be that it is the vertical velocity r.m.s. to which the settling reduction mechanisms are sensitive, which could cause the opposite trend with anisotropy as is suggested by the integral scale argument. An initial attempt was made to measure settling speeds in two anisotropic flows, with axisymmetric anisotropy of 0.67 and 1.5 in the vertical direction, but a consistent result was not immediately met. This is certainly an avenue of interest. With the soccer ball apparatus, one might also investigate to the three-dimensional problem where gravity is orthogonal to the axis of symmetry of the anisotropy. In the case of a prolate r.m.s. ellipse, this is as the case for particles settling in a boundary layer, as occurs for sedimentary flows, excepting of course for mean shear in the flow. One would also wish to isolate the effects of coherent structures due to mean shear on particle settling speeds.

The anisotropic behaviour of inertial particles even in isotropic turbulence also raises questions as to how it might affect their inertial clustering. This was in fact an initial motivation of the study, with the idea being that if particles select downward-moving regions of strain in contrast to regions of strain in general, they might be clustered more in planes orthogonal to gravity than they are in planes parallel to gravity. A novel point here is that clustering could actually increase for certain particle classes with gravity; it has only previously been reported that gravity disrupts clustering by diminishing particle response to turbulent eddies (Wang and Maxey, 1993). The DNS data used in Chapter 4 in fact confirmed the hypothesis and yielded many interesting results to this

end, and are currently being studied by Peter Ireland. It would be quite difficult to replicate these results experimentally, as they are most interesting for large particles for which the one-way coupling approximation would be lost with the required seeding densities of a clustering study. Additionally, fields of large particles require some time to reach statistically-stationary states, and their settling speeds would necessitate very large experimental apparatuses for the study of their clustering.

There are thus a number of problems requiring further attention for which the papers presented here may provide some foundation. It is the author's hope that the thesis provides some motivation for inquiry into the avenues of future research described here and inspired by the culmination of this doctoral work.

APPENDIX A

EXTENDED DETAILS OF THE EXPERIMENTS

It is the purpose of this appendix to provide extended details for the thesis regarding the experiments and methods described more succinctly within the chapters/papers therein. The elaboration is provided in two parts: firstly, on the wind tunnel work conducted at Cornell (Chapters 2 & 3) and, secondly, on the experiments conducted in the soccer ball apparatus of the Max Planck Institute for Dynamics and Self-Organization (Chapter 4). The apparatus in Göttingen is particularly unique, and the author's personal notes on its use and capabilities are offered as well.

A.1 DeFrees Laboratory Wind Tunnel Experiments

A.1.1 The wind tunnel and grid

The DeFrees Laboratory wind tunnel is 20 meters long and has an open-circuit configuration. It has an approximately square cross section of dimensions 100 x 95 cm. It was designed for alternative utility as a flume, with a wooden roof in the wind tunnel configuration and concrete floor. The side walls are glass, allowing both PDPA and camera particle tracking techniques without any protrusions into the flow.

High-Reynolds number turbulence is generated in the wind tunnel via an active grid like that described in Mydlarski and Warhaft (1996). It is actually that of Mydlarski and Warhaft (1998), 91x91 cm in size, and originally designed for the wind tunnel of the same dimensions in Yoon and Warhaft (1990). The

DeFrees tunnel was adapted for use with the grid with sheet metal ductwork extending approximately 50 cm up- and downstream of the grid apparatus. The tunnel does not have a contraction or proper straightener and relies on the active grid to negate any inhomogeneities at the inlet. The grid consists of independently-rotating rows and columns of winglets (10x10 cm squares), which are operated in the random mode, by which their direction of rotation changes at random. Some winglets are perforated in order to reduce the blockage ratio of the grid. Some perforated winglets were used in the grid configurations of the Chapter 2 flows, in order to reduce the amount of shear generated between the grid and grid gap. In the Chapter 3 entrainment flow, non-perforated plates were used in an arrangement where four screens were positioned opposite the splitter plate and spaced just such that they balanced the drag of the grid, for the purposes of creating the non-turbulent side of a shearless interface. The author credits Sergiy Gerashchenko with this design (Gerashchenko et al., 2011).

The test section was chosen in Chapter 2 based on peak transverse velocity kurtosis, found with hot-wire measurements every 5 cm downstream of the grid. (It is noted in Chapter 2 that for flow 1, the location may be slightly displaced from the peak). For Chapter 3, Lagrangian measurements were desired in tandem with Eulerian measurements, and so the measurement station was set at the center of the half meter distance over which the Lagrangian particle tracking sled system acquires data, 1.17 m downstream of the splitter plate trailing edge. The splitter plate itself was 2.5 meters long.

A.1.2 Hot-wire data

The hot-wire work of Chapters 2 and 3 was conducted with TSI 1241 X-probes with tungsten wires, 3.05 microns in diameter. The copper-coated wires were provided by Laurent Mydlarski and were soldered and etched in house. The probes were calibrated in the lab over a jet orifice by the method of Browne et al. (1989) at angles 0°, ±4°, ±8°,..., ±20°.

For the large-scale intermittency work of Chapter 2, higher-order statistics were of interest. Samples were taken until the velocity pdfs could be resolved to up to ±5 standard deviations from their means, taking nearly one half hour per measurement (200-250 data blocks each). The greatest concern with the long-running measurements was the fading accuracy of the probe calibration with time, as the profiles each took around ten hours to complete. The two, independent measurements on both sides of the ideally symmetric flows generally showed good agreement, however. The full profiles were shown to illustrate both the symmetry of the flows and to indicate the accuracy of the measurements (chiefly dependent upon the calibration), which was sufficient not to be problematic to the points of the study.

For the chapter 3 entrainment flows, the hot-wire work was done in the absence of water droplets. The collision of water droplets with hot wires in droplet-carrying flows typically results in spikes in the probe signal. Some groups have claimed success in filtering out these spikes. It was not however deemed crucial in our case to have the water droplets present for the hot-wire, velocity field measurements. The momentum and turbulent energy provided by the nozzles was simply maintained by supplying both inlets of the coflowing nozzles with air, rather than with both air and the water necessary to create

a spray. For the turbulent-turbulent interface (TTI), where homogeneous turbulence was desired, all experiments were carried out with the dry side of the flow having these same air jets to match the effect of the water sprays on the seeded side of the flow.

The ideal cases of the Chapter 3 interfaces would be completely homogeneous turbulence properties for the TTI and a clean step in the turbulence properties for the turbulent-non-turbulent interface, with initially homogeneous properties on either side of the splitter plate, and likewise for the droplet number density. Some variation in these properties of course existed in the experiments, as seen in figure 3.3. The error bars shown in the figure simply illustrate the maximum observed variation on both sides of the flows, which was slightly more than the imprecision of the measurements of the high-energy turbulence presented in table 3.1, as in Gerashchenko et al. (2011). These were based on different hot-wire measurements from independent realisations of the flows. It should be noted that the mean velocity profile matched that measured by the PDPA within error, which is as expected, since this quantity should not be affected by the droplet inertia.

A.1.3 Droplet seeding and PDPA data

Water droplets were seeded in the entrainment flows via 3 coflowing air and water nozzles. The active grid turbulence, generated 5 cm upstream of the sprays, was critical to more-homogeneously distributing the droplets and spray momentum before the end of the splitter plate. The effect of inhomogeneities in this are discussed in appendix B (Good et al., 2012).

The sprays could be tuned to adjust the size distribution. This was however kept constant throughout the experiments. What could however unfortunately not be controlled was the long-time variation in the output of the sprays. The droplet number density produced by the sprays was measured by the PDPA to fluctuate in time with a period of about 30 minutes, typically between 200 and 300 droplets per meter through the PDPA cross-section. Since droplet mean number density measurements in the mixing layer must be compared to that simultaneously present in the bulk, it was necessary to check the bulk mean number density directly before and after each mixing layer measurement, linearly interpolating the bulk value for each mixing layer measurement. Droplet number density measurements were thus completed over very short times of about one minute, small compared to the timescale of the spray output variation. Particularly at the edge of the mixing layers, where droplet mean number densities were small, various independent measurements needed to be combined to obtain sufficient statistics of typically tens of thousands of individual measurements. The error function profiles measured for the TTI validate the method, also used in Gerashchenko et al. (2011).

For droplet velocity statistics and radial distribution function measurements in the mixing layers (with the latter using a moving average mean number density), the variation of the bulk mean was not of importance, and so separate data from longer time series including hundreds of thousands of individual measurements were used. Velocity measurements from these time series also confirmed the hot-wire profiles and confirmed the tunnel to perform consistently between experiments.

Between five and ten independent number density measurements were com-

pleted for each location in the mixing layer, depending upon how sparse the droplets were at a given location. The confidence intervals for the mean droplet number densities were calculated from these using the bootstrap, resampling method (Efron, 1979). This method was also used for the velocity moments calculated from the longer data sets with many more data points. The bootstrapping method requires populating N copies of the data set with random values from the original, and calculating the desired statistic for each copy. It is the author's experience that $N = 5000$ safely produces smooth cumulative distribution functions of the calculated quantities, from which confidence intervals may be extracted.

A.1.4 Lagrangian data

For the acceleration measurements of the entrainment study, the pneumatically-driven Lagrangian particle tracking sled of Ayyalasomayajula et al. (2006a) was used. Particles were illuminated via forward scattering from a 20 W, 40 kHz pulse (120 ns width) Nd-YAG laser. The particles were filmed with a high-speed, Phantom v.7.1 camera capturing 8000 fps on 512x512 pixels. The camera rests about 40 cm above the wind tunnel floor. Measurements are presented from the g0 TNI mixing layer, for which different locations in the mixing layer were reached by zooming of the camera. The measurement window thus varied from about 2.5 to 4 cm in width.

The gravitational cases were also measured using a new periscope assembly attached to the sled, with which different locations in the mixing layer (at different heights in the tunnel) could be measured. These measurements were

eventually abandoned, however, as the particles could not be sized and the size distribution as measured by the PDPA changes as a function of position in the mixing layer in the gravitational cases due to gravitational settling. Given the constant size distribution and Stokes numbers of the particles throughout the g0 mixing layer, this case was chosen to assess changes in the turbulence observed by particles in the TNI.

Acceleration statistics were computed from about 2 million individual measurements for each mixing layer position, with the acceleration pdfs being smooth to over ±10 standard deviations. The large uncertainty in the acceleration measurements is due to that in particles positions. The error bars shown represent an uncertainty of a half pixel, a conservative estimate, as the particle tracking code (Ouellette et al., 2006) determines particle centers using Gaussian filtering. The uncertainty was not problematic to confirming the preserved turbulence conditions ambient to the particles in the TNI mixing layer.

A.2 Göttingen Settling Experiments

A.2.1 Soccer ball apparatus

Basic description

The original Göttingen soccer ball apparatus is described in Chang et al. (2012), with 32 loudspeaker jets on 16 axes focused by truncated cones with 10 cm openings. The speakers are mounted on the 32 faces of a wooden truncated icosahedron, the shape of a soccer ball. The device is able to create very isotropic

turbulence at its center (with orthogonal velocity r.m.s. components matching to within $\sim 1\%$), where the jets converge, but also turbulence of a range of desired anisotropies. The second version of the device at the MPI-DS uses a nearly spherical acrylic chamber, with the speakers positioned as in the first device. The acrylic apparatus was used for this work.

The speakers are independently driven with 50 Hz sinusoidal signals whose amplitudes are set by exponentially correlated colored noise (Fox et al., 1988) of correlation time 0.1 seconds. The mean signal from all 32 speakers is always conserved to be zero for volume conservation in the chamber (by subtracting the mean signal from each signal), without which there is noticeable vibration of the apparatus, though the ball is not sealed and can exchange air with its surroundings. Under ideal operation, the r.m.s. velocity in the chamber increases linearly with the mean signal amplitude. There is some fear that large-scale flows are eventually generated within the soccer balls during extended operation; this is not a concern for the settling experiments, as the turbulence was only generated for about one minute while data was taken on the cameras, before long pauses for data downloads.

Generating anisotropic turbulence

Axisymmetric anisotropy was controlled in the driving code of Chang et al. (2012) by modifying the power sent to speakers based on their locations. Two speakers (on hexagonal faces) were chosen as poles on the axis of symmetry. One can picture the anisotropic flow as having an r.m.s. ellipse, whose major and minor axes are chosen components of the velocity r.m.s. During anisotropic driving, the signal amplitudes were multiplied by some constant, depending

on the nearness of the speakers to the equator or poles. This constant was the radial distance to the surface of the desired r.m.s. ellipse from its center, at the angle where the speaker was located (Chang et al., 2012). The anisotropy of the measured turbulence was observed in Chang et al. (2012) to match the anisotropy of the amplitude ellipse for anisotropies between 2/3 and 1.5, representing oblate and prolate spheroids, respectively, beyond which the turbulence anisotropy no longer responds linearly, as the turbulence becomes sensitive to the increasingly limited number of speakers providing considerable energy to the flow. (The speakers cease to create jets if the amplitudes are too low). Chang et al. (2012) showed the achievable anisotropy to saturate as a function of the driving anisotropy at about 0.5 and 2.

For the new experiments, the code was altered to accept three arbitrary axes of anisotropy, with the wish to control anisotropy along axes parallel and orthogonal to gravity. An attempt was also made to input an origin for the ellipse to correct for the typical mean flows of up to 10% of u' which exist in the apparatus. This feature was not used for the experiments, however, as some mean flow would exist and need to be measured in any case. In order to make corrections to the driving parameters to obtain desired conditions, a 3D laser doppler velocimetry (LDV) system (TSI Inc.) was installed around the ball and used with fog droplets for real-time measurements. The LDV system could not be used during the settling experiments, as the fog droplets obstruct the cameras. For lower Reynolds numbers, orthogonal r.m.s. components were the same within about 1% with isotropic driving. With increased power, the flow became more sensitive to mechanical differences in the speakers, with this difference becoming more like 5% at the Reynolds number of the Chapter 4 experiment 3, which was however corrected by driving the system slightly anisotropically in

the other direction.

As discussed in Chapter 5, some attempt was made to measure droplet settling in anisotropic turbulence. In this case, speakers were not located on the vertical axis of symmetry of the anisotropy, as water droplets were seeded directly from above through the space between a hexagonal and pentagonal speaker. (This orientation of the apparatus was perhaps not ideal to experiments with gravity, as the speakers are not symmetrically arranged with regards to the vertical). Under this arrangement, anisotropies between 2/3 and 1.5 were achievable. More exaggerated forcing mechanisms were attempted, where the power sent to speakers increased or decreased by power laws or exponentially, given their distances along different axes. Anisotropies between 2/3 and 2 were then again achievable, but the flows were not desirable, as this turbulence is not well-characterised and is highly sensitive to the locations of the few number of speakers driving it, unlike for the ensemble turbulence of all 32 speakers.

A very different driving mechanism was also attempted to suppress fluctuations along a given axis. The turbulent fluctuations in the soccer ball turbulence are thought to be some combination of the fluctuations within the individual speaker-generated jets, and the give and take of jets coming from different directions due to their mean speeds. (It is not clear that the wide, loudspeaker-generated jets act like classical jets, whereby both the mean and r.m.s. velocities of individual jets should likewise linearly depend on the driving signal amplitude). Similarly to how the mean signal sent to all jets is instantaneously conserved to be zero for volume conservation, the attempt was made to instantaneously balance the momentum of all jets along given axes to be, for example, zero. The operating mode produced no observable anisotropy with the

signal amplitudes themselves being equal, however, either fundamentally because of interference from turbulence surrounding the central spot where the jets are meant to cross, or inexact alignment of the jets (which may be better in the Chang et al. (2012) device). While the idea was only quickly tested here, if it proved to work under other conditions, it would be a superior operating mode for anisotropic flows to the one currently used in the soccer balls, which degrades the power and number of the jets.

A.2.2 Particles and measurements

Droplet generation and seeding

Water droplets were generated using a Sono-Tek Inc. ultrasonic nozzle. The nozzle is machined to a precise length and vibrates piezoelectrically at 25 kHz such that water wetting its tip breaks into droplets due to capillary wave instabilities. A conical tip shape was chosen to more broadly distribute the droplets. The nozzle tip was 0.5 inches in diameter with a 0.086 inch orifice at its center, through which water was supplied. The nozzle is manufactured for a maximum flow rate of 1.2 ml/s. The nozzle ideally produces the same size distribution regardless of flow rate, though in practice has some minimum (some percent of the maximum for this nozzle), below which it produces droplets intermittently. The droplets were seeded just above the top of the ball, and measurements were taken at the ball's centre. The size distribution measured there is shown in figure A.1.

It is generally given that the particle to fluid volume ratio, ϕ_v, should be of about order 10^{-5} or less for water droplets to have negligible effect on surround-

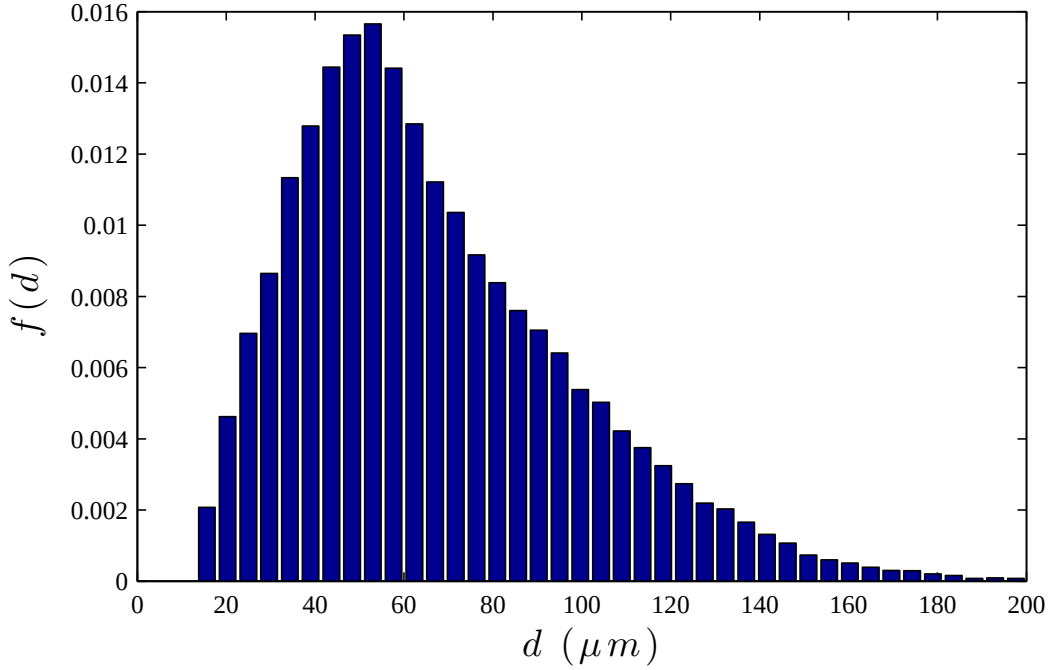

Figure A.1: Droplet size distribution as produced by ultrasonic nozzle and measured a half-meter below at the centre of the soccer ball apparatus by shadow imaging.

ing air turbulence (Elghobashi and Truesdell, 1993; Sundaram and Collins, 1999; Bosse and Kleiser, 2006). With gravity, one should also calculate the energy supplied to the flow by the particles' collective drag force, this energy rate being the product of the drag force and terminal speed for the sum of the droplets in the flow, $\phi_v \frac{\rho_p}{\rho} g \cdot \tau_p g$ for monodispersed droplets. For polydiserpsed droplets, this must be calculated from the size distribution for a droplet of diameter $\langle d^5 \rangle^{1/5}$. The necessary condition is then that $\phi_v \frac{\rho_p}{\rho} \tau_p g^2 / \epsilon \ll 1$. Bosse and Kleiser (2006) showed no visible effect on the turbulence (velocity spectra) where this can be calculated to have been around 1% and only negligible changes for a value reaching 8%. Aliseda et al. (2002) already saw small effects of particle loading on the mean settling speeds of water droplets in air turbulence for $\phi_v = 10^{-5}$, with the data indicating the effect might vanish for $\phi_v \lesssim 10^{-6}$.

To ensure the one-way coupling regime, the Chapter 4 experiments aimed for $\phi_v \approx 10^{-6}$ and $\phi_v \frac{\rho_p}{\rho} \tau_p g^2/\epsilon \approx 1\%$. For experiment 3, this was satisfied within the measurement volume with a flow rate of 0.1 ml/s to the nozzle with its tip positioned 8 cm above the ball. For experiments 1 and 2, lower seeding rates were necessary than allowed by the minimum flow rate of the nozzle. The droplets were then instead sprayed through a hole formed by nylon pipe nipple (1 cm in diameter and 5 cm long), with droplets falling to the side captured and the water drained away. For experiment 1, the nozzle was operated 7 cm above the nipple with a flow rate of 0.5 ml/s. For experiment 2, the nozzle had a flow rate of 0.33 ml/s, 2 cm above nipple.

Particle tracking and sizing

The settling measurements were done via two-dimensional particle tracking with a high-speed camera. The nature of the data was however Eulerian, with the camera system being used due to its larger measurement volume and more accurate particle sizing capability than would have been possible with phase Doppler particle analysis. The large measurement volume was necessary because of the very low droplet seeding rates, with which sufficient statistics could not be gathered with a PDPA measurement volume, despite the advantage of being able to collect data continuously, whereas the camera required about 20 minutes of download time for every 1 minute of collected data.

The videos were taken with a Phantom V640 camera fitted with two Kenko N-AF 2X Teleplus Pro 300 teleconverters and a Nikon AF Micro Nikkor 200 mm 1:4 D lense, with the lense about 40 cm from the measurement volume. The shadow-imaging technique was used, where a Thorlabs high intensity fiber

light source was used to shine a light beam from the opposite side of the ball directly into the lense of the camera. The beam was made wide enough so that the brightness was nearly constant across the measurement volume. The system and optics were the same as in Bewley et al. (2013), such that both experiments could be conducted in parallel. (The Bewley et al. (2013) experiment however also used a second camera for 3D particle tracking). The measurement volume was about 1.6 mm on a side in a window of 512 x 512 pixels, such that each pixel represented 3.2 microns. To increase data rates for the 2D settling measurements, the f-stop of the lense was increased from the Bewley et al. (2013) configuration to 16 for experiment 1 and 22 for experiments 2 and 3. The depth of field was thus about 2.5 mm for experiment 1 and 3.5 mm for experiments 2 and 3, resulting in an error below 0.5% regarding sizes and lengths on the camera due to the depth of field, which was small compared to uncertainties from the pixel-limited resolution of the camera. Data was taken at 4000 frames per second for experiments 1 and 2 and at 5000 frames per second for experiment 3. The background value in the image was about 125 (with droplet edges being 85 or darker) for experiment 1 and 100 for experiments 2 and 3, (with droplet edges being 70 or darker). The background image of each video was independently averaged over all frames, helping eliminate a few percent fluctuation in brightness due to the power source (50 Hz frequency). The average image was then subtracted from every frame.

The 2D, Matlab tracking code made publicly available by the Ouellette group at Yale (http://leviathan.eng.yale.edu/) was used, as it was fast enough for the simple tracking done here, and relatively easy to modify. Sizing was done using the Matlab imaging toolbox, with sizes assigned from the major axis of the smallest ellipse which could be fitted to particle images. This method seemed

more robust regarding truncated particle images at the edge of the measurement volume than a pixel-area-based method, which also discounted the few lit pixels (1 to 5) which appeared at the centers of the shadows of very large droplets due to light shining through them. The droplets were always observed to be spherical.

The low seeding densities meant there were order 10^{-2} droplets per camera image, on average. Droplet tracks were seldom near each other and visual inspection of the tracks confirmed proper operation of the algorithm. The tracks were very straight and typically vertical for the settling particles, with negligible variation in the measured speeds or droplet size along them. Particles were found with the criteria of a minimum contrast of 25 to the background and a 10 pixel area minimum. (The smallest observed particles were about 13 microns in diameter). Typical particle displacements between frames were about 20 pixels. The tracking code looked for particle matches with maximum displacements of 100 pixels between frames, given the particles' Stokes and turbulence velocities and the displacements observed directly in the images.

Individual particles were measured about 20 times along their tracks, on average. As Eulerian measurements were sought, only the median size and velocity of each tracked particle were counted towards ensemble statistics. This method eliminated issues from averaging data points including truncated particle images or images of two crossing particles which might confuse the tracking code, though this appeared to occur for less than 1% of particle tracks. Given the short times and distances over which the inertial particles were tracked, no filtering effect is expected from this, and there was no noticeable difference to the statistics overall from taking simple averages from the tracks.

A.2.3 Characterizing the turbulence

Both the turbulence r.m.s. and flow mean velocities needed to be measured for the settling experiments. Ideally, small fog droplets would have been used as tracer particles, measured by the PDPA system concurrently to the Lagrangian measurements of the larger droplets, which were too few to be measured by the PDPA. Unfortunately, the fog obstructed the camera system and so the experiments were conducted without it and these quantities were instead extracted from the Lagrangian data.

The mean and r.m.s. velocities of the droplets were plotted as functions of the droplet size. For the mean, the Stokes velocity of each droplet was first subtracted from its measured velocity. The limit as $d \to 0$ for both of these quantities ought be the air turbulence mean and r.m.s. velocities. Points were plotted as functions of both d^2 and d^4, whose importance was indicated by the Chapter 4 DNS data. In either case, the same answers were given within error. Both the r.m.s. and means were plotted as functions of particle size, given overlapping size bins in log space, sufficiently wide as to prevent scatter from insufficient numbers of particles in the bins, and overlapping such that the points were close enough as a function of size to smoothly resolve the trends in the mean and r.m.s. velocities. The velocity field mean and r.m.s. velocities could then be linearly interpolated to the value for a zero-sized particle from bins of droplets below 25 microns. Conservatively, this method was accurate to within 1 cm/s for u' and to about 5% of u' for the mean.

The single-point measurements were insufficient for directly determining ϵ and thus R_λ or ℓ as well. The variation of these quantities as functions of u' could however be determined from calculations of ϵ from the 3D particle tracking

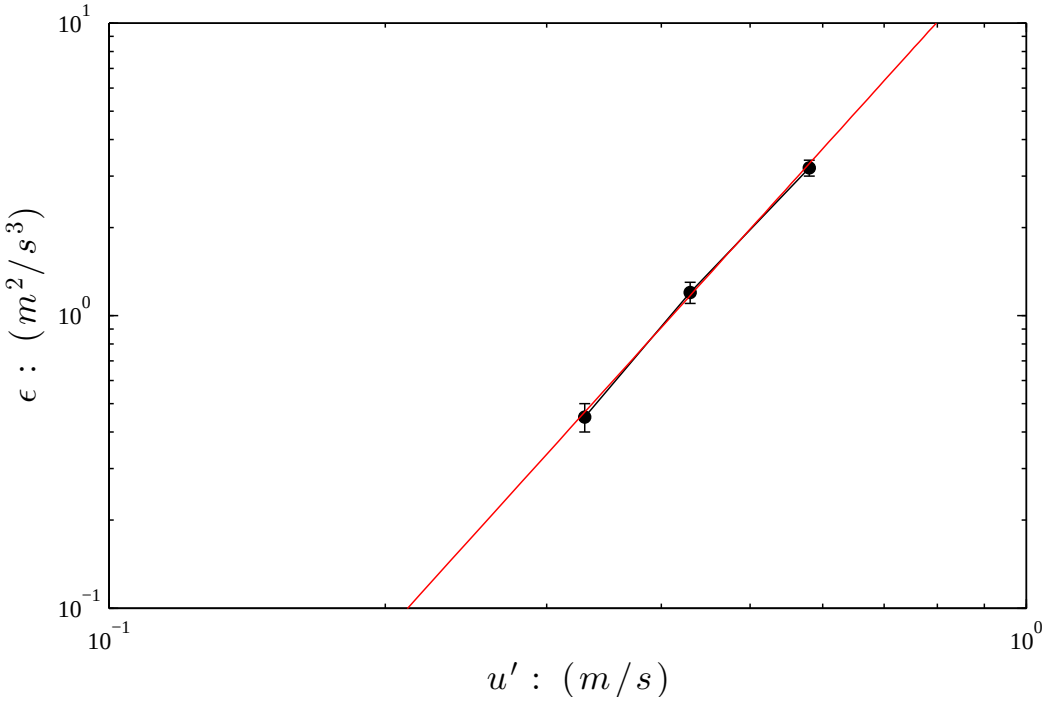

Figure A.2: Turbulence dissipation rate, ϵ, as a function of the driven u' in the Chapter 4, soccer ball apparatus. The black dots are 3D particle tracking measurements from Bewley et al. (2013). The red line is a power-law fit with equation $\epsilon = 21.9u'^{3.47}$.

data of Bewley et al. (2013), which clearly showed $\epsilon \propto u'^{3.5}$ (see figure A.2), indicating that ℓ grows like nearly $u'^{-0.5}$ in the apparatus. The reason for this is unclear. The transverse size of the jet should depend on the fixed cone size, while the longitudinal length scale could also depend upon the mean jet speed and correlation time of the signal sent to it. In any case, the Bewley et al. (2013) measurements show a strong fit, and so ϵ could be reliably interpolated from the dissipation measurements at the u' values given from the 2D particle tracking measurements in the settling study. R_λ and ℓ were then calculated from u' and ϵ.

A.2.4 Confidence intervals

As discussed in Chapter 4, there has been some disagreement between the various studies of particle settling, particularly amongst experiments. For this reason, particular care was taken regarding the uncertainty analysis in the new study, and both horizontal and vertical confidence intervals were given. The uncertainty analysis makes it undesirable, for example, to plot settling enhancement as a ratio of turbulent to still-fluid settling speeds, as this ratio can be off by orders of magnitude for small droplets, whose settling speeds are often less than the uncertainty in the mean flow speeds.

As the particles were polydispersed, binned data (in log space) were presented. Depending which particle parameter was plotted, the mean droplet size (based on $\langle d^4 \rangle$ or $\langle d^6 \rangle$) was calculated for each bin, with the bootstrapping method again used with 5000 samples to compute the 95% confidence intervals for this measurement. An uncertainty in size of one pixel in diameter, being 3.2 microns, was also assumed. For the large droplets this uncertainty was negligible. For the small droplets (down to about 15 microns) it could be seen in figure 4.3f that the sizing error due to this was significant. Uncertainty in the values of the Kolmogorov scales and large eddy scales of the flows were also taken into account. The errors in these measurements were discussed in the previous section and are listed parenthetically in table 4.1. Their importance varied of course depending upon the particle parameter of choice. For example, the 10% uncertainty in ϵ was increasingly significant for $\mathring{S}t_\eta \propto \epsilon^{1/4}$, $St_\eta \propto \epsilon^{1/2}$ and $\mathring{F}r_\ell \propto \epsilon$, (given $\ell \propto \epsilon^{-1}$), in that order.

For the vertical error bars of the mean settling speeds and velocity r.m.s. components, the bootstrapping method was again used for to obtain 95% con-

fidence intervals from the data within each size bin. A position error of one pixel relative to the mean displacement (in pixels) between frames for particles in a given size bin was also considered for the uncertainty in the measured velocities. For the settling velocity difference calculations, the lower bound of the plotted confidence intervals in figure 4.3f were based on subtraction of the still-fluid fall speed of a particle of the size at the upper bound of the bin's particle size 95% confidence interval, and vice versa. Finally, the uncertainty in determining u' was factored into the total confidence intervals presented in the Chapter 4 figures.

APPENDIX B

CHAPTER 3 APPENDICES[1]

B.1 The TNI droplet mixing layer model

Here, we describe the simple advection-diffusion model used for the TNI droplet mixing layer, where the droplet mean number density is treated like a diffusive species and hot-wire data has been used to inform a domain with an inhomogeneous turbulent diffusivity. We begin with the downstream evolution of the u_{rms} profiles for the TNI case in figure B.1. These are approximately error functions, so we first model the u_{rms} evolution as a diffusive process as well. The form of the error functions plotted in figure B.1 is determined from the analytical solution to the 1D advection-diffusion equation of a concentration species with step initial condition in a domain with homogeneous diffusivity, D. In a high-Péclet-number regime in two dimensions, where an advective scale (U) dominates the diffusive scale, the Taylor approximation $t = x/U$ may be used. The profiles were fit with the adapted form

$$u_{rms}(x,y) = u'_{min} + \left(\frac{u'_{max} - u'_{min}}{2}\right)\left[1 + erf\left(\frac{y - y_o}{\sqrt{4D_u(x/U)}}\right)\right], \tag{B.1}$$

where u'_{min}, u'_{max}, y_o and D_u are fitting parameters, the former two being the asymptotic u_{rms} values for a given error function fit. The three u_{rms} profiles are reasonably well-approximated using a constant diffusivity, D_u, of the turbulence r.m.s. Since $u'_{max} \propto (x_g)^{-m/2}$, where x_g is the distance from the active grid and with m the turbulence decay constant (e.g., Comte-Bellot and Corrsin, 1971), and since the other parameters did not vary significantly between fits

[1]by G. H. Good, S. Gerashchenko and Z. Warhaft; *J. Fluid Mech.*, Volume 694 (March 2012), pp. 371-198. Copyright © 2012 Cambridge University Press. Reprinted with permission.

at different downstream locations, the mixing layer u_{rms} may be approximated by a single equation in two dimensions. (We note that while the TTI droplet number density error function fits mentioned in the text indicate that the turbulence decay is not of primary importance, since they indicate a homogeneous diffusivity, we have chosen here to model the TNI flow profiles with the decay, as they were measured). The figure B.1 fits are calculated based on this single equation, and it is apparent that the TNI u_{rms} evolution may be modelled in this manner. Given $D_n \propto u_{rms}\ell$ (where D_n is the diffusivity of the droplet number density), $\ell \propto (x_g)^{1-m/2}$ (disregarding its transverse variation), and the previous result for $u_{rms}(x, y)$, $D_n(x, y)$ may be modelled to within a constant of proportionality. Using this, a simple, steady-state advection-diffusion finite-element model was created with a two-dimensional spatial domain, where a concentration species representing n advects/diffuses from a stepped boundary condition. (The mean streamwise velocity is input into the model).

The resulting model fits were thus determined for figure 3.8b. We note that the model constants produced diffusivities (D_n) in agreement with those of the TTI figure 3.8a error function fits (of the form of eq. B.1), but that these were nearly an order of magnitude smaller than predicted by the $u_{rms}\ell$ scaling, and this may be indicative of stirring/entrainment at the subintegral scales.

B.2 The role of initial conditions

As mentioned in the text, there is some shifting of the mean droplet number density profiles due to experimental initial conditions. This is known in particular from the $g0$ cases, where for the TTI the inflection point of the mean droplet

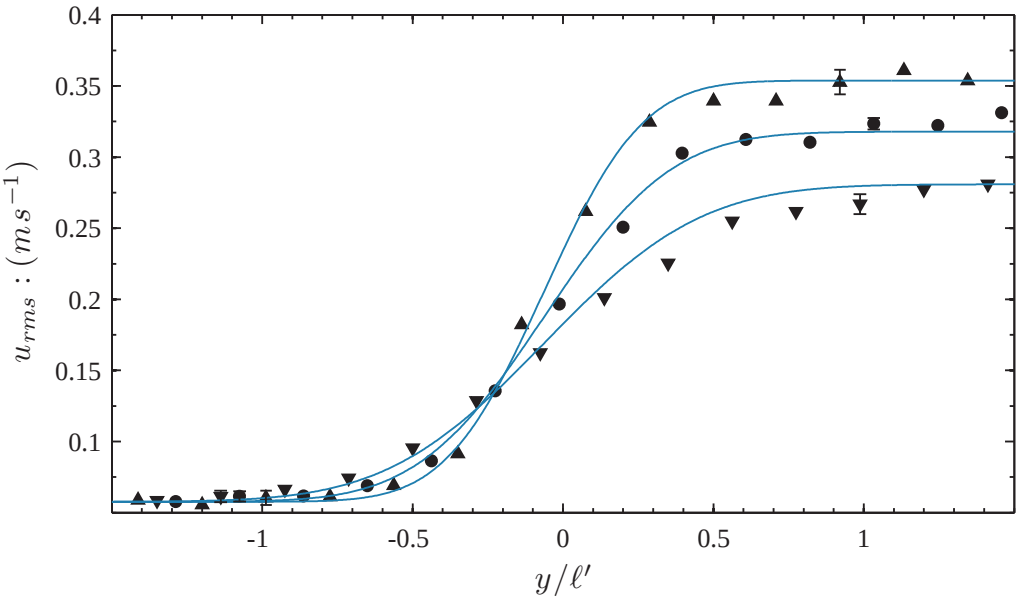

Figure B.1: TNI profiles of u_{rms} upstream ($t/\tau_{\ell'} \approx 0.4$, $x = 0.7m$), downstream ($t/\tau_{\ell'} \approx 1.1$, $x = 1.8m$) and at the test section ($t/\tau_{\ell'} \approx 0.7$, $x = 1.20m$), denoted by upward- and downward-pointing triangles and circles, respectively. The form of the error functions plotted at each x location is discussed in Appendix A.

number density profile (an error function) is displaced from $y = 0$, and for the TNI, where the profile is found to be yet further displaced when compared with matching profiles from both our model (appendix B.1) and the DNS results of an analogous mixing layer by Ireland and Collins (2012). The causes of these shifts may be (1) a deficit in the mean droplet number density near the splitter plate at the initial condition for both the TTI and TNI (due to the reduced particle flux in the spitter plate boundary layer), and (2) the flow asymmetry for the TNI. Figure B.2a shows the droplet number density initial condition, which is not perfectly (uniformly) mixed before the end of the splitter plate by the grid turbulence. A TTI diffusion model, a simplified version of that described for the TNI in appendix B.1, was used to show anticipated number density profiles resulting from both a uniform initial condition and one with a linear deficit. The

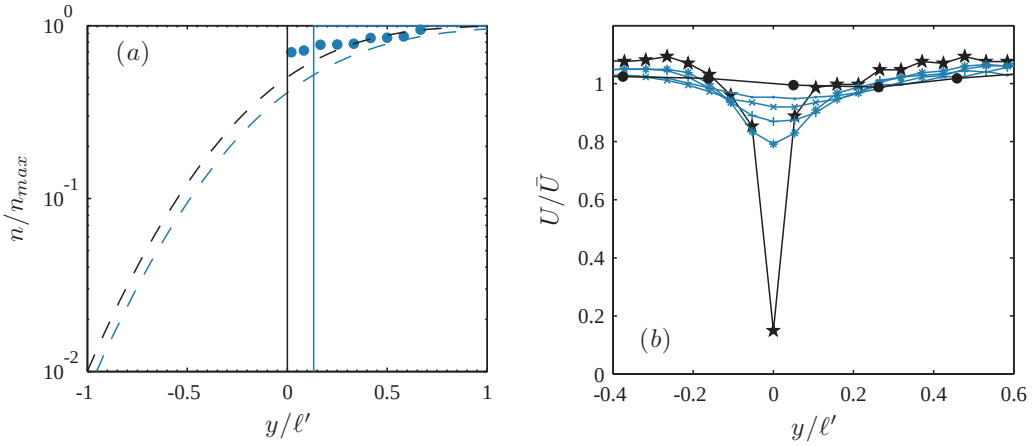

Figure B.2: Mixing layer displacements due to the droplet mean number density initial condition (at $x \equiv 0$) (*a*) and the diffusion of the splitter plate momentum deficit (*b*). In (*a*), the circles are the measured initial condition; the vertical line ($y/\ell' \approx 0.13$) denotes the *displacement thickness* of the number density profile. The dashed lines are FEM solutions (see Appendix B.1) for the test section based on a uniform profile and one with a linear deficit matched to the measured profile. In (*b*), hot-wire mean velocity profiles (normalized by the average velocity at their respective downstream location) are shown between the splitter plate trailing edge and the test section. Measurement stations are at $t/\tau_{\ell'} \approx 0.003, 0.064, 0.186, 0.427, 0.611,$ and 0.7, where $t = x/U$, denoted by stars, asterisks, pluses, multiplication signs, dots and circles, respectively.

resultant profile is the same in shape, but there is a shift of abscissa on the order of the number density displacement thickness of the deficit, and this result has been confirmed with the help of DNS (Peter Ireland, private communication). We find the TTI and TNI $g0$ cases to be shifted by $\sim 5cm$ and $\sim 8cm$ into the turbulent, seeded region, respectively. The additional displacement in the TNI case could be explained by more efficient mixing of the momentum deficit from the splitter plate boundary layers into the high-turbulence side, as shown in the hot-wire wake profiles of figure B.2b.

REFERENCES

S. Alberghi, A. Maurizi, and F. Tampieri. Relationship between the vertical velocity skewness and kurtosis observed during sea-breeze convection. *J. Appl. Meteorology*, 41:885–889, 2002.

A. Aliseda, A. Cartellier, F. Hainaux, and J. C. Lasheras. Effect of preferential concentration on the settling velocity of heavy particles in homogeneous isotropic turbulence. *J. Fluid Mech.*, 468:77–105, 2002.

M. Andrejczuk, W. W. Grabowski, S. P. Malinowski, and P. K. Smolarkiewicz. Numerical simulation of cloud clear air interfacial mixing. *Atmos. Sci.*, 61: 17261739, 2004.

D. Anfossi, E. Ferrero, D. Sacchetti, and S. T. Castelli. Comparison among empirical probability density functions of the vertical velocity in the surface layer based on higher order correlations. *Boundary-Layer Meteorology*, 82:193–218, 1996.

S. Ayyalasomayajula, A. Gylfason, L. Collins, E. Bodenschatz, and Z. Warhaft. Lagrangian measurements of inertial particle accelerations in grid generated wind tunnel turbulence. *PRL*, 97:144507, 2006a.

S. Ayyalasomayajula, A. Gylfason, L. R. Collins, E. Bodenschatz, and Z. Warhaft. Lagrangian measurements of inertial particle accelerations in grid generated wind tunnel turbulence. *Phys. Rev. Lett.*, 97:144507, 2006b.

J. Bec, L. Biferale, M. Cencini, A. Lanotte, S. Musacchi, and F. Toschi. Heavy particle concentration in turbulence at dissipative and inertial scales. *PRL*, 98: 084502, 2007.

G. P. Bewley, K. Chang, and E. Bodenschatz. On integral length scales in anisotropic turbulence. *Phys. Fluids*, 24:061702, 2012.

G. P. Bewley, E. W. Saw, and E. Bodenschatz. Observation of the sling effect. Under Review, 2013.

F. Boettcher, C. H. Renner, H. P. Waldl, and J. Peinke. On the statistics of wind gusts. *Boundary-Layer Meteorology*, 108:163–173, 2003.

T. Bosse and L. Kleiser. Small particles in homogeneous turbulence: Settling velocity enhancement by two-way coupling. *Phys. Fluids*, 18:027102, 2006.

A. Bracco, J. LaCasce, C. Pasquero, and A. Provenzale. The velocity distribution of barotropic turbulence. *Phys. Fluids*, 2000a.

A. Bracco, J. H. LaCasce, and A. Provenzale. Velocity probability density functions for oceanic floats. *J. Physical Oceanography*, 2000b.

J. E. Broadwell and R. E. Breidenthal. A simple model of mixing and chemical reaction in a turbulent shear layer. *J. Fluid Mech.*, 125:397–410, 1982.

L. W. B. Browne, R. A. Antonia, and L. P. Chua. Calibration of x-probes for turbulent flow measurements. *Exp. Fluids*, 7:201–208, 1989.

S. J. Caughey. Observed characteristics of the atmospheric boundary layer. In F. T. M. Nieuwstadt, H. van Dop, and D. Reidel, editors, *Atmospheric Turublence and Air Pollution Modelling*, pages 107–158. Reidel, Dordrecht, Holland, 1982.

T. Cebeci and P. Bradshaw. *Momentum Transfer in Boundary Layers*. McGraw-Hill Book Co., New York, 1977.

K. Chang, G. P. Bewley, and E. Bodenschatz. Experimental study of the influence of anisotropy on the inertial scales of turbulence. *J. Fluid Mech.*, 692:464–481, 2012.

R. Clift, J. R. Grace, and M. E. Weber. *Bubbles, Drops, and Particles*. Academic Press, 1978.

G. Comte-Bellot and S. Corrsin. Simple eulerian time correlation of full and narrow-band velocity signals in grid-generated 'isotropic' turbulence. *J. Fluid Mech.*, 48:273–337, 1971.

J. Dávila and J. C. R. Hunt. Settling of small particles near vortices and in turbulence. *J. Fluid Mech.*, 440:117–145, 2001.

J. W. Deardorff. Three-dimensional numerical study of turbulence in an entraining mixed layer. *B.L. Meteorology*, 7(2):199–226, 1974.

B. Efron. Bootstrap methods: Another look at the jackknife. *Ann. Statist.*, 7(1): 1–26, 1979.

S. Elghobashi and G. C. Truesdell. On the two-way interaction between homogeneous turbulence and dispersed solid particles. i: Turbulence modification. *Phys. Fluids A*, 5:7, 1993.

H. Fellouah, C. G. Ball, and A. Pollard. Reynolds number effects within the development region of a turbulent round free jet. *Intl. J. Heat and Mass Transfer*, 52(17–18):3943–3954, 2009.

R. F. Fox, I. R. Gatland, R. Roy, and G. Vernuri. Fast, accurate algorithm for numerical simulation of exponentially correlated coloured noise. *Physical Review*, 38(11):5938–5940, 1988.

P. D. Friedman and J. Katz. Mean rise rate of droplets in isotropic turbulence. *Phys. Fluids.*, 14:3059–3073, 2002.

S. Gerashchenko, N. S. Sharp, S. Neuscamman, and Z. Warhaft. Lagrangian measurements of inertial particle accelerations in a turbulent boundary layer. *J. Fluid Mech.*, 617:255–281, 2008.

S. Gerashchenko, G. Good, and Z. Warhaft. Entrainment and mixing of water droplets across a shearless turbulent interface with and without gravitational effects. *J. Fluid Mech.*, 668:293–303, 2011.

S. Ghosh, J. Dávila, J. C. R. Hunt, A. Srdic, H. H. S. Fernando, and P. R. Jonas. How turbulence enhances coalescence of settling particles with applications to rain in clouds. *Proc. R. Soc. A*, 461:3059–3088, 2005.

J. P. Gollub, J. Clarke, M. Gharib, B. lane, and O. N. Mequita. Fluctuations and transport in a stirred fluid and a mean gradient. *Phys. Rev. Lett.*, 67:3507, 1991.

G. H. Good and Z. Warhaft. On the probability distribution function of the velocity field and its derivative in multi-scale turbulence. *Phys. Fluids*, 23: 95–106, 2011.

G. H. Good, S. Gerashchenko, and Z. Warhaft. Intermittency and inertial particle entrainment at a turbulent interface: the effect of the large-scale eddies. *J. Fluid Mech.*, 694:371–398, 2012.

A. Gylfason, S. Ayyalasomayajula, and Z. Warhaft. Intermittency, pressure and acceleration statistics from hot-wire measurements in wind-tunnel turbulence. *J. Fluid. Mech.*, 501(1):213–229, 2004.

P. E. Hancock and P. Bradshaw. Turbulence structure of a boundary layer beneath a turbulent free-stream. *J. Fluid Mech.*, 205:45–76, 1989.

R. J. Hill. Geometric collision rates and trajectories of cloud droplets falling into a burgers vortex. *Physics of Fluids*, 17:037103, 2005.

G. L. Holtzer and L. R. Collins. Relationship between the intrinsic radial distribution function for an isotropic field of particles and lower-dimensional measurements. *J. Fluid Mech.*, 459:93–102, 2002.

J. C. R. Hunt. Turbulent diffusion from sources in complex flows. *Ann. Rev. Fluid. Mech.*, 17:447–485, 1985.

J. C. R. Hunt and J. M. R. Graham. Free stream turbulence near plane boundaries. *J. Fluid Mech.*, 84:209–235, 1978.

H. J. Hussein, S. Capp, and W. K. George. Velocity measurements in a high-reynolds-number, momentum-conserving, axisymmetric, turbulent jet. *J. Fluid Mech.*, 258:31–75, 1994.

P. J. Ireland and L. R. Collins. Direct numerical simulation of inertial particle entrainment in a shearless mixing layer. *J. Fluid Mech.*, 704:301–332, 2012.

P. J. Ireland, T. Vaithianathan, P. S. Sukheswalla, B. Ray, and L. R. Collins. Highly parallel particle-laden flow solver for turbulence research. *Comp. and Fluids*, 76:170–177, 2013.

Jayesh and Z. Warhaft. Probability distribution, conditional dissipation, and transport of passive temperature fluctuations in grid-generated turbulence. *Phys. Fluids A*, 1991.

Jayesh and Z. Warhaft. Turbulent penetration of a thermally stratified interfacial layer in a wind tunnel. *J. Fluid Mech.*, 1994.

J. Jimenez. Algebraic probability density tails in decaying isotropic two-dimensional turbulence. *J. Fluid Mech.*, 313:223–240, 1996.

H. S. Kang and C. Meneveau. Experimental study of an active grid-generated shearless mixing layer and comparisions with large-eddy simulation. *J. Fluid Mech.*, 20:125102, 2008.

L. H. Kantha, O. M. Phillips, and R. Azad. On turbulent entrainment at a stable density interface. *J. Fluid Mech*, 79:753–768, 1977.

K. Kawanisi and R. Shiozaki. Turbulent effects on the settling velocity of suspended sediment. *J. Hydraul. Eng.*, 134(2):261–266, 2008.

D. H. Kelley and N. T. Ouellette. Using particle tracking to measure flow instabilities in an undergraduate laboratory experiment. *Am. J. Phys.*, 79:267–273, 2011.

A. R. Kerstein. Linear-eddy modelling of turbulent transport, part 6, microstructure of diffusive scalar mixing fields. *J. Fluid Mech.*, 231:361, 1991.

P. Knebel, A. Kittel, and J. Peinke. Atmospheric wind field conditions generated by active grids. *Experiments in Fluids*, In Press, 2011.

P. A. Krogstad and P. A. Davidson. Freely decaying, homogeneous turbulence generated by multi-scale grids. *J. Fluid Mech.*, 680:417–434, 2011.

B. J. Lázaro and J. C. Lasheras. Particle dispersion in a turbulent, plane, free shear layer. *Physics of Fluids*, 1:1035–1044, 1989.

D. H. Lenchow, J. Mann, and L. Kristensen. How long is long enough when measuring fluxes and other turbulence statistics? *J. Atmos. Oceanic Tech.*, 11: 661–673, 1994.

E. K. Longmire and J. K. Eaton. Structure of a particle-laden round jet. *J. Fluid Mech.*, 236:217–257, 1992.

M. J. Manton. On the motion of a small particle in the atmosphere. *B.L. Meteorol.*, 6:487–504, 1974.

I. Marusic, R. Mathis, and N. Hutchins. Predictive model for wall-bounded turbulent flow. *Science*, 329:193–196, 2010.

N. Mazellier and J. C. Vassilicos. Turbulence without Richardson-Kolmogorov cascade. *Phys. Fluids*, 2010.

D. A. McQuarrie. *Statistical Mechanics*. Harper Row, New York, 1976.

R. Mei. Effect of turbulence on the particle settling velocity in the nonlinear drag range. *Int. J. Multiphase Flow*, 20:273–284, 1994.

N. Mordant, A. Crawford, and E. Bodenschatz. Experimental lagrangian acceleraition probability density function measurements. *Physica D*, 193:245–251, 2004.

H. Mouri, M. Takaoka, A. Hori, and Y. Kawashima. Probability density function of turbulent velocity fluctuations. *Phys. Rev. E*, 2002.

S. P. Murray. Settling velocities and vertical diffusion of particles in turbulent water. *J. Geophys. Res.*, 75:1647–1654, 1970.

L. Mydlarski and Z. Warhaft. On the onset of high-reynolds-number grid-generated wind tunnel turbulence. *J. Fluid Mech.*, 320:331–368, 1996.

L. Mydlarski and Z. Warhaft. Passive scalar statistics in high-péclef-number grid turbulence. *J. Fluid Mech.*, 358:135–175, 1998.

A. Naert, B. Castaing, B. Chabaud, B. Hebral, and J. Peinke. Conditional statistics of velocity fluctuations in turbulence. *Physica D*, 113:73, 1998.

P. Nielsen. Turbulence effects on the settling of suspended particles. *J. Sediment. Petrol.*, 63(5):835–838, 1993.

N. T. Ouellette, H. Xu, M. Bourgoin, and E. Bodenschatz. A quantitative study of three-dimensional lagrangian particle tracking algorithms. *Exp's in Fluids*, 40:301–313, 2006.

A. Pumir, B. Shraiman, and E. D. Siggia. Exponential tails and random advection. *PRL*, 1991.

J. P. L. C. Salazar, J. de Jong, L. Cao, S. H. Woodward, H. Meng, and L. R. Collins. Experimental and numerical investigations of inertial particle clustering in isotropic turbulence. *J. Fluid Mech.*, 600:245–256, 2008.

E. W. Saw, R. A. Shaw, S. Ayyalasomayayajula, P. Y. Chuang, and Á. Gylfason. Inertial clustering of particles in high-reynolds-number turbulence. *PRL*, 100: 214501, 2006.

B. L. Sawford, P. K. Yeung, M. S. Borgas, P. Vedula, A. La Porta, A. M. Crawford, and E. Bodenschatz. Conditional and unconditional acceleration statistics in turbulence. *Phys. Fluids*, 15(11), 2003.

N. S. Sharp, S. Neuscamman, and Z. Warhaft. Effects of large-scale free stream turbulence on a turbulent boundary layer. *Physics of Fluids*, 21:095105, 2009.

R. A. Shaw. Particle-turbulence interactions in atmospheric clouds. *Annu. Rev. Fluid Mech.*, 35:183–227, 2003.

R. A. Shaw, W. C. Reade, L. R. Collins, and J. Verlinde. Preferential concentration of cloud droplets by turbulence: Effects on the early evolution of cumulus cloud droplet spectra. *J. Atmo. Sci.*, 55:1965–1976, 1998.

R. A. Shaw, A. B. Kostinski, and M. L. Larsen. Towards quantifying droplet clustering in clouds. *Quart. J. Roy. Meteor. Soc.*, 128(582):1043–1057, 2002.

X. Shen and Z. Warhaft. The anisotropy of the small scale structure in high reynolds number ($R_\lambda \sim 1000$) turbulent shear flow. *Phys. Fluids*, 12:2976, 2000.

H. Siebert, S. Gerashchenko, A. Gylfason, K. Lehmann, L.R. Collins, R. A. Shaw, and Z. Warhaft. Towards understanding the role of turbulence on droplets in clouds: In situ and laboratory measurements. *Atmospheric Research*, 97:426–437, 2010.

K. D. Squires and J. K. Eaton. Preferential concentration of particles by turbulence. *Phys. Fluids A*, 3:1169–1178, 1991.

S. Sundaram and L. R. Collins. Collision statistics in an isotropic particle-laden turbulent suspension. part 1. direct numerical simulations. *J. Fluid Mech.*, 335: 75–109, 1997.

S. Sundaram and L. R. Collins. A numerical study of the modulation of isotropic turbulence by suspended particles. *J. Fluid Mech.*, 379:105–143, 1999.

S. Tavoularis and S. Corrsin. Experiments in nearly homogeneous turbulent shear flow with a uniform mean temperature gradient. *J. Fluid Mech.*, 104: 311–347, 1981.

P. F. Tooby, L. W. Gerald, and D. I. John. The motion of a small sphere in a

rotating velocity field: A possible mechanism for suspending particles in turbulence. *J. Geophys. Res.*, 82(15):2096–2100, 1977.

A. A. Townsend. *The Structure of Turbulent Shear Flow*. Cambridge University Press, Cambridge, 1976.

J. S. Turner. Turbulent entrainment: the development of the entrainment assumption, and its applications to geophysical flows. *J. Fluid Mech.*, 173:431–471, 1986.

S. Veeravalli and Z. Warhaft. The shearless turbulence mixing layer. *J. Fluid Mech.*, 207:194–229, 1989.

G. A. Voth, A. La Porta, A. M. Crawford, J. Alexander, and E. Bodenschatz. Measurement of particle accelerations in fully developed turbulence. *J. Fluid Mech*, 469:121–160, 2002.

L. P. Wang and M. R. Maxey. Settling velocity and concentration distribution of heavy particles in homogeneous isotropic turbulence. *J. Fluid Mech.*, 256: 26–68, 1993.

Windpower Monthly. Facing up to the gearbox challenge: A survey of gearbox failure and collected industry knowledge. *Windpower Monthly*, 21, #11, November 2005.

A. Witkowska, J. G. Brasseur, and D. Juvé. Numerical study of noise from isotropic turbulence. *J. Comput. Acoust.*, 5:317–336, 1997.

E. J. P. Woittiez, H. J. J. Jonker, and L. M. Portela. On the combined effects of turbulence and gravity on droplet collisions in clouds: a numerical study. *J. Atmos. Sci.*, 66:1926–1943, 2009.

A. M. Wood, W. Hwang, and J. K. Eaton. Preferential concentration of particles in homogeneous and isotropic turbulence. *Intl. J. Multiphase Flow*, 31:1220–1230, 2005.

C. Y. Yang and U. Lei. The role of turbulent scales in the settling velocity of heavy particles in homogeneous isotropic turbulence. *J. Fluid Mech.*, 371: 179–205, 1998.

T. S. Yang and S. S. Shy. The settling velocity of heavy particles in an aqueous near-isotropic turbulence. *Phys. Fluids*, 15:868–880, 2003.

T. S. Yang and S. S. Shy. Two-way interaction between solid particles and homogeneous air turbulence: particle settling rate and turbulence modification measurements. *J. Fluid Mech.*, 526:171–216, 2005.

K. Yoon and Z. Warhaft. The evolution of grid-generated turbulence under conditions of stable thermal stratification. *J. Fluid Mech.*, 215:601–638, 1990.